CHAPTER 1

INTRODUCTION

1.1 Motivation

Due to recent significant improvement in the standard of living, refrigerated display cases are extensively used in today's supermarkets and grocery stores. For the purpose of saving precious floor-space and providing a large selling surface, vertical display cabinets are the better choice than the horizontal ones [1]. In order to attract consumers and hence increase sales, manufacturers developed open display cases with no obstacle between the products and customers [1-4]. A cold air curtain is often used to produce a factitious barrier between the inside cold air in the cabinets and the outside warm air in the ambient. The air curtain is essentially a two-dimensional cool air jet. Usually, the air curtain is provided from the upper wall of a display case through a discharge honeycomb, then flows over the open surface of the cabinet, and finally reaches a return air grille at the case bottom. In real situation, an open display case is operated in a store environment and it exchanges heat and moisture with the surrounding air in the store. Besides, the outside warm and moist air can be entrained into the display case by the air curtain, which in turn can substantially lower the performance of the case and hence the energy efficiency. The warm and moist air entrained into the cabinet becomes sensible and latent energy loads to the cabinet since the air needs to be cooled and the moisture in it should be removed. The performance of refrigerated display cabinets is affected by many factors, including the velocity and temperature of the jets and the temperature, humidity and air flow velocity in the ambient environment. Therefore a detailed understanding of the heat and mass transfer processes in open refrigerated display cases is needed to improve the performance of the systems. Especially, how the momentum, energy and moisture transports in the cabinets are affected by the moist air entrained into the flow and the interactions between the buoyancy forces and momentum forces in the flow in the cabinets and ambient require an in-depth investigation. To facilitate the exploration of the complicate transport processes in the display cabinets, we focus on a cabinet with a laminar air curtain flowing over its open surface.

1.2 Literature Review

The literature relevant to the present study is reviewed in the following.

1.2.1 Cooling loads and thermal entrainment factor

The total cooling loads of a refrigerated display cabinet consists of sensible and latent components. The sensible portion includes heat conduction through physical envelopes of the cabinet, thermal radiation from the ambient to the cabinet, sensible infiltration, and heat gains from fan motors, anti-sweat heater and defrost. The latent portion refers to the entrainment of the moisture in the ambient into the cabinet through the air curtains. The efficiency of an air curtain ε was defined by Cortella et al. [1, 5] as $\varepsilon = \frac{heat\ \ flow\ rate\ \ from\ the\ load}{total\ refrigerating\ capacity}$ according to the results from a numerical simulation by using a LES (Large Eddy Simulation) turbulence model. It was pointed out by Faramarzi [6, 7] that the infiltration of the moist air from the ambient into the cabinet was the largest constituent of the case cooling load. And the infiltration load can be further divided into the sensible and latent parts. The sensible and latent portions respectively result from the temperature and water vapor concentration differences between the air in the ambient and in the cabinet. Hence determining the infiltration load is considered as the most challenging aspect of the display case cooling load analysis. On the other hand, Ge and Tassou [8] used an implicit numerical method to simulate flow and heat transfer in a vertical display case and developed a correlation for the total heat transfer across an air curtain in terms of the ambient air enthalpy, initial dry-bulb temperature of air jet, temperature difference between the air inside the cabinet and injected air, and some air curtain properties such as the jet initial velocity, jet mass flow rate and jet length. Jet thickness is not directly included, but has some relationship with the jet velocity and mass flow rate. They also proposed a correlation for the return air temperature based on the air temperature at the injection grille and ambient and on the air curtain length. In addition, Faramarzi [7, 9] observed that the temperature of the products and the air temperature near the return grille were increased by the entrainment of the ambient warm air into a display cabinet. Recently Chen & Yuan [4, 10] and Bhattacharjee & Loth [11] defined a thermal entrainment factor as $\alpha = \frac{i_r - i_s}{i_{amb} - i_s}$ = (enthalpy difference between the return and supply air) / (enthalpy difference between the ambient and supply air). If the air curtain does not cause any air entrainment, α will be equal to zero. On the contrary, the enthalpy of return air and thermal entrainment factor α increase if the moist air entrainment increases. In practical situation α would be between zero and unity. The amount of warm air that moves into the display case through the air curtain is called the infiltration. Similarly, Navaz et al. [3] introduced a parameter to characterize the portion of air mass spillage to the inside and infiltration into the case. However, Navaz et al. [2 3] and Bhattacharjee and Loth [11] also estimated the volumetric infiltration rate by integrating the negative horizontal velocity component from the bottom edge of the opening at the air return grille to a location where U= 0. Besides, they also noted that the infiltration rate was mostly momentum driven and was a very week function of the discharge air temperature. On the other hand, Chen & Yuan [4, 10] investigated how the thermal entrainment factor was affected by the jet Reynolds number (based on the jet length H) and Richardson number (based on the jet length H and temperature difference between the ambient and injection air, $Ri_t = Gr_t / Re_H^2$). They found that when the Richardson number decreased to 0.14, the infiltration rate arrived at a minimum. For a further reduction in Ri_t the infiltration rate would increase slightly due to the excessive mixing. They suggested that there existed a critical Richardson number to ensure the insulation of the air curtain at a given Grashof number. For increases in Re_H and Ri_t the thermal entrainment factor increases slightly, signifying that the momentum force would promote the thermal entrainment but the buoyant force would suppress it. Chen & Yuan [4.10] observed that cold air curtains in refrigerated display cabinets were negatively buoyant jets which were dominated by momentum and gravitational forces and the combined effects of forced and natural convection due to density difference. Then they pointed out that perfect insulation of cold air curtains depended on the combined effects of initial momentum, gravitational forces and the pressure difference across the air curtain. If the initial momentum is insufficient to sustain the pressure difference, the cold air curtain will deflect inwards after exiting from the supply grille, and perfect insulation is not assured.

1.2.2 Importance of ambient temperature and relative humidity

In a combined CFD & experimental DPIV study, Navaz et al. [2] found that the discharge average temperature exhibited a relatively slight effect on the flowfield structure in the cabinet. Then in a numerical prediction Cortella [5] showed that the indoor environment in which display cases operated significantly affected the performance of air curtain. Faramarzi and Kemp [12] experimentally tested several refrigerated display cabinets subject to different relative humidities and noted that the higher indoor temperature and relative humidity yielded an increase in the case cooling loads for the display cases. Combined experimental measurement and numerical prediction carried out by Howell et al. [13] showed that the sensible heat transfer was directly proportional to the temperature difference across the air curtain. Recently, Chen & Yuan [4] experimentally demonstrated that the air temperature rise between the discharge and return grilles was slightly affected by the change in the relative humidity of the ambient air. As the ambient temperature increased at a constant relative humidity, the air humidity ratio also increased and hence the latent heat transfer across the air curtain increased with the infiltration. In addition, Howell [14] developed a numerical procedure to evaluate the effects of relative humidity on the energy performance of refrigerated display cabinets and showed that a decrease in the store relative humidity from 55% to 35% would reduce the open display case energy consumption by 29%.

1.2.3 Effects of discharge air velocity

The total heat transfer through an air curtain was found to be directly proportional to the initial jet velocity [11, 15]. By comparing the CFD and experimental results, Navaz et al. [2] noted that a small air discharge velocity still could entrain the ambient air and a less stable air curtain would break up before reaching the bottom section of the cabinet and suggested that the infiltration rate was a function of the discharge air velocity. Cortella et al. [1] used a LES turbulence model to predict a two-curtain display case. They found that the most stable flow configuration in the cabinet was obtained when the inner air curtain had a lower velocity. Cui & Wang [16] used a commercial software FLUENT to predict the transport processes in a cabinet and introduced a parameter, *UI*, to describe the uniformity of the air velocity distribution at the discharge grille. They suggested that a low inlet *UI* value was preferred in an energy-efficient design for a display case. Chen & Yuan [4] found that when Re_H was raised from 4,100 to 4,500, the temperature inside the cabinet decreased roughly 1-1.5 ℃, and the cabinet temperature was more uniform. Besides, the temperature difference between the discharge and return air is smaller. Axell and Fahlen [17] carried out experimental measurement and numerical simulation and argued that a relatively small discharge velocity should be recommended in designing an air curtain. However, a small discharge velocity would possess insufficient initial momentum to prevent the invading of the warm moist air from the outside.

1.2.4 Effects of air flow from the perforated back panels

It was suggested by Navaz et al. [3] and Chen and Yuan [4] that the air flow from the perforated back panels not only provided air curtain stability by reducing the entrained warm ambient air, but also helped the air temperature in the case to stabilize immediately after any intrusion. Navaz et al. [3] indicated that any intrusion could cause the warm air to penetrate into the lower shelves and became stagnant there. In an experimental investigation Chen & Yuan [4] tested different perforation densities and found that the heat load dropped slightly for an increase in the perforation density.

1.2.5 Effects of discharge width and length of air curtain

The ratio of the opening height H of a cabinet to the width b_j of the discharge jet was also noted to be an important factor in influencing the performance of air curtains. A larger jet width could improve the quality of the thermal insulation. At the same Richardson number the volumetric infiltration rate reduces greatly for a smaller ratio [10, 18, 19]. Chen & Yuan [4] and Besbes et al. [19] showed that as the H / b_j ratio was decreased, the higher energy efficiency was obtained and the critical Richardson number was higher. The flow pattern and heat transfer characteristics of the air curtain could be affected significantly by the value of the H / b_j ratio [4, 10, 21, 22]. Axell & Fahlen [17] manifested that the air flow in the air curtain could be divided into transition, fully developed and recovery regions. Besides, the flow rate was constant in the transition region. In the fully developed region, the air flow slows down. While in the recovery region, the air velocity profile and flow rate depend on the design of the return grille.

1.2.6 Laminar jet

Schlichting [23] defined a free plane jet as laminar for the Reynolds number $\leqq 30$. Besides, Gardon and Akfirat [24] regarded the two-dimensional jets with $Re > 2{,}000$ as turbulent. Additionally, McNaughton and Sinclair [25] proposed the characteristic flow regimes for circular free jets : dissipated-laminar jets for $Re < 300$, fully laminar jets for $300 < Re < 1{,}000$, semi-turbulent jets for $1{,}000 < Re < 3{,}000$, and fully turbulent jets for $Re > 3{,}000$.

1.2.7 Mixed convection over an open cavity

The transport processes in the flow associated with a vertical display case protected by an air curtain can be regarded as mixed convection over an open cavity, which has received some attention in the past. Khanafer et al. [26] numerically predicted the mixed convection in an open-ended two-dimensional enclosure for three basic configurations: horizontal flow, vertical flow, and inclined flow for $100 \leqq Re \leqq 10{,}000$ and $100 \leqq Gr_t \leqq 100{,}000$. They illustrated that a high horizontal flow speed could be used to insulate a horizontal cavity from the surrounding flow medium thus minimizing the heat exchange between the cavity and the surroundings. In a continuing study they experimentally investigated the effects of heated wall position on mixed convection in a horizontal plane channel with an open rectangular cavity [27]. Three heated modes were considered: assisting flow, opposing flow, and heating from below. Results for the Richardson number of 0.1 and 100, Re =100 and 1,000, and aspect ratio in the range of 0.1-1.5 were reported. It was shown that the maximum temperature was lower as the Reynolds and Richardson numbers increased. The effects of the ratio of the channel height to cavity height were found to play a significant role on streamline and isotherm patterns for different heating configurations. The investigation showed that the opposing forced flow configuration had the highest thermal performance, in terms of both maximum temperature and average Nusselt number. Later on, they experimentally investigate mixed convection in the horizontal plane channel with the open rectangular cavity studied previously for the assisting heating modes [28]. Their results indicate that at the lowest investigated Reynolds number (Re=100) the surface temperature of the heated plate was lower than the corresponding surface temperature for Re=1,000, at the same Richardson number. The flow visualization pointed out that for Re = 1,000 there were two nearly distinct fluid motions: a parallel forced flow in the channel and a recirculation flow inside the cavity. For Re =100 the stronger buoyancy induces a penetration of thermal plume from the heated plate wall into the upper channel. In a numerical simulation Leong et al. [29] examined mixed convection in a bottom heated open cavity in a horizontal channel. The results showed that the transition to the mixed convection regime depended on the relative magnitudes of the Grashof and Reynolds numbers and the cavity aspect ratio. For a high Grashof number ($Gr_t > 10^5$), the flow may become unstable. In the mixed convection regime, the heat transfer rate is reduced. Particularly for $Gr_t > 10^3$, there is a critical Reynolds number in the transitional regime which makes the heat transfer a minimum. For flows at $Gr_t > 10^3$ and a small Reynolds number, heat transfer on the other hand can be approximated by the natural convection limit. Slightly later, Brown and Lai [30] proposed empirical correlations for combined heat and mass transfer in mixed convection of air from the same cavity. The correlations have covered the entire convection regime, from natural, mixed, to forced convection, for mass-transfer driven flows $(|N| > 1)$.

On the other hand, Polat and Bilgen [34] numerically studied conjugated heat transfer between conduction in the cavity walls and laminar natural convection in inclined open swallow cavities. They found that the volume flow rate was an increasing function of the Rayleigh number and the aspect ratio of the cavity, heated wall thickness and the inclined angle of the cavity from the horizontal and a decreasing function of the thermal conductivity ratio of the wall to fluid. Heat transfer varies nonmonotonically with the Rayleigh number due to the complex recirculating flow induced in the cavity. Then, Hasnaoui et al. [32] conducted a two-dimensional numerical simulation to investigate the mixed convection heat transfer in ventilated cavities with opposing and assisting flows. The opposing flow configuration was found to be more useful to reduce the mean temperature inside the cavity for $Re \leq 1{,}000$. Also, the maximum competition between natural and forced convections could be characterized by the maximum values of the Nusselt number. However, the opposing flow configuration was unfavorable for the natural convection development at lower values of Reynolds number. In a continuity study [33] mixed convection in a vertical rectangular cavity containing adiabatic fins attached to the vertical heated surface was examined. They noted that heat transfer was significantly affected by the presence of the fins. Besides, the intensity of forced flow through the lower opening is an important factor in cooling the heated surface. However, a numerical investigation of laminar mixed-convective cooling of a horizontal rectangular cavity with differentially heated vertical walls had been conducted to identify the optimum placement of inlet and exit openings for best cooling effectiveness by Singh and Sharif [34]. Their study encompassed a range of the Reynolds number from 50 to 500 and a range of the Richardson number from 0 to 10, covering dominating forced convection through mixed convection to dominating natural convection. Results showed that injecting air through the cool wall was more effective in heat removal, due to the impinging effect of the cold air jet onto the opposite hot wall. Moreover, for the configuration with the inlet opening near the bottom and the exit opening near the top, the forced and natural convection assist each other in the heat removal from the hot wall. The configuration utilizing both of these favorable features can produce higher cooling efficiency, higher average Nusselt number and lower bulk average temperature. A similar study from Ramirez- Iraheta et al. [35] numerically investigated passive (natural- convection) and mixed-convection cooling of vertical stacks of heat-generating bodies inside a cavity with openings for inlet and outlet flow. They showed that the locations of the inlet and outlet ports relative to the stack position substantially influenced the cooling effectiveness. In some cases, the increase in the inlet flow rate of the coolant associated with mix-convection cooling did not improve the cooling through natural convection. It was also demonstrated that passive cooling could be more effective than mixed-convection cooling for certain conditions. Besides, a detailed experimental study of heat transfer in an open isothermal cubic cavity for mixed convection was carried out by Pavlovic and penot [36]. They quantitatively confirmed the important influence of the external flow on the heat transfer in the open isothermal cubic cavity. The influences of different types of front masks on the convective heat transfer were also examined.

1.3 Objective of Present Study

The above literature review clearly indicates that a better design of refrigerated display cabinets to improve their energy efficiencies is still an important goal to the refrigeration industry. Minimizing the infiltration of the warm and humid outside air into the cabinets through improving the performance of air curtains is therefore essential in this design. In the present study a two-dimensional numerical simulation will be conducted to explore the detailed momentum, heat and mass transfer processes in an open vertical refrigerated display case subject to a laminar air curtain. In order to get a more fundamental understanding of the thermal entrainment process, attention will be focused on how the parameters associated the laminar air curtain affect the transport processes in the display case and hence the performance of the cabinet.

CHAPTER 2

MATHMATICAL FORMULATION

The physical model adopted here and the governing equations used to numerically predict the transport processes in a vertical refrigerated display case are described in this chapter.

2.1 Physical Model

The simplifying physical model for investigating laminar momentum, heat and mass transfer in a vertical refrigerated display case adopted here is a two-dimensional vertical downward cold air jet flowing over the open surface of a vertical two-dimensional open cavity standing in a store environment, as schematically shown in Fig. 2.1. For the sake of avoiding the boundary conditions in the surrounding to affect our numerical results, the upper and right ambient surroundings are respectively placed at y = 0.6-m and x = 0.8-m, far from the open cavity. At the top and bottom of the open cavity there are discharge and return air flow zones adjacent to the ambient. Initially, the flows in the case and surrounding are assumed to be stationary, isothermal at the same temperature T_{amb}, and iso-solutal at the same water vapor concentration w_{1a}. Then at time $t \geq 0$ a cold plane air jet is introduced from the discharge grille of the cabinet and injects vertically downwards over the open cavity. At the air discharge grille the jet flow is assumed to be at a uniform speed V_j, at a lower uniform temperature T_j, and a uniform relative humidity ϕ_j. The width of the jet is b_j. Meanwhile, at time $t = 0$ we assume that the temperature of the inner vertical plate of the case is suddenly lowered to a uniform value T_c and maintained at this level thereafter. In the mean time, the upper plate and bottom plate of the cavity is kept adiabatic for $t \geq 0$, except at the discharge and return grilles of the cavity. In the present computation we assume $T_j = T_c$. The air flow at the steady state long after the jet discharged into the cavity is numerically predicted. In this study the size of the cavity is chosen to be small with 0.2-m in height and 0.1-m in depth. Note that in the present numerical simulation the computation domain surrounding the cavity is chosen to be large enough to reduce the effects of the store size on the flow in the cavity. The ambient is assumed at a uniform temperature T_{amb} and uniform relative humidity ϕ_{amb} for $t \geq 0$.

2.2 Assumptions and Governing Equations

To simplify the computation, the following assumptions are made:

1. Flow is laminar and incompressible.
2. Boussinesq approximation is valid and thermal radiation is neglected.
3. Heat conduction in the wall of the cavity and grilles are neglected in the computation. Besides, Heat capacity effects associated with the cavity wall and the grilles are negligible.
4. Neglect the viscous dissipation in the flow
5. $g_x = 0$, $g_y = -g$

With the Boussinesq approximation the pressure gradient and body force terms in the y- momentum equation are

$$-\partial p / \partial y - \rho g \ .$$

By using the equation of state for ideal gas mixture and assuming a low level of water vapor concentration in the flow, the density variation in the air flow can be approximated by

$$\rho = \rho_0\left[1-\beta_t(T-T_0)-\beta_m(w_1-w_{1_0})\right]. \tag{2.1}$$

Where ρ_0 is the mixture density evaluated at the referenced temperature T_0 and concentration w_{1_0}, and the referenced conditions are chosen to be that in the air surrounding. With the dynamic pressure in the y direction, p_m, defined as $p_m = p-\rho_o gy$

the term $-\partial p/\partial y-\rho g$ may be rewritten as $-\partial p_m/\partial y+\rho_0[1-\beta_t(T-T_0)-\beta_m(w_1-w_{1_0})]g$

$$=-\frac{\partial}{\partial y}(p-\rho_0 gy)+\rho_0 g\beta_t(T-T_0)+\rho_0 g\beta_m(w_1-w_{1_0}) \tag{2.2}$$

$$=-\frac{\partial p_m}{\partial y}+\rho_0 g\beta_t(T-T_0)+\rho_0 g\beta_m(w_1-w_{1_0})$$

Where β_t and β_m are respectively the volumetric coefficients of thermal and solutal expansion,

$$\beta_t \equiv -\frac{1}{\rho_0}\left(\frac{\partial\rho}{\partial T}\right)_{w_1,p}$$

$$\beta_m \equiv -\frac{1}{\rho_0}\left(\frac{\partial\rho}{\partial w_1}\right)_{T,p}$$

The concentration buoyancy force needs to be taken into account here due to the presence of the density variation with the non-uniform species concentration in the flow. Note that the buoyancy force resulting from the concentration difference may assist or oppose the thermal buoyancy force resulting from the temperature variation in the fluid, depending on whether the concentration expansion coefficient β_m is positive or negative. A combined Grashof number $\mathrm{Gr} = \mathrm{Gr}_t + (\mathrm{Pr}/\mathrm{Sc})^{1/2}\mathrm{Gr}_m$ was proposed to characterize the combined buoyancy effects [37].

Under these assumptions the basic equations describing the steady open cavity flow are

Continuity equation-

$$\frac{\partial(\rho u)}{\partial x}+\frac{\partial(\rho v)}{\partial y}=0 \tag{2.3}$$

x - momentum equation-

$$\rho\left[\frac{\partial u}{\partial t}+\left(u\frac{\partial u}{\partial x}+v\frac{\partial u}{\partial y}\right)\right]=-\frac{\partial p_m}{\partial x}+\left[\frac{\partial}{\partial x}\left(\mu\frac{\partial u}{\partial x}\right)+\frac{\partial}{\partial y}\left(\mu\frac{\partial u}{\partial y}\right)\right] \tag{2.4}$$

y- momentum equation-

$$\begin{aligned}&\rho\left[\frac{\partial v}{\partial t}+\left(u\frac{\partial v}{\partial x}+v\frac{\partial v}{\partial y}\right)\right]\\&=-\frac{\partial p_m}{\partial y}+\left[\frac{\partial}{\partial x}\left(\mu\frac{\partial v}{\partial x}\right)+\frac{\partial}{\partial y}\left(\mu\frac{\partial v}{\partial y}\right)\right]+\rho_0 g\beta_t(T-T_0)+\rho_0 g\beta_m(w_1-w_{10})\end{aligned} \tag{2.5}$$

Energy equation-

$$\rho c_p\left[\frac{\partial T}{\partial t}+u\frac{\partial T}{\partial x}+v\frac{\partial T}{\partial y}\right]=\left[\frac{\partial}{\partial x}\left(k\frac{\partial T}{\partial x}\right)+\frac{\partial}{\partial y}\left(k\frac{\partial T}{\partial y}\right)\right] \tag{2.6}$$

Species diffusion equation-

$$\rho\left(\frac{\partial w_1}{\partial t}+u\frac{\partial w_1}{\partial x}+v\frac{\partial w_1}{\partial y}\right)=\left[\frac{\partial}{\partial x}\left(\rho D\frac{\partial w_1}{\partial x}\right)+\frac{\partial}{\partial y}\left(\rho D\frac{\partial w_1}{\partial y}\right)\right] \tag{2.7}$$

The above equations are subjected to the following initial and boundary conditions:

For t < 0,

$$u = v = 0,\ T = T_{amb},\ w_1 = w_{1a}; \tag{2.8}$$

For t ≥ 0, at

Boundary I- air discharge. At the air discharge, flow is at uniform speed V_j, temperature T_j, and water vapor concentration $w_{1j,}$

$$u = 0,\ v = -V_j,\ T = T_j = T_C,\ w_1 = w_{1j} \text{ at } y = 0.4 \text{ m for } (0.1\text{m}-b_j) \le x \le 0.1\text{m} \tag{2.9}$$

When the air discharge is inclined

$$u = V_j\sin\theta,\ v = -V_j\cos\theta,\ T = T_j = T_C,\ w_1 = w_{1j} \text{ at } y = 0.4 \text{ m for } (0.1\text{m}-b_j) \le x \le 0.1\text{m} \tag{2.10}$$

Boundary II- inner vertical plate of the cavity. At the inner vertical plate we have no-slip condition and isothermal and impermeable conditions,

$$u = v = 0,\ T = T_C,\ \frac{\partial w_1}{\partial x} = 0 \text{ at } x = 0 \text{ for } 0.2\text{m} \le y \le 0.4\text{m} \tag{2.11}$$

Boundary III- upper and bottom plates of the cavity. At the upper and bottom plates of the cavity we have adiabatic, impermeable and no-slip conditions,

$$u = v = 0,\ \frac{\partial T}{\partial y} = 0,\ \frac{\partial w_1}{\partial y} = 0 \text{ at } y = 0.2 \text{ m and } 0.4\text{m for } 0 \le x \le 0.1\text{m} \tag{2.12}$$

Boundary IV- return grilles of the air curtain. At the return grilles, the vertical velocity, temperature and concentration gradients are assumed to be negligibly small,

$$u = 0,\ \frac{\partial v}{\partial y} = \frac{\partial T}{\partial y} = \frac{\partial w_1}{\partial y} = 0 \quad \text{at y =0.2 m for } (0.1\text{m-b}_\text{j}) \le x \le 0.1\text{m} \tag{2.13}$$

Boundary V- surrounding boundary I- At the upper boundary of the surrounding, the vertical gradient of the air velocity is assumed to be very small and the air is at ambient temperature and water vapor concentration,

$$\frac{\partial u}{\partial y} = \frac{\partial v}{\partial y} = 0,\ T = T_{amb}, w_1 = w_{1a} \quad \text{at y =0.6 m} \tag{2.14}$$

Boundary VI- surrounding boundary II- At the outer surrounding horizontally far from the cavity the horizontal gradients of the air velocity is assumed to be rather small, and the pressure, temperature and water vapor concentration are assumed at the ambient values,

$$\frac{\partial u}{\partial x} = \frac{\partial v}{\partial x} = 0,\ \text{p} = \text{P}_\text{amb},\ \text{T} = \text{T}_\text{amb},\ \text{w}_1 = \text{w}_\text{1a},\ \text{at x =0.8 m} \tag{2.15}$$

Boundary VII- ground boundary- At the ground boundary we have adiabatic, impermeable and no-slip conditions,

$$\text{u} = \text{v} = 0,\ \frac{\partial T}{\partial y} = 0,\ \frac{\partial w_1}{\partial y} = 0 \quad \text{at y=0 for } x \ge 0.1m \tag{2.16}$$

Boundary VIII- other solid boundaries- At the other vertical solid boundaries at x = 0.1 m the flow is subjected to the adiabatic, impermeable and no-slip conditions,

$$\text{u} = \text{v} = 0,\ \frac{\partial T}{\partial x} = 0,\ \frac{\partial w_1}{\partial x} = 0 \quad \text{at } \begin{cases} x = 0.1m, \text{ for } 0 \le y \le 0.2m \\ x = 0.1m, \text{ for } 0.4 \le y \le 0.6m \end{cases} \tag{2.17}$$

Some of these hydrodynamic and thermal boundary conditions are specified in Fig. 2.2. Using the non-dimensional variables

$$X = \frac{x}{H} \qquad Y = \frac{y}{H} \qquad U = \frac{u}{V_j}$$

$$P = \frac{p_m}{\rho_o \cdot V_j^{\,2}} \qquad V = \frac{v}{V_j} \qquad \Theta = \frac{T - T_C}{T_{amb} - T_C}$$

$$W_1 = \frac{w_{1a} - w_1}{w_{1a} - w_{1_j}} \qquad \Pr = \frac{\nu_0}{\alpha_0} = \frac{C_{p0}\mu_0}{k_0} \qquad Ra_t = \frac{g\beta_t\left(T_{amb} - T_C\right)H^3}{\alpha_0\nu_0}$$

$$Re_b = \frac{V_j b_j}{\nu_0} \qquad Sc = \frac{\nu_0}{D_0} \qquad N = \frac{\beta_m\left(w_{1_a} - w_{1_j}\right)}{\beta_t\left(T_{amb} - T_C\right)}$$

$$A = \frac{H}{b_j} \qquad \lambda_\rho = \frac{\rho}{\rho_0} = 1 \qquad \lambda_\mu = \frac{\mu}{\mu_0}$$

$$\lambda_{cp} = \frac{C_p}{C_{p0}} \qquad \lambda_k = \frac{k}{k_0} \qquad \lambda_D = \frac{D}{D_0}$$

$$\tau = \frac{t}{H/V_j} \qquad Ri = \frac{Gr_t}{\mathrm{Re}_b^{\,2}} = \frac{g\beta\left(T_{amb} - T_C\right)H^3}{V^2{}_j b_j^{\,2}}$$

$$Gr_t = \frac{g\beta\left(T_{amb} - T_C\right)H^3}{\nu_0^{\,2}}$$

The basic flow equations can be written in dimensionless form as

Continuity equation-

$$\frac{\partial(\lambda_\rho U)}{\partial X} + \frac{\partial(\lambda_\rho V)}{\partial Y} = 0 \qquad (2.18)$$

x- momentum equation-

$$\lambda_\rho\left(\frac{\partial U}{\partial \tau}+U\frac{\partial U}{\partial X}+V\frac{\partial U}{\partial Y}\right)$$
$$=-\frac{\partial P}{\partial X}+\frac{1}{Re_b A}\left[\frac{\partial}{\partial X}\left(\lambda_\mu\frac{\partial U}{\partial X}\right)+\frac{\partial}{\partial Y}\left(\lambda_\mu\frac{\partial U}{\partial Y}\right)\right] \tag{2.19}$$

y- momentum equation-

$$\lambda_\rho\left(\frac{\partial V}{\partial \tau}+U\frac{\partial V}{\partial X}+V\frac{\partial V}{\partial Z}\right)$$
$$=-\frac{\partial P}{\partial Y}+\frac{1}{Re_b A}\left[\frac{\partial}{\partial X}\left(\lambda_\mu\frac{\partial V}{\partial X}\right)+\frac{\partial}{\partial Y}\left(\lambda_\mu\frac{\partial V}{\partial Y}\right)\right]+\frac{Gr_t}{\left(Re_b\right)^2\cdot A^2\cdot}\cdot\left(\Theta+NW_1\right) \tag{2.20}$$

$$=-\frac{\partial P}{\partial Y}+\frac{1}{Re_b A}\left[\frac{\partial}{\partial X}\left(\lambda_\mu\frac{\partial V}{\partial X}\right)+\frac{\partial}{\partial Y}\left(\lambda_\mu\frac{\partial V}{\partial Y}\right)\right]+\frac{Ri}{A^2}\cdot\left(\Theta+NW_1\right) \tag{2.21}$$

Energy equation-

$$\lambda_\rho\lambda_{cp}\left(\frac{\partial \Theta}{\partial \tau}+U\frac{\partial \Theta}{\partial X}+V\frac{\partial \Theta}{\partial Y}\right)$$
$$=\frac{1}{PrRe_b A}\left[\frac{\partial}{\partial X}\left(\lambda_k\frac{\partial \Theta}{\partial X}\right)+\frac{\partial}{\partial Y}\left(\lambda_k\frac{\partial \Theta}{\partial Y}\right)\right] \tag{2.22}$$

Species equation

$$\lambda_\rho\left(\frac{\partial W_1}{\partial \tau}+U\frac{\partial W_1}{\partial X}+V\frac{\partial W_1}{\partial Y}\right)$$
$$=\frac{1}{Re_b Sc A}\left[\frac{\partial}{\partial X}\left(\lambda_\rho\lambda_D\frac{\partial W_1}{\partial X}\right)+\frac{\partial}{\partial Y}\left(\lambda_\rho\lambda_D\frac{\partial W_1}{\partial Y}\right)\right] \tag{2.23}$$

The above non-dimensional governing equations are subjected to the following initial and boundary conditions:

For t < 0,

$$\mathrm{U}=\mathrm{V}=0,\quad \Theta=1,\quad W_1=0\,. \tag{2.24}$$

For t ≥ 0,

Boundary I- air discharge. At the air discharge,

$$U = 0,\ V = -1,\ \ \Theta = 0, W_1 = 1 \ \text{ at } Y = 2 \quad \text{for } \ (0.5 - {b_j}/{H}) \le X \le 0.5 \tag{2.25}$$

When the air discharge is inclined

$$U = \sin\theta,\ V = -\cos\theta,\ \ \Theta = 0, W_1 = 1 \ \text{ at } Y = 2 \text{ for } \ (0.5 - {b_j}/{H}) \le X \le 0.5 \tag{2.26}$$

Boundary II- inner vertical plate of the cavity. At the inner vertical plate

$$U = V = 0,\ \ \Theta = 0,\ \frac{\partial W_1}{\partial X} = 0 \ \text{ at } \ X = 0 \qquad \text{for } 1 \le Y \le 2 \tag{2.27}$$

Boundary III- upper and bottom plates of the cavity. At the upper and bottom plates of the cavity,

$$U = V = 0,\ \frac{\partial \Theta}{\partial Y} = 0,\ \frac{\partial W_1}{\partial Y} = 0 \text{ at } Y = 1 \text{ and } 2 \quad \text{for } 0. \le X \le 0.5 \tag{2.28}$$

Boundary IV- return grilles of the air curtain. At the return grilles,

$$U = 0,\ \frac{\partial V}{\partial Y} = \frac{\partial \Theta}{\partial Y} = \frac{\partial W_1}{\partial Y} = 0 \ at \ Y = 1 \quad \text{for } \ (0.5 - {b_j}/{H}) \le X \le 0.5 \tag{2.29}$$

Boundary V- surrounding boundary I- At the upper boundary of the surrounding,

$$\frac{\partial U}{\partial Y} = \frac{\partial V}{\partial Y} = 0,\ \Theta = 1,\ W_1 = 0 \text{ at } Y = 3 \tag{2.30}$$

Boundary VI- surrounding boundary II- At the outer surrounding horizontally far from the cavity,

$$\frac{\partial U}{\partial X} = \frac{\partial V}{\partial X} = 0,\ \mathrm{P} = 0,\ \Theta = 1, \mathrm{W}_1 = 0 \text{ at } X = 4 \tag{2.31}$$

Boundary VII- ground boundary- at the ground boundary,

$$\mathrm{U} = \mathrm{V} = 0,\ \frac{\partial \Theta}{\partial Y} = 0, \frac{\partial W_1}{\partial Y} = 0 \text{ at Y=0 for } X \geq 0.5 \tag{2.32}$$

Boundary VIII- other solid boundaries- at the other vertical solid boundaries,

$$\mathrm{U} = \mathrm{V} = 0,\ \frac{\partial \Theta}{\partial X} = 0\ ,\ \frac{\partial W_1}{\partial X} = 0 \text{ at } \begin{cases} X = 0.5, \text{ for } 0 \leq Y \leq 1 \\ X = 0.5, \text{ for } 2 \leq Y \leq 3 \end{cases} \tag{2.33}$$

Some of these nondimensional boundary conditions are shown in Figure 2.2.

2.3 Installation of Secondary Air Curtain

In this study we move further to investigate the possible improvement of the cabinet performance by installing a secondary air curtain, as schematically shown in Figure 2.4. This newly added air curtain is placed at the upper boundary of the computational domain and its location, width, temperature and jet speed can be varied.

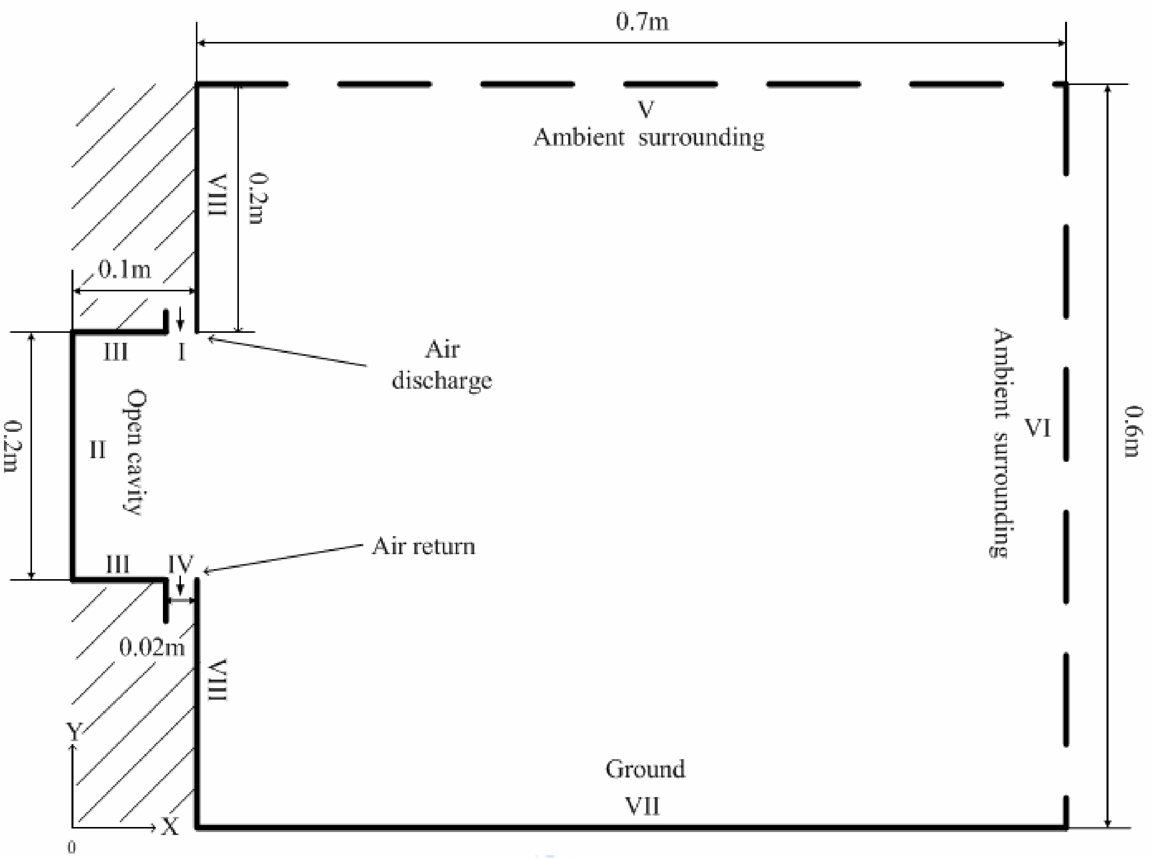

Fig. 2.1 Physical model for a vertical refrigerated display case.

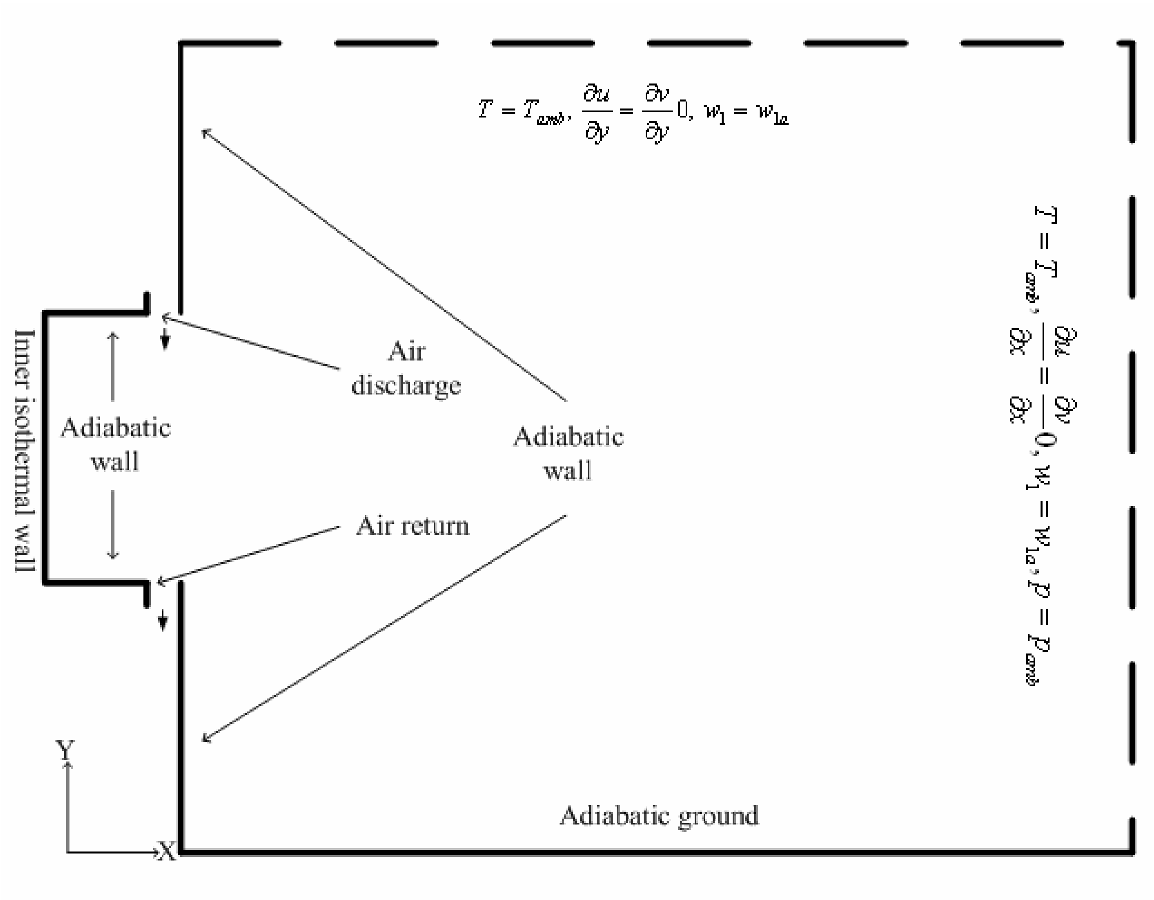

Fig. 2.2 Schematic diagram illustrating the geometry and some boundary conditions.

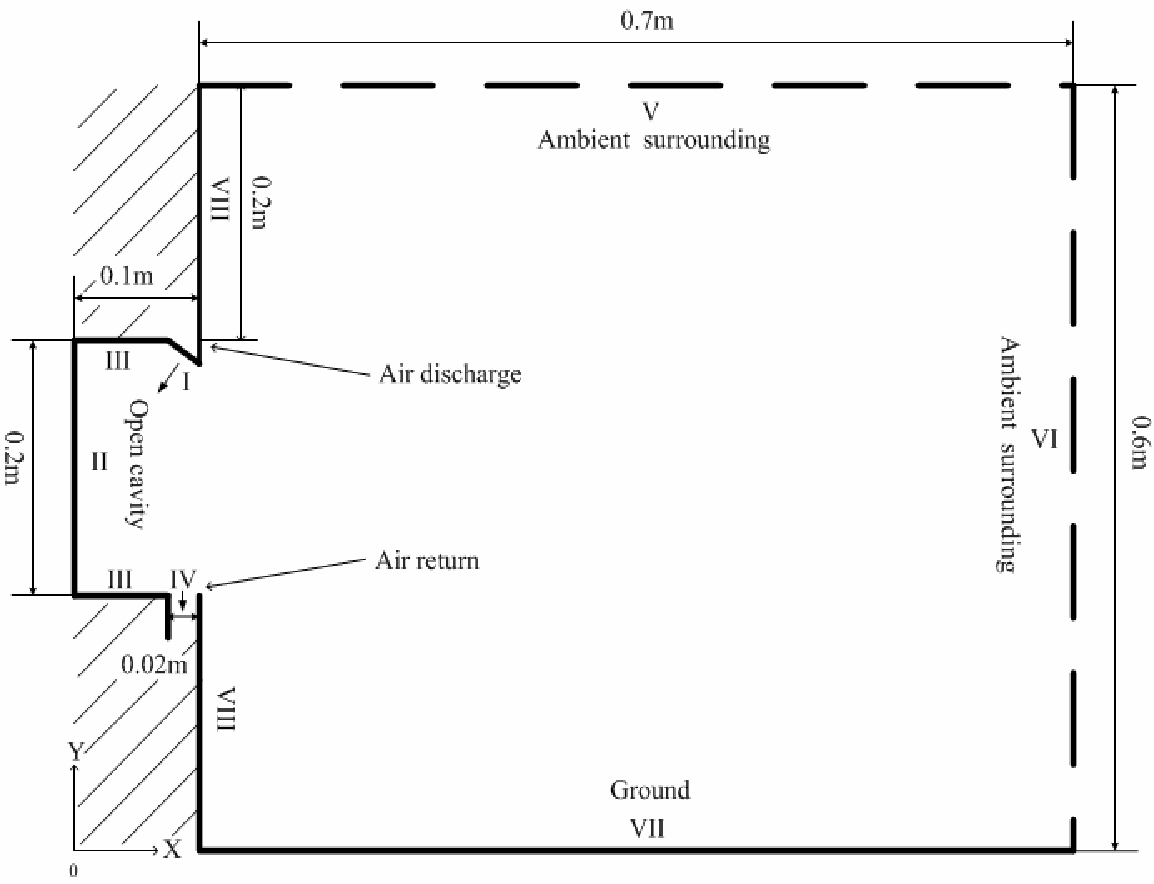

Fig. 2.3 Physical model for a vertical refrigerated display case with an inclined angle air curtain discharge

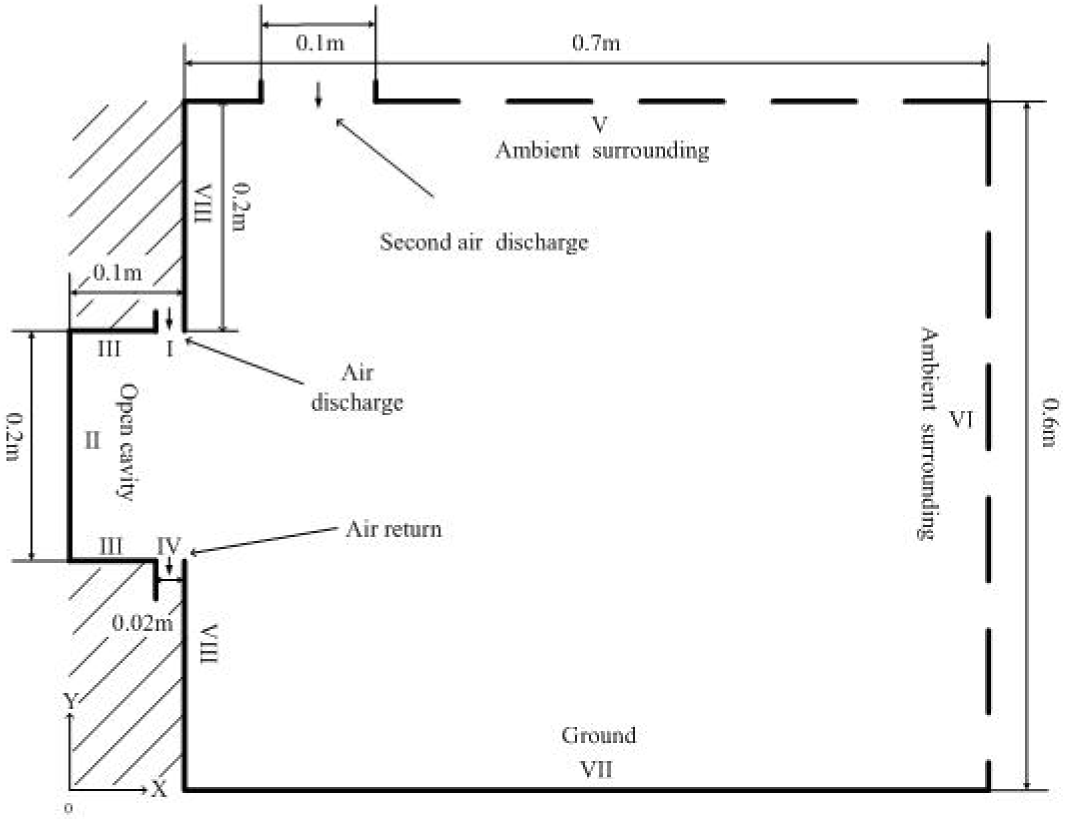

Fig. 2.4 Physical model for a vertical refrigerated display case covered by a second air jet.

CHAPTER 3

SOLUTION METHOD

The solution method to be used in the present study and the verification of its applicability to predict the transport processes in the open cavity flow considered here are detailed in this chapter. The grid distribution in the computing domain for this numeral scheme is also verified by comparing the predicted results with that in the open literature.

3.1 Numerical Scheme and Solution Procedures

The governing differential equations described in Chapter 2 are discretized by the SIMPLE algorithm [38] which applies the finite volume (FV) method to the partial differential equations. In this study, these discretized equations are solved by the commercial software PHOENICS [42], which implements the scheme of SIMPLE with an interactive Windows environment. More specifically, the differential equations are integrated over the chosen individual computational cells during a finite time increment in the present transient formulation. The values of the dependent physical variables are approximated by the hybrid difference method. The thermal and transport properties located at the central node are calculated by means of center average for each cell in the computation domain. For convenience, the general conservation equations are expressed as

$$\frac{1}{\sqrt{g}}\frac{\partial}{\partial t}\left(\sqrt{g}\rho\phi\right)+div\left(\rho\bar{u}\phi-\Gamma_{\phi}grad\phi\right)=s_{\phi} \tag{3.1}$$

where $\bar{u}$ represents u, v or w; φ could express any of the dependent variables, like u, v, T and w_1 ; Γ_{ϕ} and s_{ϕ} are respectively the associated diffusion and source coefficients. Here $\sqrt{g}$ is a metric tensor.

Now Eq. (3.1) can be integrated over a closed surface S valid for an arbitrary control volume $\forall$ to give

$$\frac{d}{dt}\int_{\forall}\rho\phi dV + \int_{S}\left(\rho\vec{u}\phi - \Gamma_{\phi} grad\phi\right)\cdot d\vec{S} = \int_{\forall} s_{\phi} dV \qquad (3.2)$$

where $\vec{S}$ is the surface vector. If $\forall$ and S are respectively taken to be the volume V_p and discrete faces $S_j\,(j=1,N_f)$ of a computational cell as that in Fig. 3.1, Eq. (3.2) becomes

$$\frac{d}{dt}\int_{V_p}\rho\phi dV + \sum_{j}\int_{S_j}\left(\rho\vec{u}\phi - \Gamma_{\phi} grad\phi\right)\cdot d\vec{S} = \int_{V_p} s_{\phi} dV \qquad (3.3)$$

For convenient discussion, the first and second terms on the left hand side of Eq. (3.3) are represented by T_1 and T_2, respectively. And T_3 represents the right-hand side of Eq. (3.3). Here T_1 is discretised as

$$T_1 \approx \frac{(\rho\phi V)_P^n - (\rho\phi V)_P^o}{\delta t} \qquad (3.4)$$

where the subscript “P” in Eq. (3.4) means the node P, and the superscripts “n” and “o” denote the new value and old value, respectively.

The second term T_2 can be separated into convection and diffusion terms by the separate contributions C_j and E_j, respectively. Thus T_2 can be approximated by the average value over each face of the cell as

$$T_2 \approx \sum_j \left(\rho \bar{u} \phi \cdot \vec{S}\right)_j - \sum_j \left(\Gamma_\phi grad\phi \cdot \vec{S}\right)_j \equiv \sum_j C_j - \sum_j E_j \tag{3.5}$$

Upwind differencing is used to approximate the convection term C_j as shown in Fig. 3.2:

$$C_j \equiv \left(\rho \bar{u} \cdot \vec{S}\right)_j \cdot \phi_P, \qquad \text{for } F_j \geq 0 \tag{3.6}$$

$$C_j \equiv \left(\rho \bar{u} \cdot \vec{S}\right)_j \cdot \phi_{N+}, \qquad \text{for } F_j < 0 \tag{3.7}$$

where F_j is defined as $F_j = \rho \vec{u}_j \cdot \vec{S}_j$ And the diffusion term E_j is represented by the face-centred expressions as

$$E_j \approx \Gamma_{\phi,j} \left\{ f_j^l (\phi_N - \phi_P) + \left\lfloor \vec{\nabla}\phi \cdot \vec{S} - f_j^l \vec{\nabla}\phi \cdot \vec{d}_{PN} \right\rfloor_j \right\} \tag{3.8}$$

where f_j is a geometry factor, $\vec{d}_{PN}$ is the vector from P to N, $\Gamma_{\phi,j}$ is the diffusion coefficient at the surface.

Finally, T_3 can be expressed as

$$T_3 \approx s_1 - s_2 \phi_P \tag{3.9}$$

Substitution of the results in Eqs. (3.4)-(3.9) into Eq. (3.3) gives

$$\frac{(\rho \phi V)^n - (\rho \phi V)^o}{\delta t} + \sum \rho \, \vec{u}_j \cdot \vec{S}_j = 0 \tag{3.10}$$

which can be put in a more compact form as

$$A_p \phi_P^n = \sum_m A_m \phi_m^n + s_1 + B_P \phi_P^o \tag{3.11}$$

where A_m represents the effects of the convection and diffusion and $\sum$ denotes the effects of the overall neighbor nodes shown in Fig. 3.2 for the flux discretisation. Besides, A_P is defined as $\sum_m A_m + s_2 + B_P$ and B_P is equal to $(\rho V)^o / \delta t$.

When implementing the above solution method, the convergence criterion at each time step is chosen as

$$C_\phi^k = \sum \left(\left| B_P^n \phi_P^n \right| - \left| B_P^o \phi_P^o \right| \right) < \text{the chosen conservative value} \tag{3.12}$$

We set the conservative values of velocity, pressure and temperature fields all at 0.001 in this study. The simulation procedures are briefly illustrated by the flow chart shown in Fig. 3.3.

3.2 Verification of Numerical Scheme

The computation domain includes the entire air curtain, cavity and ambient. The above solution method is verified by two typical ways: the grid independence test and comparison with the published computational results.

3.2.1 Grid independence test

The grid distribution is frequently an important issue in numerical computation. It affects the efficiency and accuracy of a thermofluid analysis. The grid distribution for numerical simulation of the transport processes in the display cabinet investigated here is shown in Fig. 3.4. The grid number for the air jet region is 6 × 45 and inside the display cabinet we place 21 × 45 grids. We place a 127 × 28 grids for the bottom surrounding region ($0 \le y \le 0.2$ m). Specifically,

21 × 28 grids for $0 \le x \le 0.08$ m and $0 \le y \le 0.2$ m,

6 × 28 grids for $0.08 \le x \le 0.1$ m and $0 \le y \le 0.2$ m,

100 × 28 grids for $0.1 \le x \le 0.8$ m and $0 \le y \le 0.2$ m,

In the middle region ($x \geq 0.1$m and $0.2\text{m} \leq y \leq 0.4$m) a 100 × 45 grid is chosen. And in the upper region ($0.4 \leq y \leq 0.6$m) the grid is 127 × 31. Specifically,

21 × 31 grids for $0 \leq x \leq 0.08$m and $0.4 \leq y \leq 0.6$m,

6 × 31 grids for $0.08 \leq x \leq 0.1$m and $0.4 \leq y \leq 0.6$m,

100 × 31 grids for $x \geq 0.1$m and $0.4 \leq y \leq 0.6$m,

Hence a total of 13,208 cells are used in the computation. It should be pointed out that in each region uniform grids are placed. For the cases with $b_j = 0.02$ m, $V_j = 0.07\text{-}0.5$ m/s, and $\Delta T = T_{amb} - T_c = 20$ ℃ in the absence of mass transfer effects, the computed results using this grid distribution are compared with the results computed from the 4,047 and 20,375 cells by showing the velocity components u and v at y = 0.3m in Figs. 3.5 and 3.6. Selected results to compare the magnitude of the velocity calculated from these three different grids are shown in Fig. 3.7 at steady state. It is noted that the results from the 13,208 and 20,375 cells are in good agreement. Besides, we compare the flow pattern, isotherms and iso-concentration lines computed from these three grid distributions in Figs. 3.8, 3.9 and 3.10 for another case with the presence of mass transfer. The predicted vortex flow patterns revealed from the velocity vector maps, isothermal and iso-concentration lines from the 13,208 and 20,375 cells are also in good agreement. Thus the computation model with the 13,208 cells is considered to be suitable in predicting the transport processes in the vertical display cabinet examined in the present study. Hence the grid distribution with the 13, 208 cells is used in the subsequent computation.

3.2.2 Domain Size Test

The domain size will sometimes affect the numerical results and needs to be tested in the present study. Selected results from the present domain size test are shown in Figs. 3.11-3.13. More specifically, the velocity vector map, isotherms and concentration contours for the case examined above at steady state computed from three different domain sizes are contrasted in Figs. 3.11-3.13. Noted that the results predicted from the domain size of 0.8 × 0.6 m^2 are in good agreement with that from the size of 1 × 0.6 m^2. Thus the computation model with the domain size 0.8 × 0.6 m^2 is considered to be suitable in predicting the transport processes in the vertical display cabinet in the present study. Hence the domain size 0.8 × 0.6 m^2 is used in the subsequent computation.

3.2.3 Verification with Published Results

To further verify the proposed solution method, the present results for some limiting cases are compared with the computational data reported in the literature. This is illustrated in Figs. 3.14 and 3.15 by comparing our predicted steady cavity flow pattern and isotherms with that from Mhiri et al. [22] for the case with $Re_b = 100$, $Gr_t = 10{,}000$, $L/H = 1$ and $b_j/H = 1/20$ without considering the mass transfer. Note that our prediction is in qualitative agreement with the results from Mhiri et al. [22].

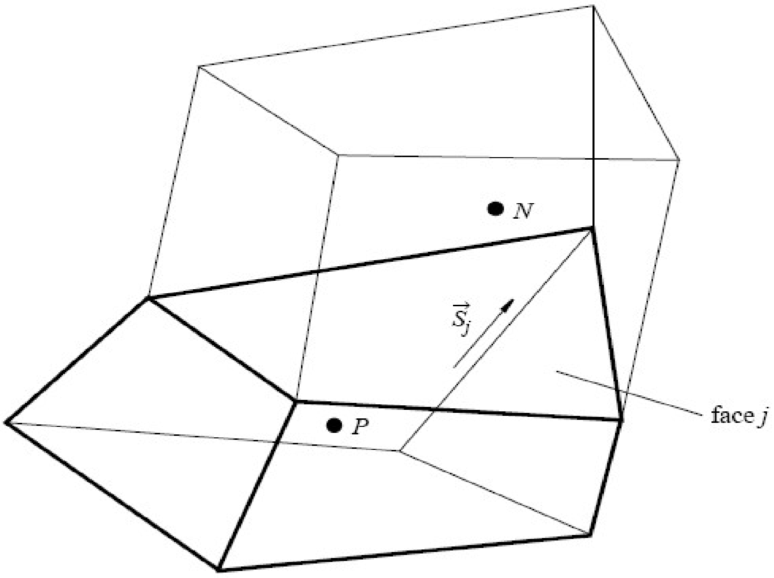

Fig. 3.1 The locations of the centred node P in a typical cell and centred node N in the neighbor cell.

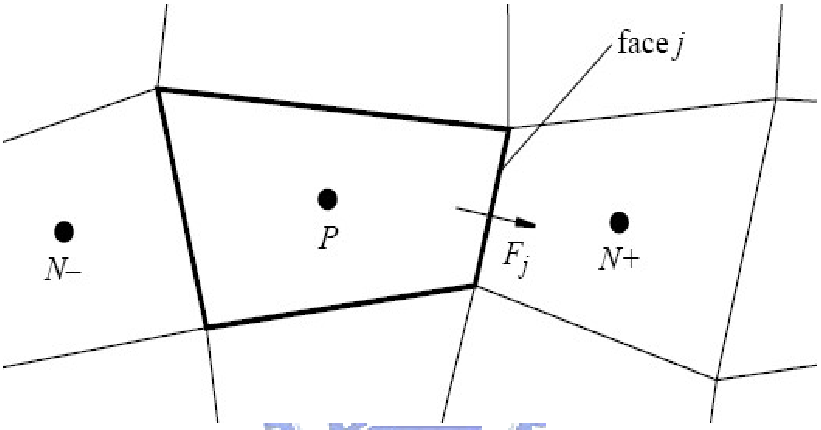

Fig. 3.2 The upwind differencing with node labeling for flux discretization.

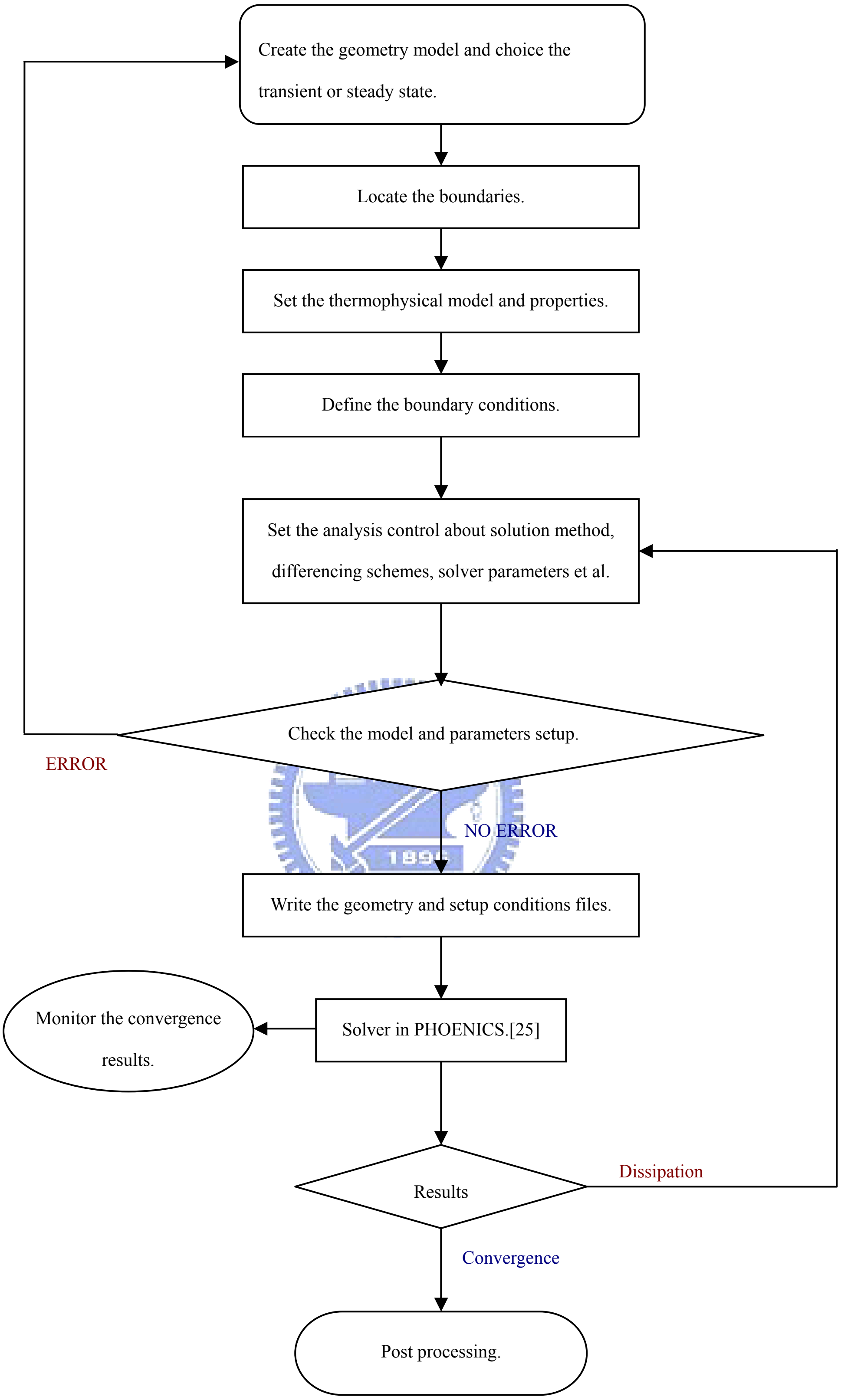

Fig. 3.3 Flow chart for the simulation procedures.

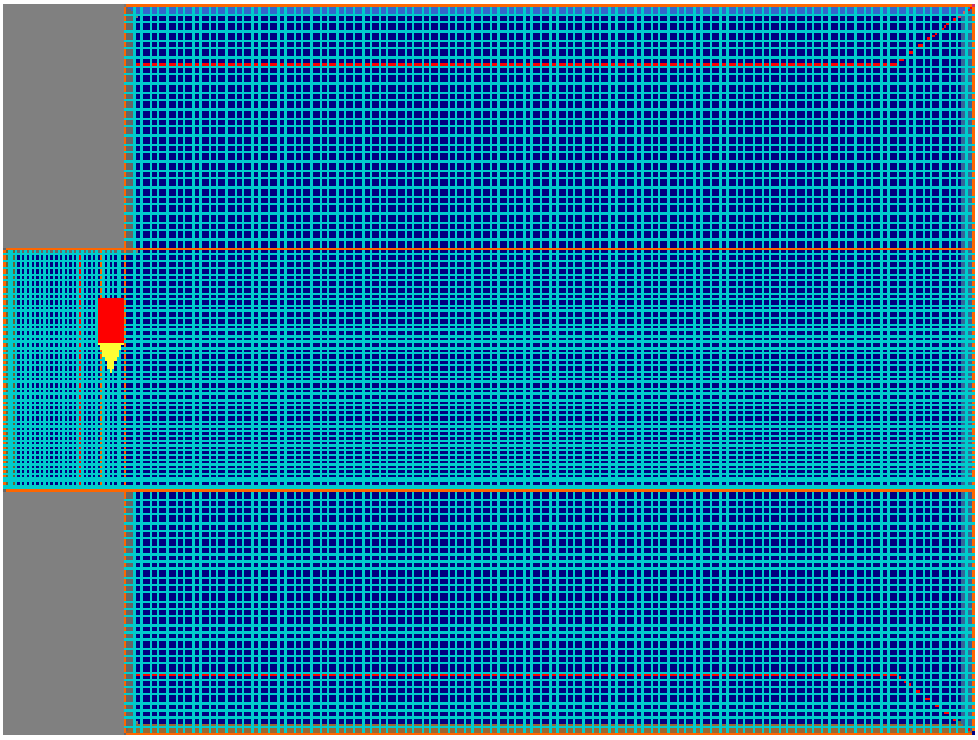

Fig. 3.4 The mesh distribution for the entire computational domain.

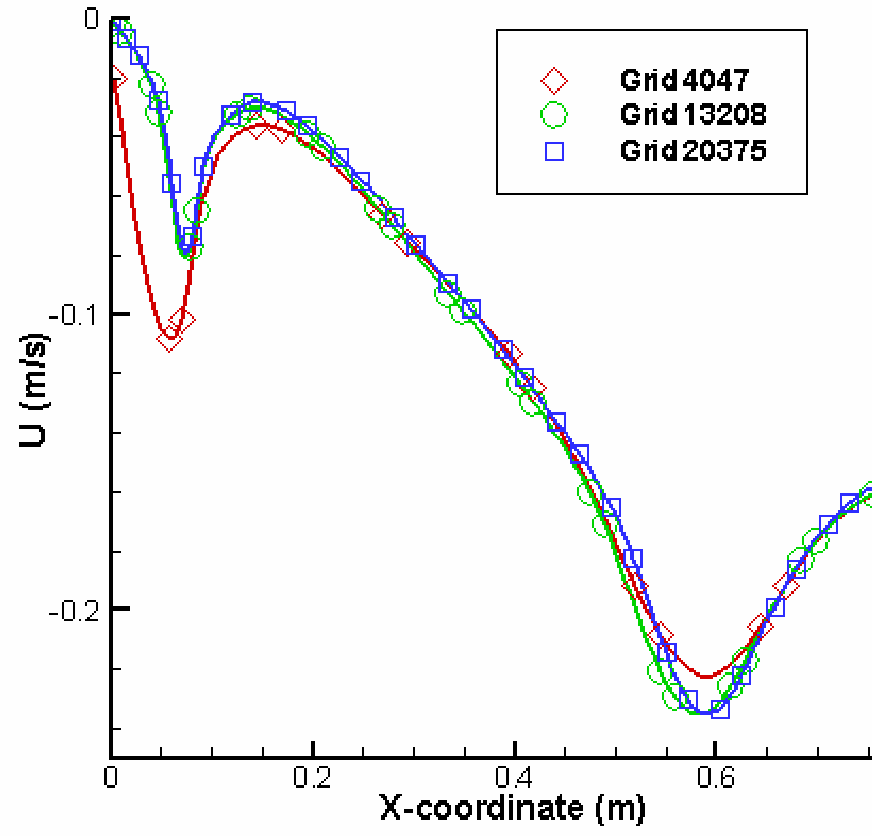

Fig. 3.5 The velocity U at the x-direction locations on the line y = 0.3 m predicted from three different grids for b_j = 0.02 m, V_j = 0.4 m/s, ΔT = 20 ℃ and N = 0.

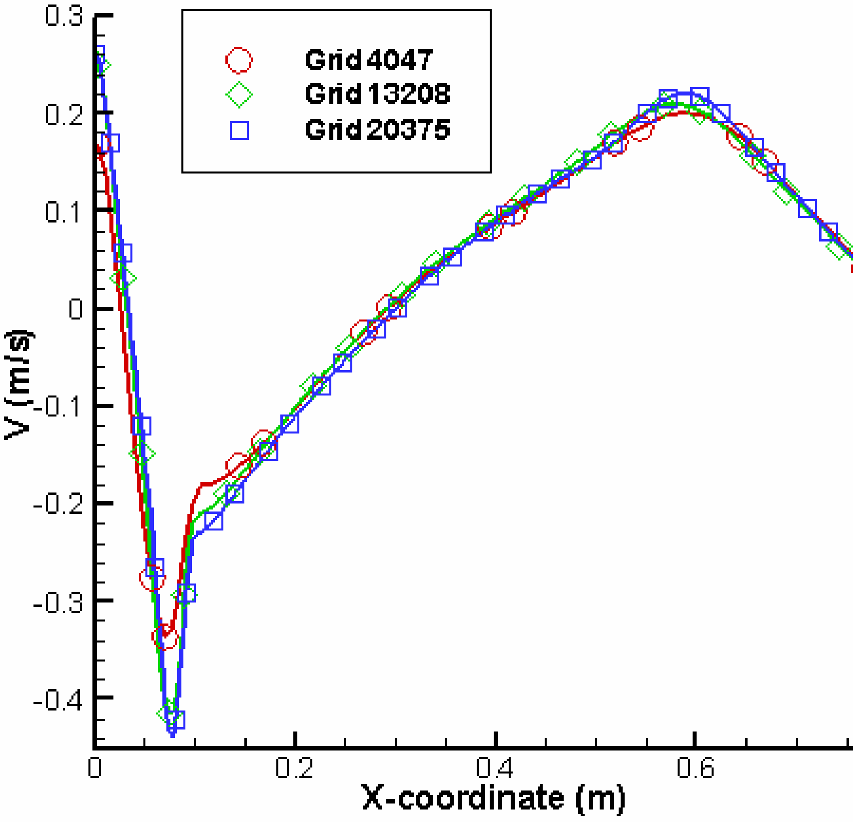

Fig. 3.6 The velocity V at the y-direction locations on the line y = 0.3 m predicted from three different grids for b_j = 0.02 m, V_j = 0.4 m/s, ΔT = 20 ℃ and N = 0.

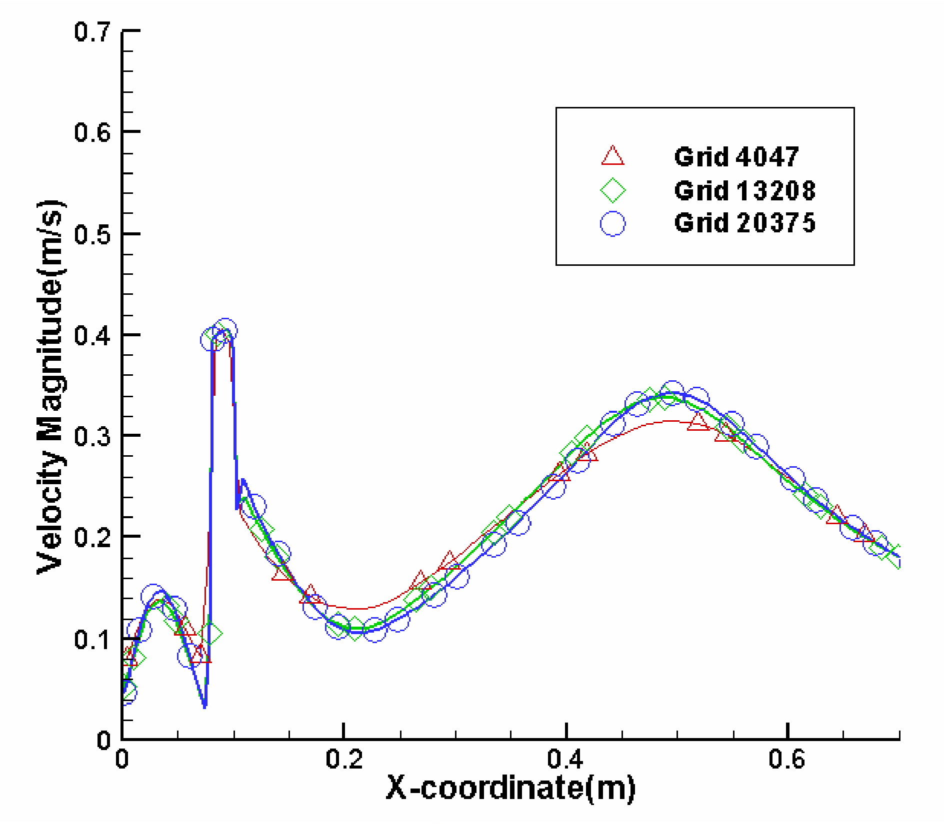

Fig. 3.7 The horizontal variations of the steady velocity magnitude at the selected locations on the line y = 0.385 m predicted from three different grids for b_j = 0.02 m, V_j = 0.4 m/s, ΔT = 20 ℃ and N = 0.

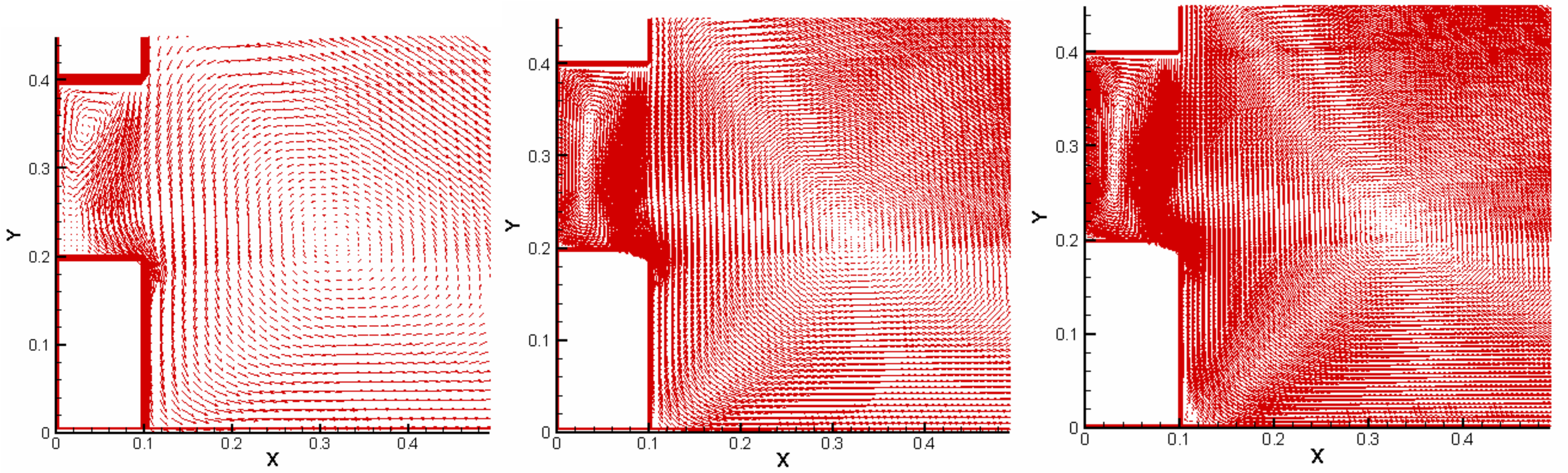

(a) (b) (c)

Fig. 3.8 Velocity vector maps at steady state for $b_j = 0.02m$, $\mathrm{Re}_b = 574.21, Gr_t = 2.71 \times 10^7$ $(\Delta T = 20^0 C)$ predicted from the grids with (a) 4,047 cells, (b) 13,208 cells, (c) 20,375 cells.

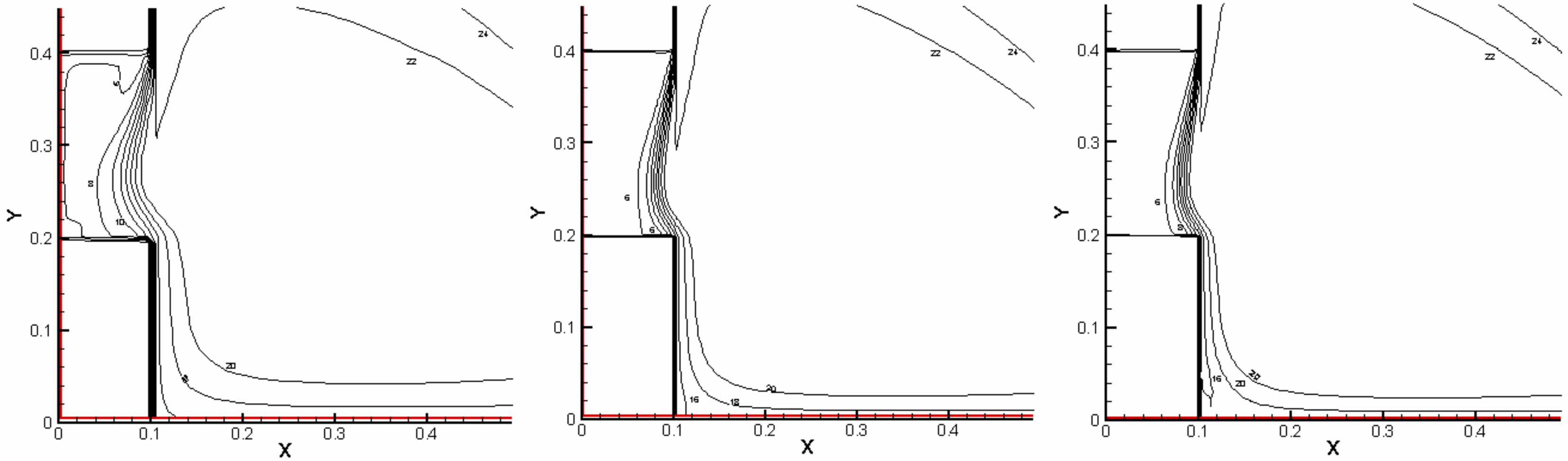

(a)

(b)

(c)

Fig. 3.9 Isotherms at steady state for $b_j = 0.02m$, $\mathrm{Re}_b = 574.21, Gr_t = 2.71 \times 10^7$ $(\Delta T = 20^0 C)$ predicted from the grids with (a) 4,047 cells, (b) 13,208 cells, (c) 20,375 cells.

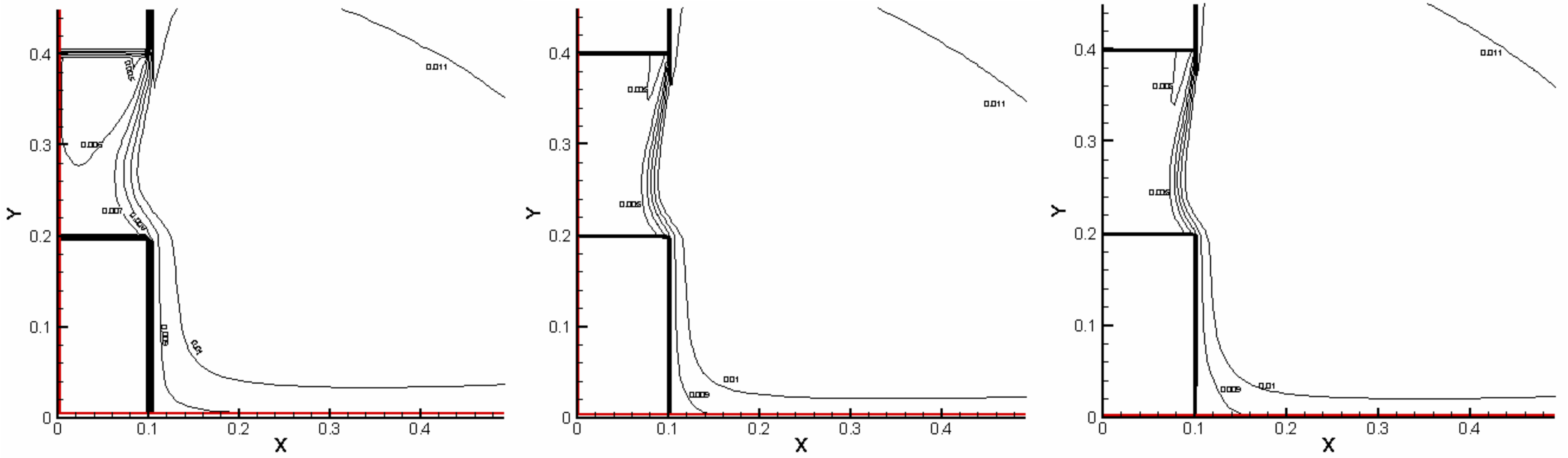

(a) (b) (c)

Fig. 3.10 Iso-concentration lines at steady state for $b_j = 0.02m$, $\mathrm{Re}_b = 574.21, Gr_t = 2.71\times10^7$ $(\Delta T = 20^0 C)$ predicted from the grids with (a) 4,047 cells, (b) 13,208 cells, (c) 20,375 cells.

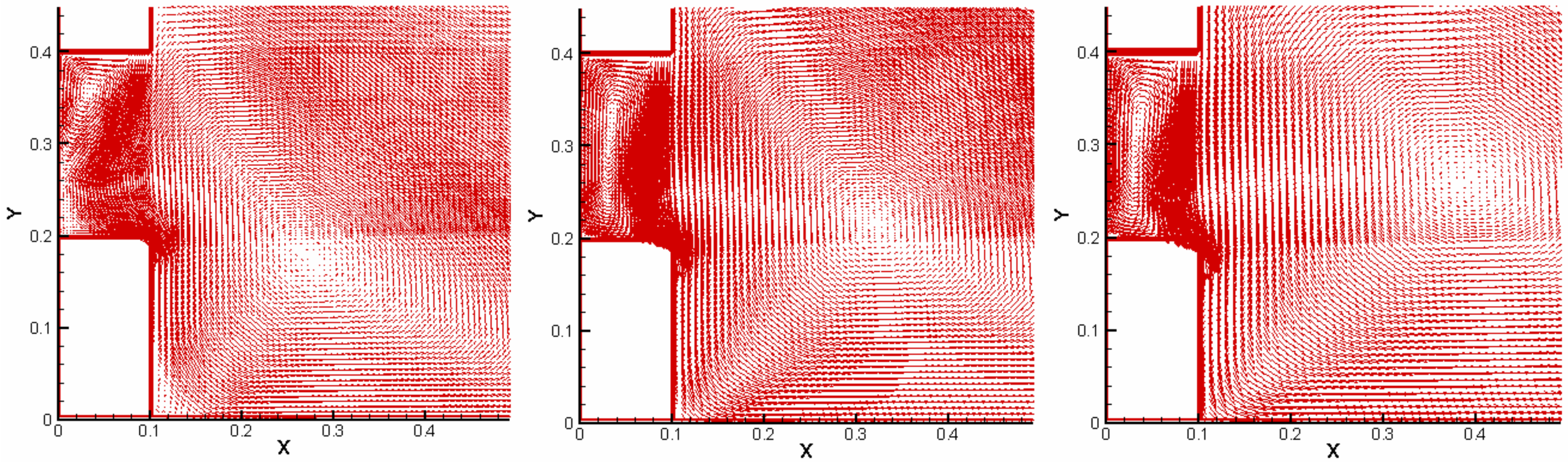

(a) (b) (c)

Fig. 3.11 Velocity vector maps at steady state for $b_j = 0.02m$, $\mathrm{Re}_b = 574.21$, $Gr_t = 2.71\times10^7$ $(\Delta T = 20^0 C)$ predicted with the domain size of (a) $0.6\times0.6\ m^2$, (b) $0.8\times0.6\ m^2$, (c) $1\times0.6\ m^2$.

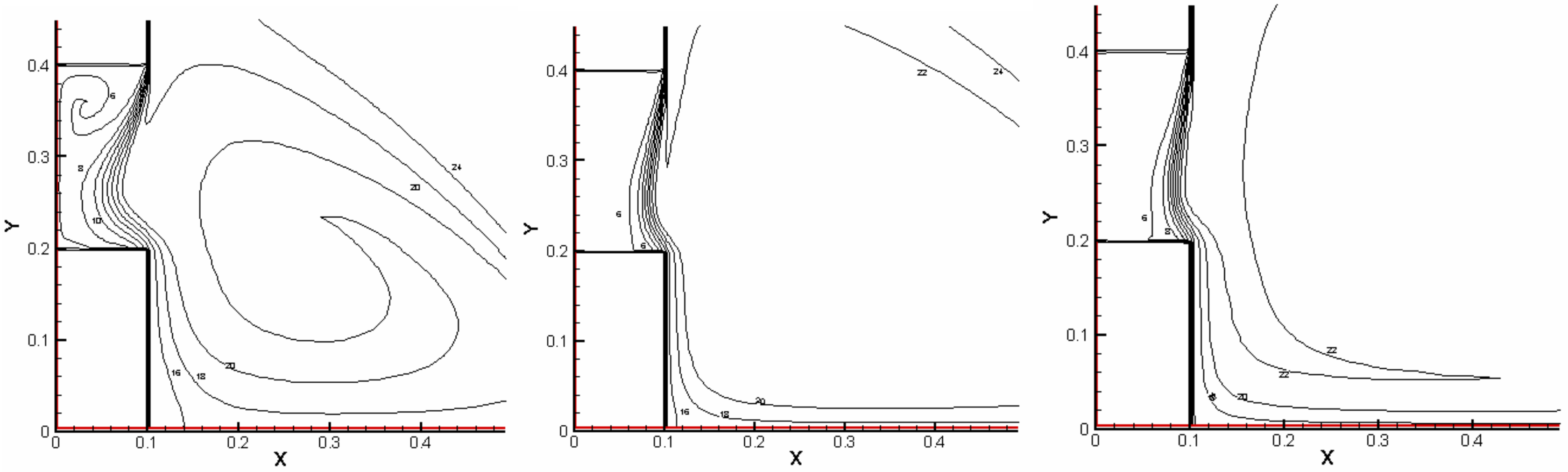

(a) (b) (c)

Fig. 3.12 Isotherms at steady state for $b_j = 0.02m$, $\mathrm{Re}_b = 574.21$, $Gr_t = 2.71\times10^7$ $(\Delta T = 20^0 C)$ predicted with the domain size of (a) $0.6\times0.6\ m^2$, (b) $0.8\times0.6\ m^2$, (c) $1\times0.6\ m^2$.

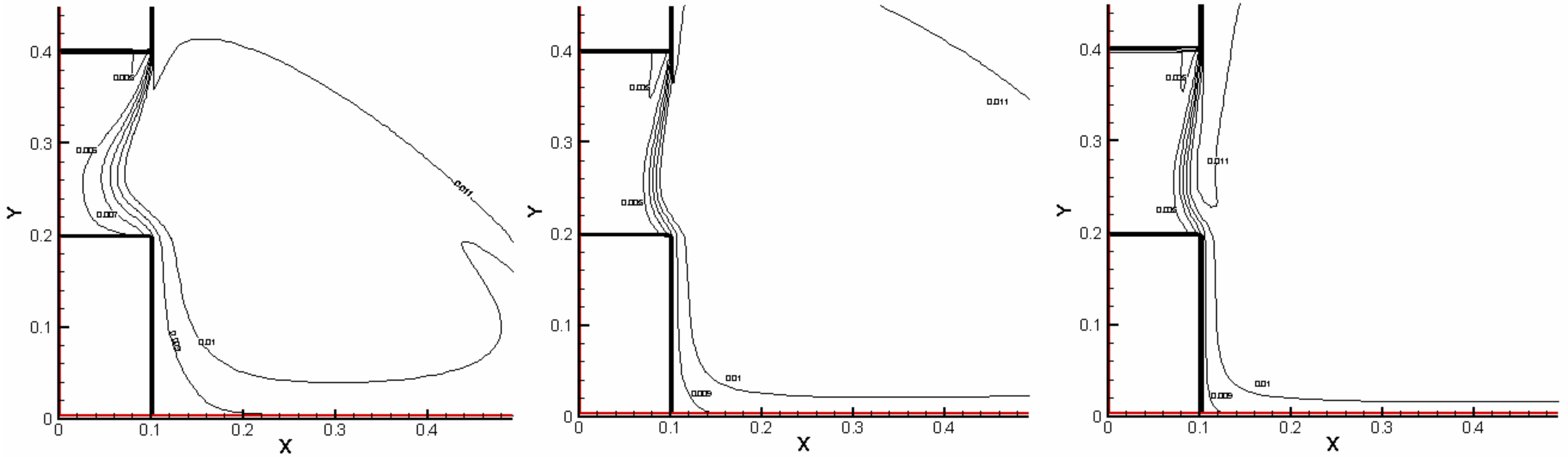

(a) (b) (c)

Fig. 3.13 Iso-concentration lines at steady state for $b_j = 0.02m$, $\mathrm{Re}_b = 574.21$, $Gr_t = 2.71\times10^7$ $(\Delta T = 20^0 C)$ predicted with the domain size of (a) $0.6\times0.6\ m^2$, (b) $0.8\times0.6\ m^2$, (c) $1\times0.6\ m^2$

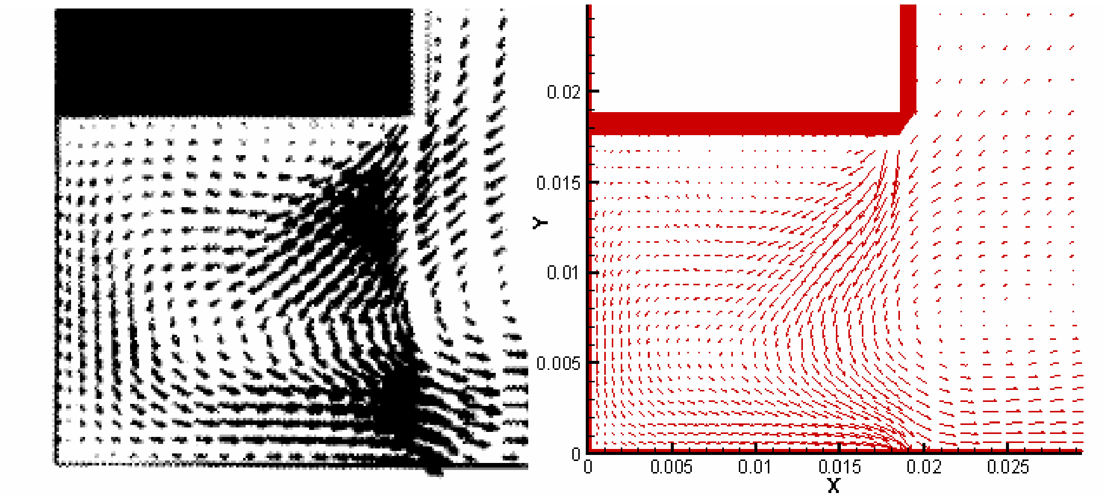

(a) (b)

Fig. 3. 14. Vector velocity maps in steady state cavity flow for $\mathrm{Re}_b = 100, Gr_t = 10{,}000$, L/H=1, $b_j / H = 1/20$ predicted from (a) Mhiri & Golli (1998) and (b) present study.

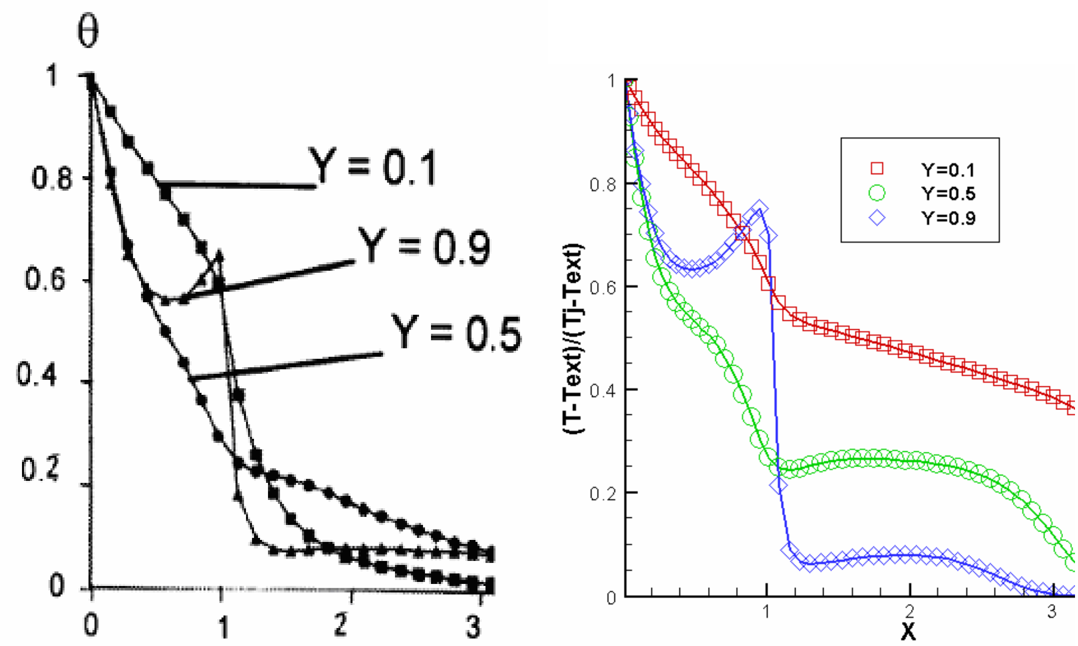

(a) (b)

Fig. 3. 15. Profiles of temperature in the cavity and the surrounding medium with $\mathrm{Re}_H = 100, Gr_t = 10000$, L/H=1, $b_j / H = 1/20$ predicted from (a) Mhiri et al.(1998) and (b) present study.

CHAPTER 4

RESULTS AND DISCUSSION

In the present numerical simulation of the transport processes in the open vertical refrigerated display case, computation is carried out mainly for the injection slot width varied from 0.016 m to 0.024m at the air discharge grille. Besides, no secondary air curtain is considered at first. The effects of the secondary air curtain will be investigated later. The air discharge-to-return grille separation distance H is fixed at 0.2 m and the cabinet depth is fixed at 0.1 m with the injected air velocity ranging from 0.0583 to 0.62 m/s and the temperature difference between the air discharge and ambient are varied from 0 to 20°C. The inner vertical plate of the case is at a uniform temperature of 5°C. The dimensionless groups governing the flow patterns are the jet Reynolds number based on the slot width at the air curtain discharge grille, thermal Grashof number, thermal-to-solutal buoyancy ratio, and thermal Richardson number (thermal buoyancy-to-inertia ratio). They are respectively defined as

$$Re_b = V_j b_j / \nu \tag{4.1}$$

$$Gr_t = g \beta_t \Delta T H^3 / \nu^2 \tag{4.2}$$

$$N = \beta_m (W_{1a} - W_{1j}) / \beta_t (T_{amb} - T_c) \tag{4.3}$$

and

$$Ri_t = Gr_t / {Re_H}^2 \tag{4.4}$$

Here the Reynolds number based on the cavity height H is defined as

$$Re_H = V_j H / \nu = Re_b \cdot (H / b_j) \tag{4.5}$$

Thus in this study the air curtain discharge Reynolds number Re_b ranges from 100.5 to 717.8, the Richardson number varied from 0.527 to 26.87 and N varied from 0 to 0.0635. At first, results from the present computation for the case in the absence of mass transfer in the flow (N = 0) are presented here to unravel how the jet Reynolds number, thermal Grashof number, thermal Richardson number, and the ratio H / b_j affect the flow patterns driven by the interaction of inertia force of the air curtain and the thermal buoyancy force in the vertical display cabinet. It should be mentioned that only the results at steady or statistical state will be examined in the following to investigate the long time behavior of the flow. Then, selected results with the simultaneous presence of heat and mass transfer will be inspected.

4.1 Jet Inertia-Driven Recirculating Flow for Un-cooled Air Curtain

At first, the effects of the jet Reynolds number at the air discharge grille on the predicted steady flow pattern for the limiting case in the absence of mass transfer (Δw_1 = 0) at b_j = 0.02 m and 0.016m for an un-cooled air curtain (Gr_t = 0) are presented in Figs. 4.1 and 4.2. Thus the open cavity flow is driven by the jet inertia alone. The results clearly show that a single large recirculating vortex is induced in the vertical cavity by the inertia force of the air curtain for all Re_b. Besides, at Gr_t = 0 and N = 0 the air curtain moves vertically downwards and the vortex in the cavity has not been cut apart. These results also show that for Gr_t = 0 and N = 0 the flow recirculation is stronger for a higher jet Reynolds number. Moreover, Fig. 4.3 shows that at the same jet Reynolds number the flow recirculation is stronger for the smaller air curtain width. It is attributed to the higher jet issuing speed for a smaller b_j.

4.2 Effects of Air Curtain Reynolds Number

For the case without the temperature difference between the air curtain and ambient for $\Delta T = 0℃$ and $\Delta w_1 = 0$, no buoyancy induced flow appears in the cavity for all jet Reynolds numbers. We can see how the jet Reynolds number at the air discharge grille affects the flow pattern in the vertical display cabinet from the results given in Figs. 4.1- 4.3. The flow patterns at steady state are all in the form of single large vortex circulating along the cavity walls and the air curtain. In the presence of a small temperature difference between the air curtain and ambient with $Gr_t = 6.78 \times 10^6$ ($\Delta T = 5^0 C$) the air curtain bends toward the cavity at low jet Reynolds number as it moves downwards, as shown in Figs. 4.4-4.7. In the simultaneous presence of temperature and concentration differences between the air jet and ambient with $Gr_t = 2.7 \times 10^7$ ($\Delta T = 20^0 C$), $N = 6.35 \cdot 10^{-2}$, the air curtain also bends toward the cavity for all Re_b tested for this higher Gr_t as it moves downwards, as shown in Figs. 4.8-4.10. And the bending is more significant for a lower Re_b, which obviously results from the increasing buoyancy-to-inertia ratio for a reduction in Re_b at fixed Gr_t and Gr_m. Thus the buoyancy force exhibits stronger effects on the flow. Note that the same trends are also observed in the cases of smaller air jet width, which are presented in Figs. 4.11-4.16. It is also noted that the isotherms and iso-concentration lines also bend significantly toward the cavity for a lower Re_b (Figs. 4.9(a) to (e) and Figs. 4.10(a) to (e)). The intrusion of the warm and humid air from the ambient into the cavity is relatively prominent. It is of interest to point out that at the very low Re_b of 100.5 the air jet is deflected toward the cavity immediately after it is discharged from the air injection slot and the intruding air from the ambient dominates the cavity. Similar trends are noted in Figs. 4.12-4.13 and Figs. 4.15-4.16 respectively for smaller jet discharge width of 0.02m and 0.016 m.

4.3 Effects of Richardson Number

Before examining our results, the important effects of the buoyancy on the cavity flow reported in the literature are given. In a vertically downward air jet moving over an open vertical cavity, Mhiri et al. [22] observed that the air curtain bent slightly inward by the action of the jet entrainment and the thermal buoyancy in the interior of the cavity. The velocity vector maps for the open cavity resulting from the negatively buoyant jet at different Ri_t predicted from Mhiri et al. [22] are shown in Fig.4.17 for the purpose of comparing with our predictions. The two cases presented in Fig.4.17 respectively correspond to predominant forced convection (Ri_t =0.04) and to dominated mixed convection (Ri_t =1.0). The thermal and aerodynamic protection from the external medium remains perfectly insured for the dominated forced convection case (Fig. 4.17 (a)), although a small deviation of the jet is observed. But the situation is very different when the mixed convection is important (Fig.4.17 (b)). Specifically, at high Ri_t there appears air jet bending into the cabinet under strong action of the buoyancy. The air curtain becomes relatively wide near the cavity bottom and it loses the strength to prevent the warm and moist air from the surrounding to penetrate into the cavity.

We proceed to examine how the recirculating flow in the cavity is affected by the Richardson number by inspecting the results predicted in the present study for various Re_H at given Gr_t. According to the definition $Ri_t = Gr_t / Re_H{}^2$, the thermal Richardson number is lower for a higher Re_H when Gr_t is fixed. The results in Fig. 4.6 clearly show that at lower Ri_t the recirculating flow resulting from the air curtain bending in the cavity becomes weaker and occupies a smaller region. This is due to the fact that at higher Re_b and Re_H the strength of the jet inertia is stronger and the air curtain is less likely to be deflected by the intruding air from the ambient. The buoyancy effects on the flow are hence weaker for smaller Ri_t and Ri_m. Moreover, the thermal and solutal Richardson numbers for the cases considered here are listed in Table 4.1.

4.4 Effects of *H / b_j* Ratio

Next, the effects of the ratio between the cavity height and jet width at the air discharge grille on the recirculating flow in the cavity are examined. According to the definition of the Richardson numbers,

$$Ri_t = Gr_t / Re_H{}^2 = \left(Gr_t / Re_b{}^2\right)\cdot\left(b_j / H\right)^2 \text{ and } Ri_m = Gr_m / Re_H{}^2 = \left(Gr_m / Re_b{}^2\right)\cdot\left(b_j / H\right)^2 .$$

Thus for given Gr_t, Gr_m and Re_b the Richardson numbers are decreasing with a reduction in the air curtain width at the air discharge grille. Hence the effects of the H / b_j on the flow can be inferred by comparing the corresponding results in Figs. 4.8 to 4.10 for b_j = 0.024 m with that in Figs. 4.11 to 4.13 for b_j = 0.002 m and Figs. 4.14 to 4.16 for b_j = 0.016 m for the same Gr_t, Gr_m and Re_b. Note that an increase in the H / b_j ratio causes a reduction in the Richardson numbers and hence weakens the buoyancy effects. By comparing the results for the isotherms and iso-concentration lines, the effects can be more clearly seen. Specifically, at a larger H / b_j the distortions in the isotherms and iso-concentration lines are less severe to a certain degree.

4.5 Effects of the Air Discharge with an Inclined Angle

Based on the present predictions, the thermal and solutal buoyancies tend to deflect the initially vertically downward moving air curtain toward the cavity core and to induce the intrusion of the warm, moist air from the ambient into the cavity. This apparently results in a significant reduction of the performance of the display cabinet. The modified simplifying physical model in a vertical refrigerated display case adopted here is a two-dimensional vertical downward cold air discharge with an inclined angle, as schematically shown in Fig.2.3. According to this observation, we proceed further to investigate the possibility of retarding the air curtain bending by inclining the jet at the air discharge grille toward the ambient. Results from this investigation are shown in Figs. 4.18 to 4.53 for various jet slot width and inclined angles. The jet inclined angle is defined as the angle between the axis of the jet issued at the discharge grille and a vertically downward line. Positive and negative inclined angles respectively denote the jet inclined toward the cavity and the ambient. Comparing the results in Figs. 4.18 to 4.20 for $\gamma = 15^\circ$ with that in Figs. 4.8 to 4.10 for $\gamma = 0^\circ$ for $b_j = 0.024$ m, the results in Figs. 4.30-4.32 for $\gamma = 15^\circ$ with that in Figs. 4.11-4.13 for $\gamma = 0^\circ$ for $b_j = 0.02$ m and the results in Figs. 4.42-4.44 for $\gamma = 15^\circ$ with that in Figs. 4.14-4.16 for $\gamma = 0^\circ$ for $b_j = 0.016$ m at the same Gr_t, N and Re_b clearly reveal that for an inclined jet the bending of the air curtain delays slightly and the ambient air intrusion into the cavity is slightly weaker. When $\gamma > 0$, at large inclined angle the delay in the air curtain bending is more significant and the distortions in the isotherms and iso-concentration lines are further reduced, as evident from the results in Figs. 4.21-4.23, Figs. 4.25-4.30 and Figs. 4.45-4.47, for the air injection slot width of 0.024, 0.02 and 0.016m, respectively. It is noted that a negative jet inclined angle, jet inclined toward the ambient, significantly delays the air curtain bending and the distortions in the isotherms and iso-concentration lines are reduced to some degree, as evident from comparing the results in Figs. 4.24-4.29, Figs. 4.36-4.41 and Figs. 4.48-4.53 with Figs. 4.8-4.16.

4.5 Effects of Installing a Secondary Air Curtain

Finally, how the installation of a secondary air curtain shown in Fig. 2.4, in addition to the original air curtain, affects the flow in the display cabinet is illustrated. Figures 4.54-4.56 show the predicted flow with the secondary air curtain located right adjacent to the original curtain with jet width of 0.01m and jet velocities of 0.1m/s and 0.4m/s with the jet temperature = T_{amb} computed by three different grids. Note that the results computed by the grid with 15,428 cells are in good agreement with that with

17,168 cells. Thus the grid with 17,168 cells is adopted in the subsequent computation.

The effects of the secondary air curtain width and location on the recirculating flow in the cabinet are shown in Figs. 4.57-4.59 for V_{2j}=0.1 m/s. The results indicate that at this low V_{2j} the effects of the jet width and location on the flow are rather slight. But at higher V_{2j} of 0.4 m/s and 0.7 m/s, installing the jet some distance away from the cabinet causes a significant bending of the original air curtain (Figs. 4.60-4.65). Then, for a given secondary air curtain with V_{2j} of 0.1 m/s and b_{2j} = 0.1m, the degree of the original air curtain bending still largely depends on the magnitude of the velocity of the original air jet, as evident from the results in Figs. 4.66-4.68 for b_j =0.024m. But when the velocity of the secondary air curtain is raised to 0.4 m/s and 0.7 m/s, the velocity of the original air curtain exhibits relatively slight effects on the bending of the original air curtain (Figs. 4.69-4.74) except at low $V_{j.}$ Similar trend is noted for a smaller width of the original air curtain from the results given in Figs. 4.75-4.83 for b_j =0.02m and in Figs. 4.84-4.92 for b_j =0.016m.

Table 4.1 Variations of Richardson numbers with the jet Reynolds number.

	Air discharge width = 0.024 m		Air discharge width = 0.02 m		Air discharge width = 0.016m	
Re_b	Ri_m	Ri_t	Ri_m	Ri_t	Ri_m	Ri_t
717.8	5.78E-03	9.10E-02	3.35E-03	5.27E-02	1.71E-03	2.70E-02
646	7.14E-03	1.12E-01	4.13E-03	6.50E-02	2.11E-03	3.33E-02
574.2	9.03E-03	1.42E-01	5.23E-03	8.23E-02	2.68E-03	4.21E-02
430.7	1.61E-01	2.53E-01	9.30E-03	1.46E-01	4.76E-03	7.49E-02
215.3	6.43E-02	1.02E+00	3.72E-02	5.85E-01	1.90E-02	3.00E-01
100.5	2.95E-01	4.64E+00	1.71E-01	2.69E+00	8.74E-02	1.38E+00

Table 4.2 Entrainment factors for selected cases with a single air curtain design

Air discharge width = 0.02 m		Air discharge width = 0.02 m with γ= 15°	
Reynolds Number Re_b	Entrainment Factor α	Reynolds number Re_b	Entrainment Factor α
717.8	0.01138	717.8	0.01082
646	0.0098	646	0.01516
574.2	0.00835	574.2	0.01082
430.7	0.00578	430.7	0.00733
215.3	0.00767	215.3	0.00688
100.5	0.00702	100.5	0.00899
Air discharge width = 0.016 m		Air discharge width = 0.016 m with γ= 15°	
Reynolds Number Re_b	Entrainment Factor α	Reynolds Number Re_b	Entrainment Factor α
717.8	0.01125	717.8	0.0107
646	0.01347	646	0.01278
574.2	0.00963	574.2	0.00918
430.7	0.00515	430.7	0.00412
215.3	0.00764	215.3	0.00731
100.5	0.00308	100.5	0.00296

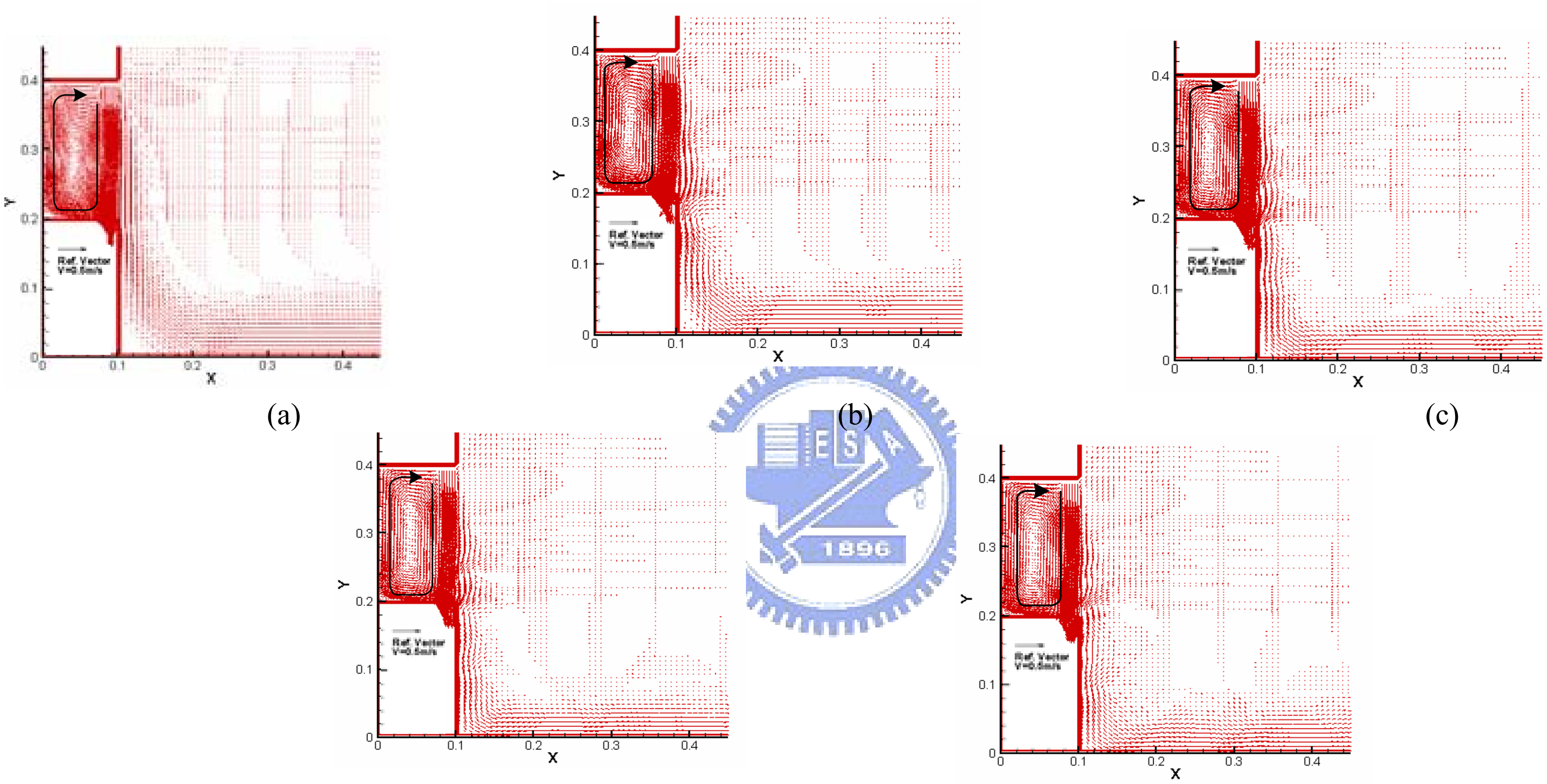

(a) (b) (c)

(d) (e)

Fig. 4.1 Velocity vector maps for steady cavity flow for $b_j = 0.02m, Gr_t = 0\ (\Delta T = 0^0 C)$ and N=0 for $\mathrm{Re}_b =$ (a) 100.5 (V_j = 0.07 m/s), (b) 215.3 (V_j = 0.15 m/s), (c) 430.7 (V_j = 0.3 m/s), (d) 574.2 (V_j = 0.4 m/s), and (e) 646 (V_j = 0.45 m/s).

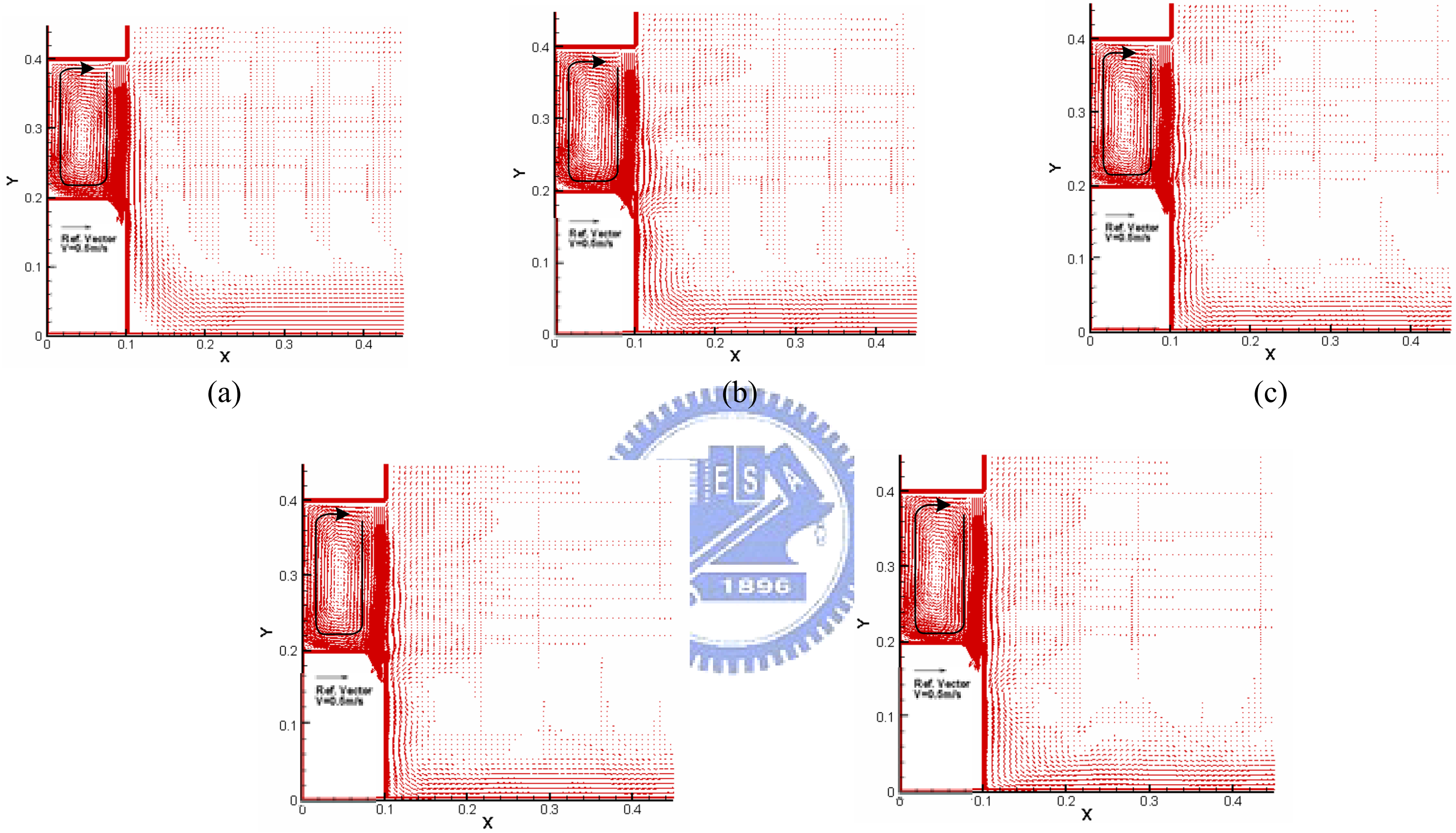

(a) (b) (c)

(d) (e)

Fig. 4.2 Velocity vector maps for steady cavity flow for $b_j = 0.016m, Gr_t = 0$ ($\Delta T = 0^0 C$) and N=0 for $\mathrm{Re}_b =$ (a) 100.5 (V_j = 0.0875 m/s), (b) 215.3 (V_j = 0.187 m/s), (c) 430.7 (V_j = 0.375m/s), (d) 574.2 (V_j = 0.5 m/s), (e) and 646 (V_j = 0.56 m/s).

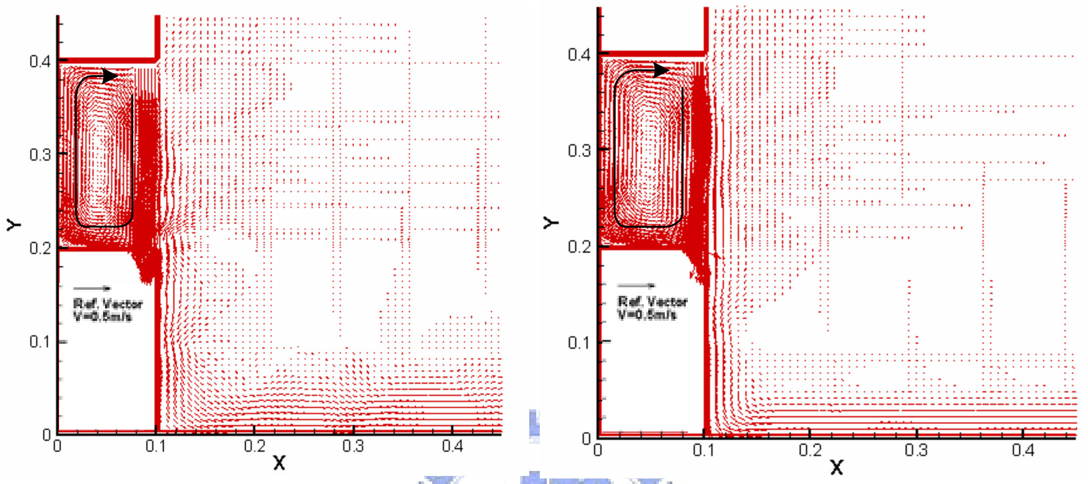

(a) (b)

Fig. 4.3 Velocity vector maps for steady cavity flow for $\mathrm{Re}_b = 646$, $Gr_t = 0\,(\Delta T = 0^0 C)$ and N=0 for (a) $b_j = 0.02m$ and (b) $b_j = 0.01m$.

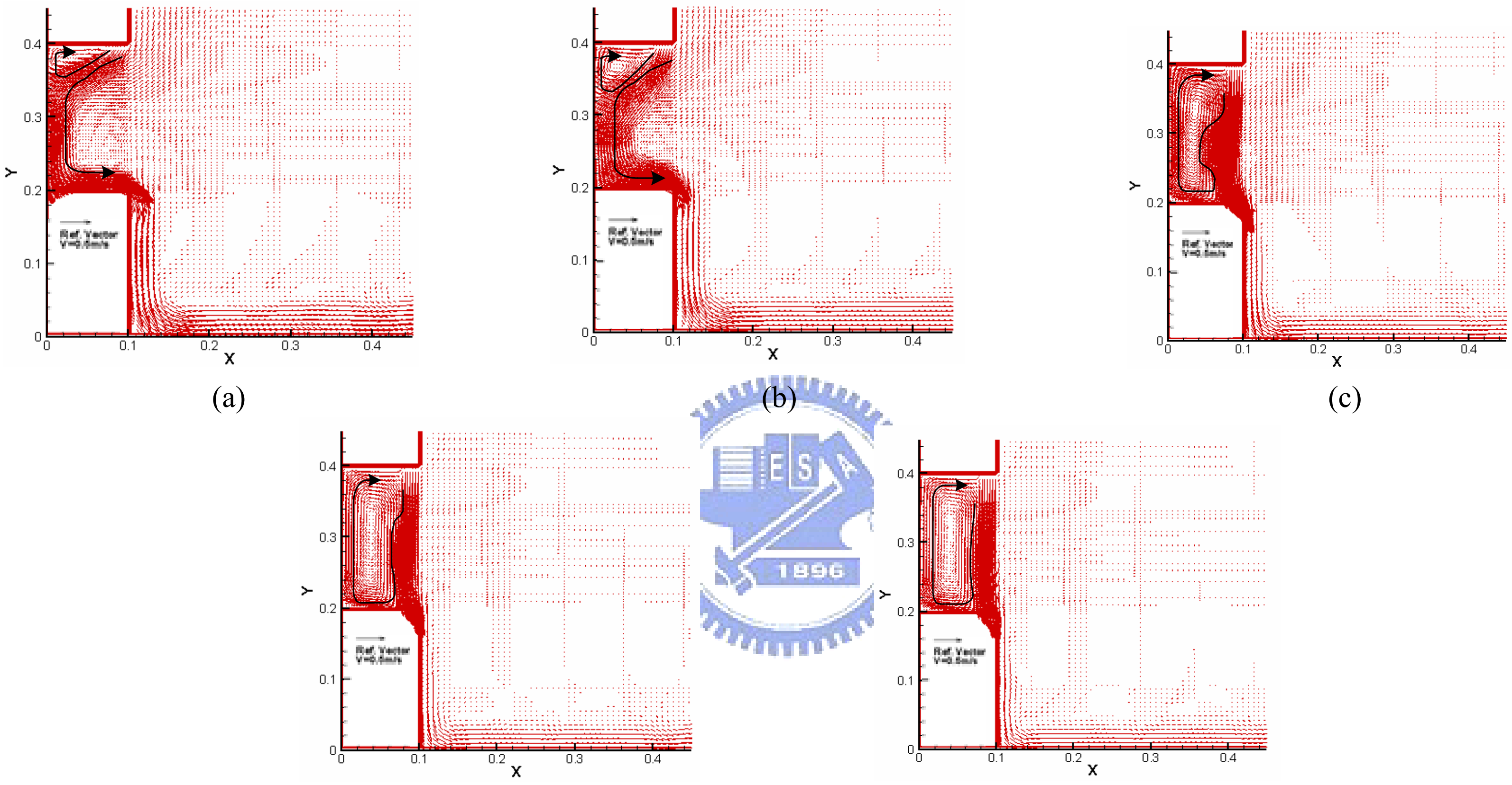

(a) (b) (c)

(d) (e)

Fig. 4.4 Velocity vector maps for steady cavity flow for $b_j = 0.02m$, $Gr_t = 6.78 \times 10^6$ $(\Delta T = 5^0 C)$ and N=0 for $\mathrm{Re}_b =$ (a) 100.5 (V_j = 0.07 m/s), (b)215.3 (V_j = 0.15 m/s), (c) 430.7 (V_j = 0.3 m/s), (d) 574.2 (V_j = 0.4 m/s), and (e) 646 (V_j = 0.45m/s)

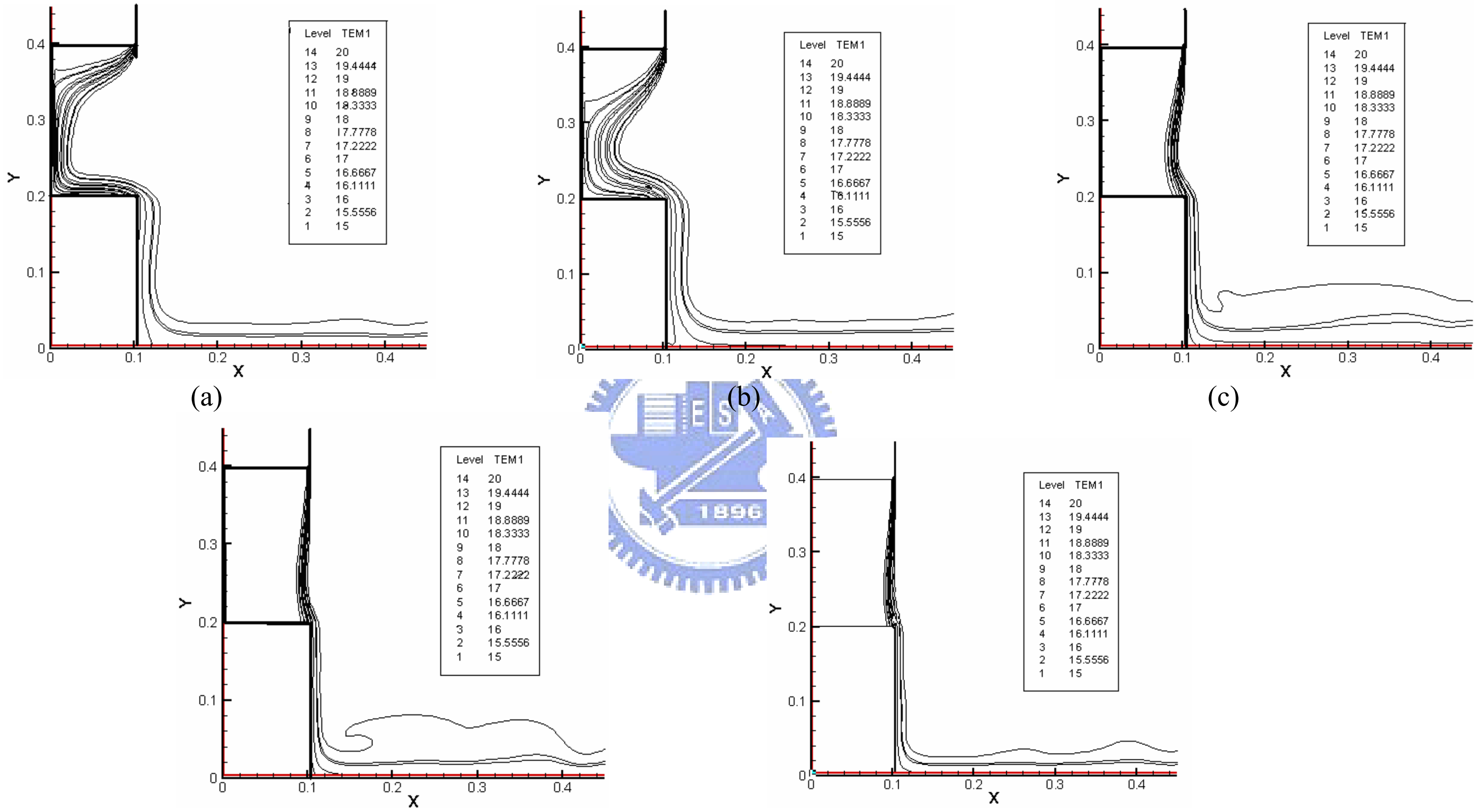

(a) (b) (c)

(d) (e)

Fig. 4.5 Isotherms in the cavity for steady cavity flow for $b_j = 0.02m, Gr_t = 6.78\times10^6$ $(\Delta T = 5^0 C)$ and N=0 for $\mathrm{Re}_b =$ (a) 100.5 (V_j = 0.07 m/s), (b) 215.3 (V_j = 0.15 m/s), (c) 430.7 (V_j = 0.3 m/s), (d) 574.2 (V_j = 0.4 m/s), and (e) 646 (V_j = 0.45 m/s).

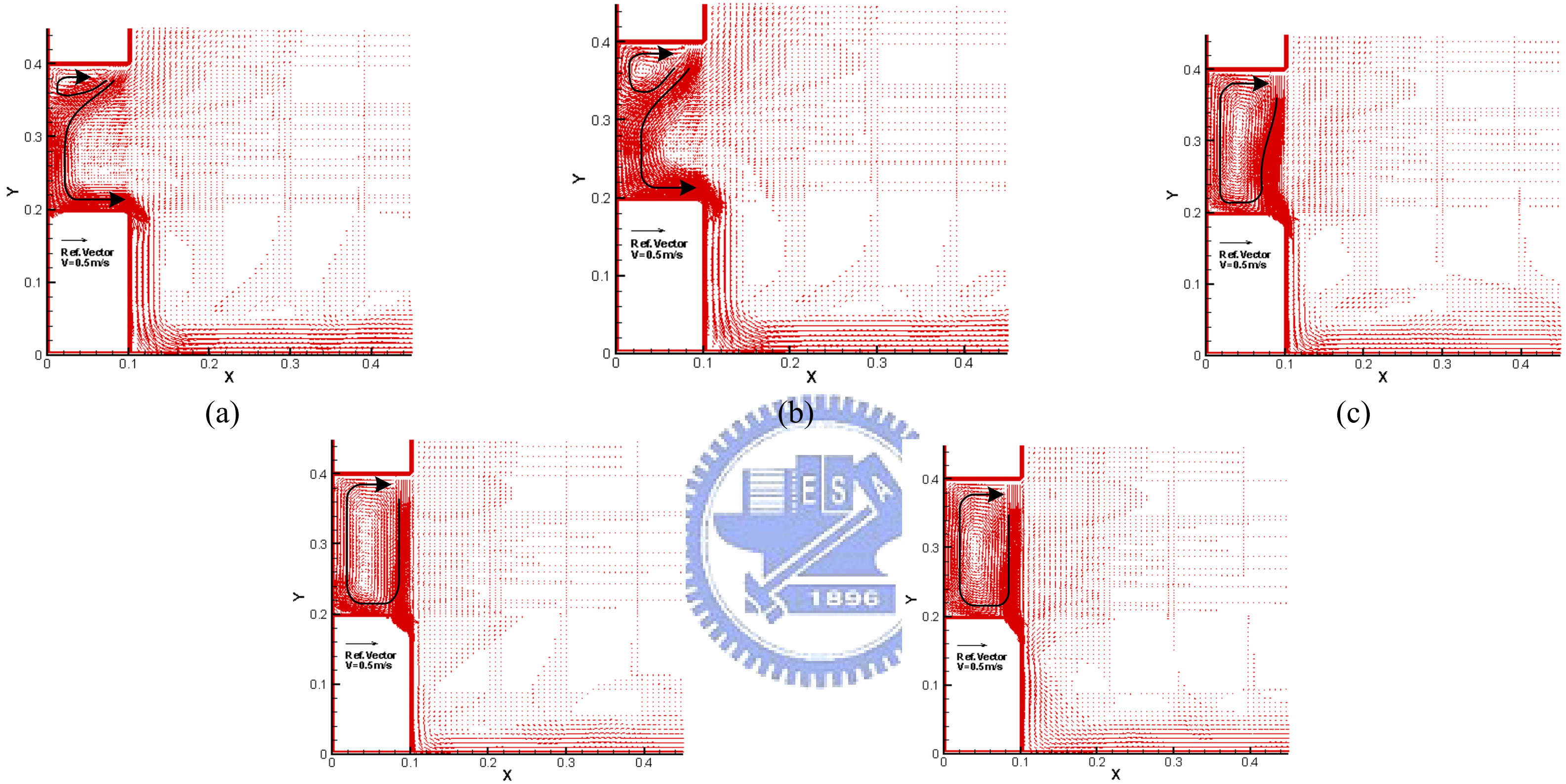

(a) (b) (c)

(d) (e)

Fig. 4.6 Velocity vector maps for steady cavity flow for $b_j = 0.016m, Gr_t = 6.78\times10^6$ $(\Delta T = 5^0 C)$ and N=0 for $\text{Re}_b =$ (a) 100.5 (V_j = 0.0875 m/s), (b) 215.3 (V_j = 0.187 m/s), (c) 430.7 (V_j = 0.375m/s), (d) 574.2 (V_j = 0.5m/s), and (e) 646 (V_j = 0.56m/s).

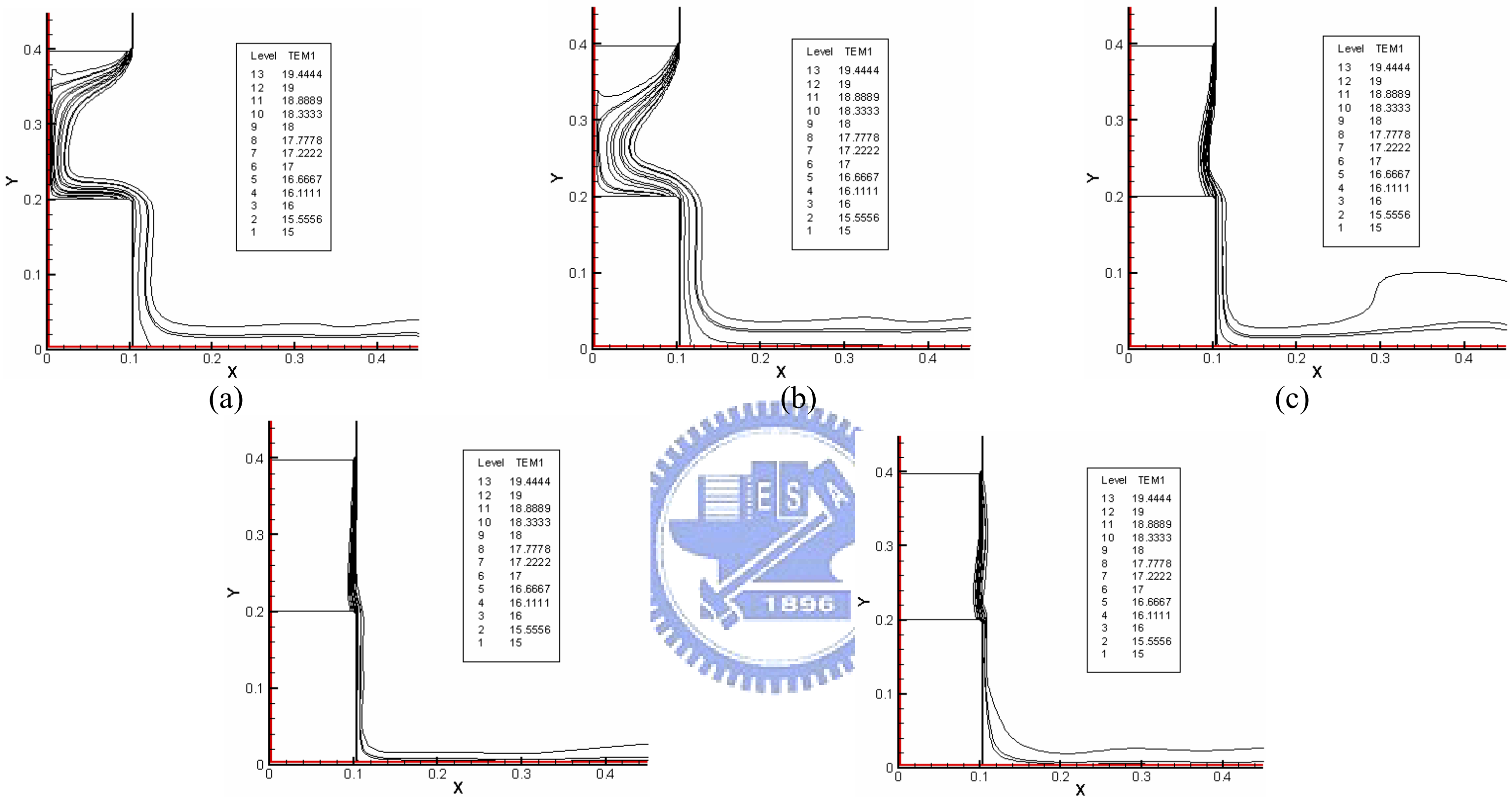

(a) (b) (c)

(d) (e)

Fig. 4.7 Isotherms in the cavity for steady cavity flow for $b_j = 0.016m$, $Gr_t = 6.78\times10^6$ ($\Delta T = 5^0 C$) and N=0 for $\mathrm{Re}_b =$ (a) 100.5 (V_j = 0.0875 m/s), (b) 215.3 (V_j = 0.187 m/s), (c) 430.7 (V_j = 0.375m/s), (d) 574.2 (V_j = 0.5m/s), and (e) 646 (V_j = 0.56 m/s)

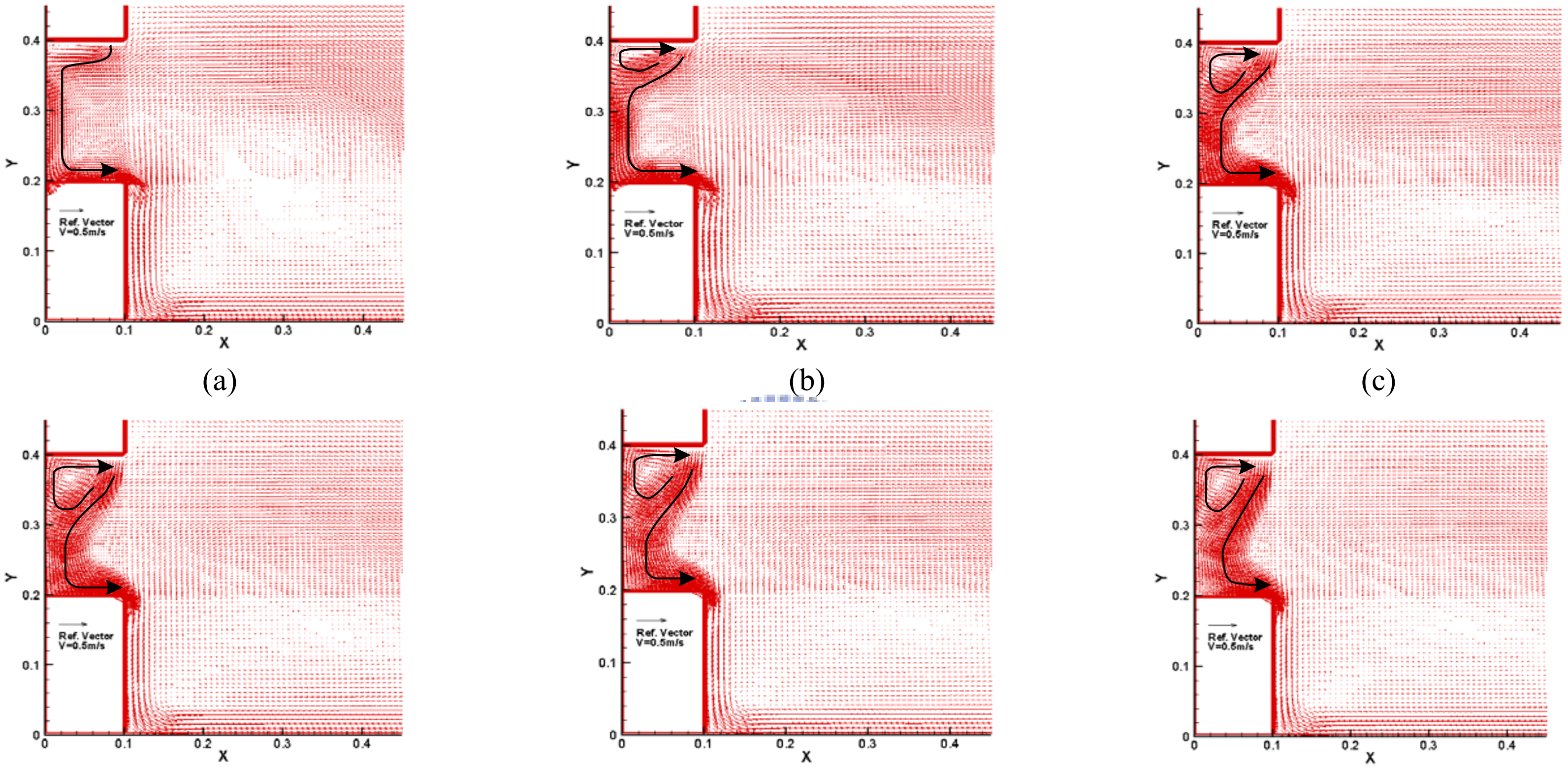

(a) (b) (c)

(d) (e) (f)

Fig. 4.8 Velocity vector maps for steady cavity flow for $b_j = 0.024m, Gr_t = 2.7\times10^7$ $(\Delta T = 20^0 C)$ and N=$6.35\cdot10^{-2}$ for $\mathrm{Re}_b =$ (a) 100.5 (V_j= 0.0583 m/s), (b) 215.3 (V_j= 0.125 m/s), (c) 430.7 (V_j= 0.25m/s), (d) 574.2 (V_j= 0.33m/s), (e) 646 (V_j= 0.375m/s), and (f) 717.8 (V_j= 0.416 m/s)

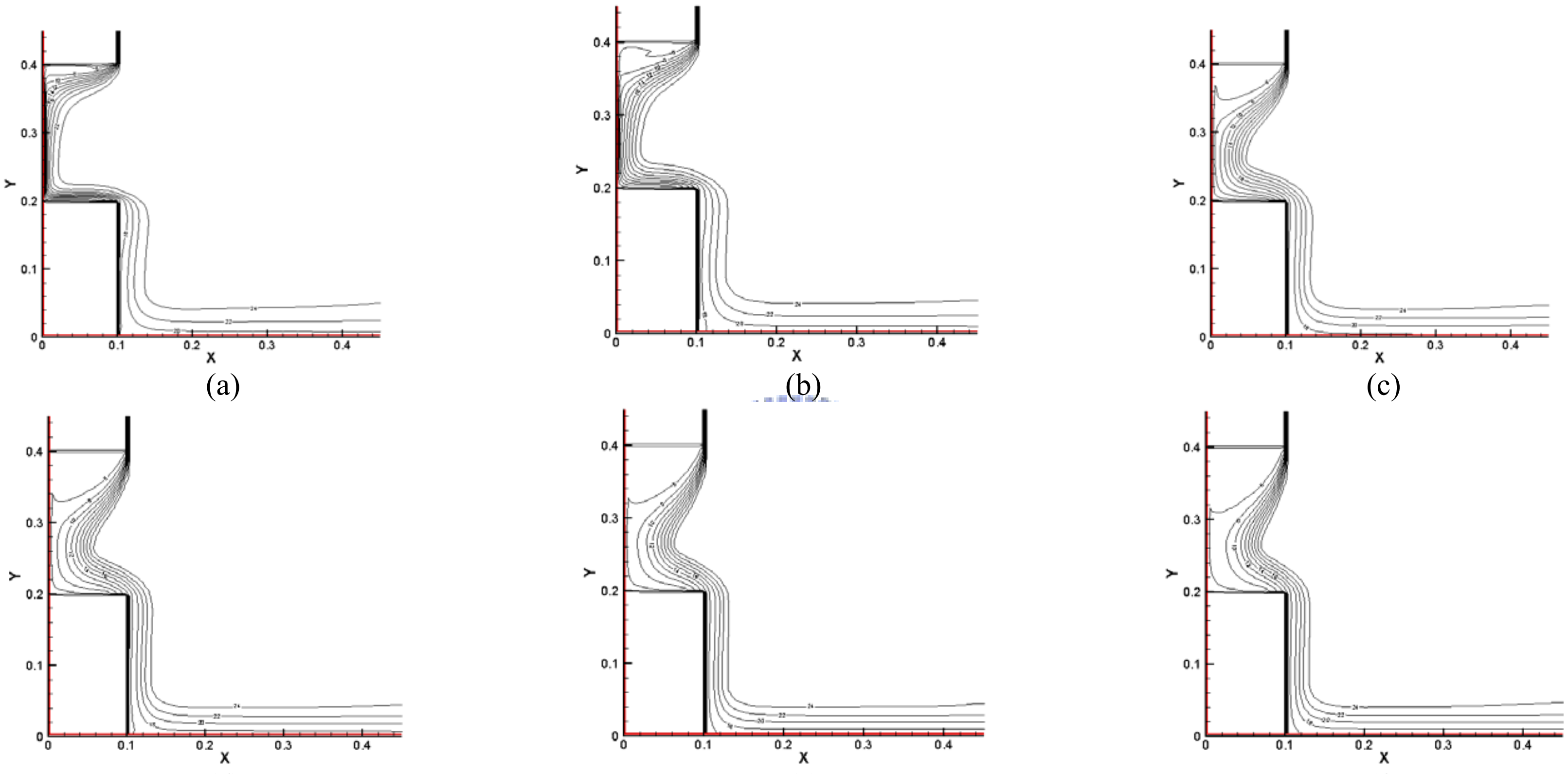

(a) (b) (c)

(d) (e) (f)

Fig. 4.9 Isotherms in the cavity for steady cavity flow for $b_j = 0.024m$, $Gr_t = 2.7\times10^7$ ($\Delta T = 20^0 C$) and N= $6.35\cdot10^{-2}$ for $\mathrm{Re}_b =$ (a) 100.5 (V_j = 0.0583 m/s), (b) 215.3 (V_j = 0.125 m/s), (c) 430.7 (V_j = 0.25m/s), (d) 574.2 (V_j = 0.33m/s), (e) 646 (V_j = 0.375m/s), and (f) 717.8 (V_j = 0.416 m/s)

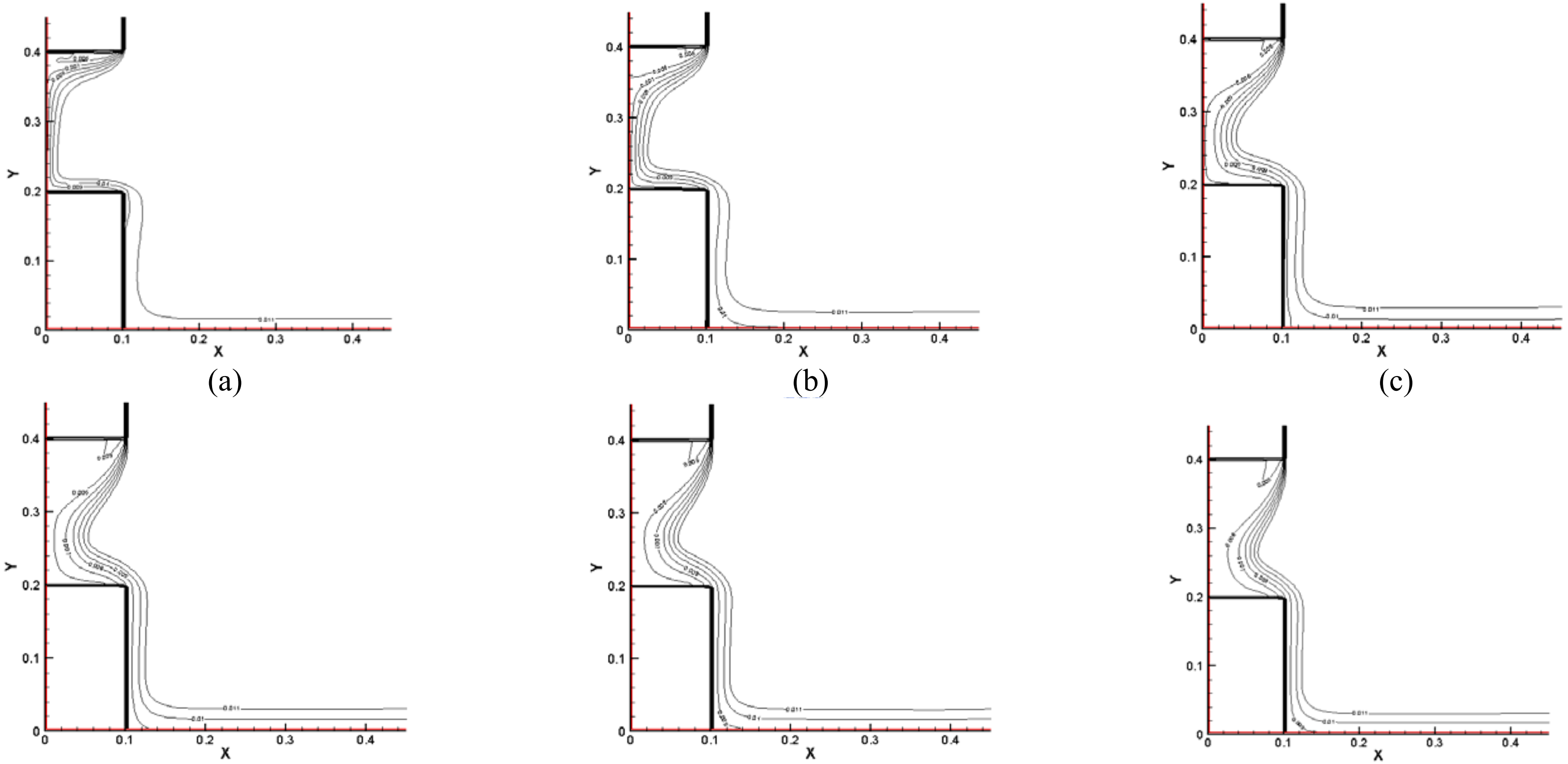

(a) (b) (c)

(d) (e) (f)

Fig. 4.10 Iso-concentration lines for steady cavity flow for $b_j = 0.024m$, $Gr_t = 2.7\times10^7$ $(\Delta T = 20^0 C)$ and N= $6.35\cdot10^{-2}$ for $\mathrm{Re}_b =$ (a) 100.5 (V_j = 0.0583 m/s), (b) 215.3 (V_j = 0.125 m/s), (c) 430.7 (V_j = 0.25m/s), (d) 574.2 (V_j = 0.33m/s), (e) 646 (V_j = 0.375m/s), and (f) 717.8 (V_j = 0.416 m/s)

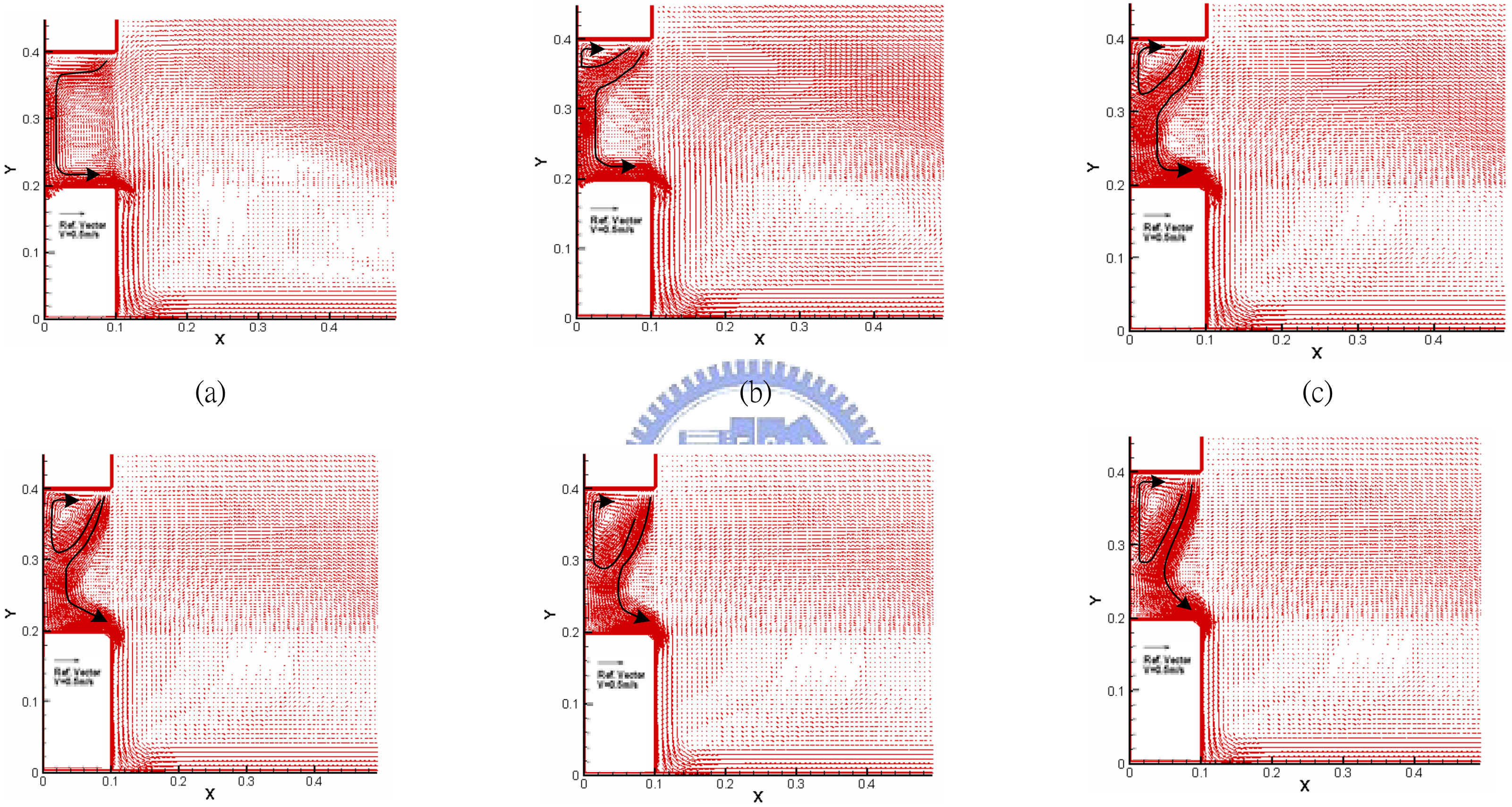

(a)

(b)

(c)

(d)

(e)

(f)

Fig. 4.11 Velocity vector maps for steady cavity flow for $b_j = 0.02m, Gr_t = 2.7\times10^7$ $(\Delta T = 20^0 C)$ and N=$6.35\cdot10^{-2}$ for Re_b = (a) 100.5 (V_j = 0.07 m/s), (b) 215.3 (V_j = 0.15 m/s), (c) 430.7 (V_j = 0.3m/s), (d) 574.2 (V_j = 0.4m/s), (e) 646 (V_j = 0.45m/s), and (f) 717.8 (V_j = 0.5 m/s)

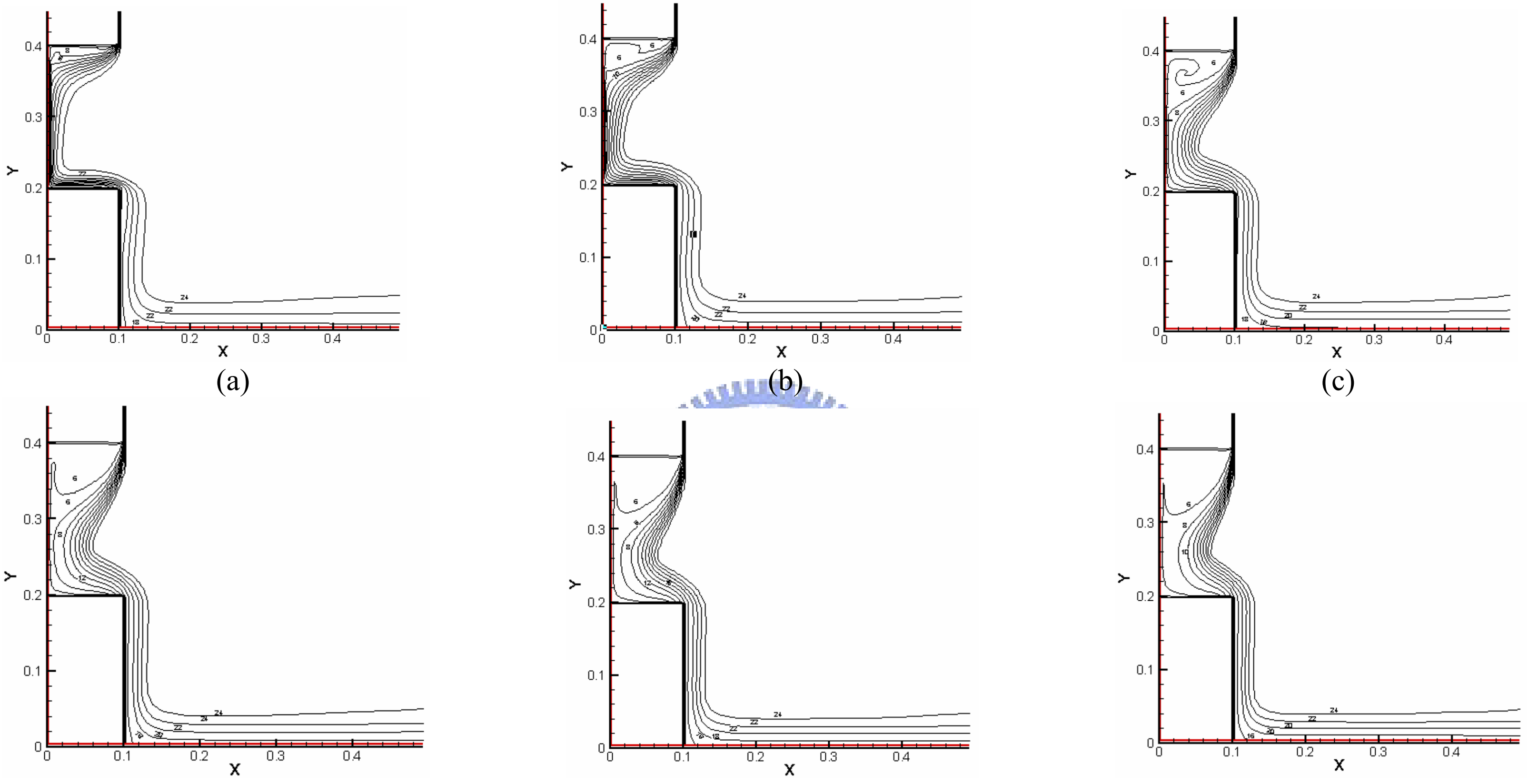

(a) (b) (c)

(d) (e) (f)

Fig. 4.12 Isotherms in the cavity for steady cavity flow for $b_j = 0.02m, Gr_t = 2.7\times10^7$ $(\Delta T = 20^0 C)$ and N=$6.35\cdot10^{-2}$ for Re_b = (a) 100.5 (V_j= 0.07 m/s), (b) 215.3 (V_j= 0.15 m/s), (c) 430.7 (V_j= 0.3m/s), (d) 574.2 (V_j= 0.4m/s), (e) 646 (V_j= 0.45m/s), and (f) 717.8 (V_j= 0.5 m/s)

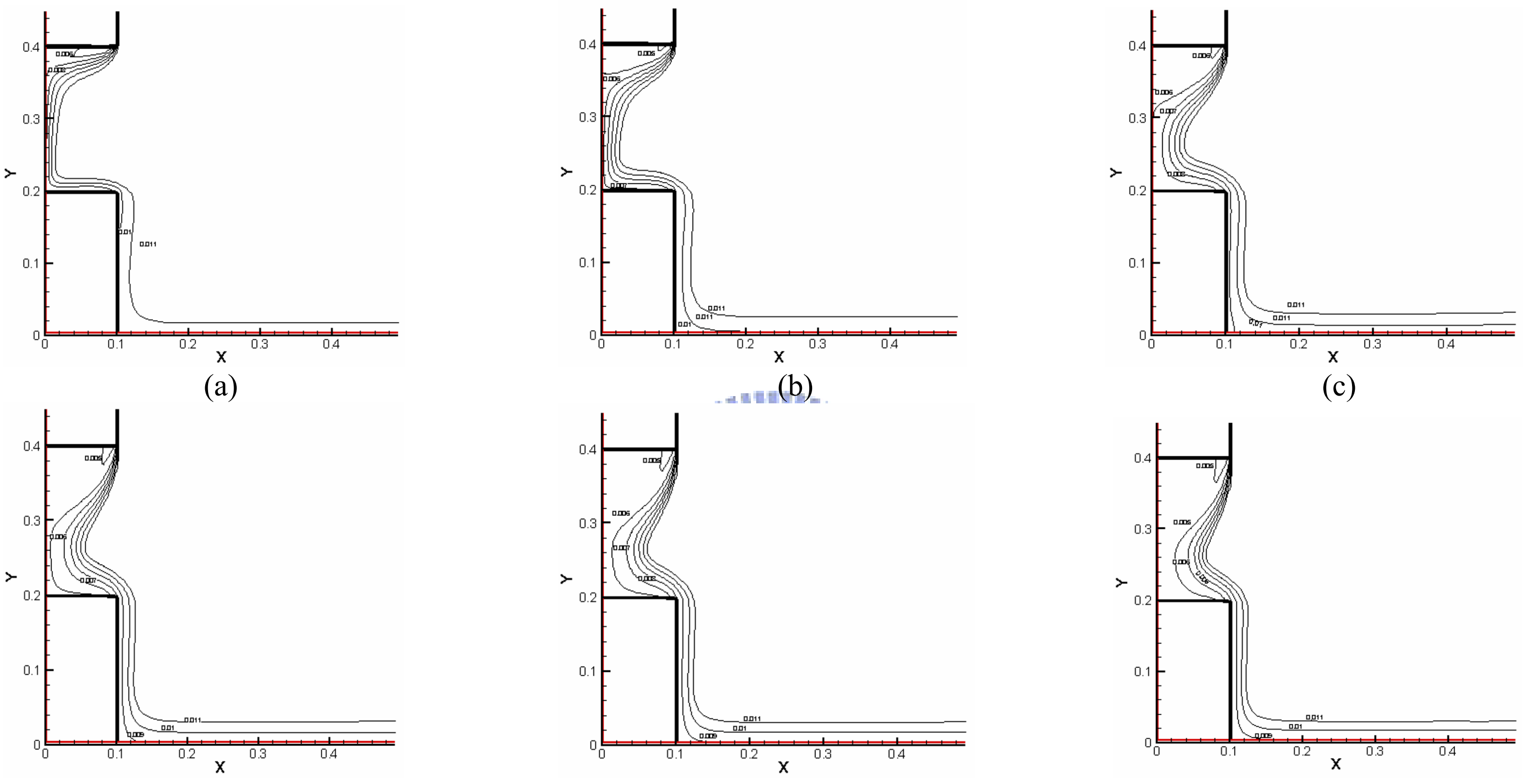

Fig. 4.13 Iso-concentration lines for steady cavity flow for $b_j = 0.02m, Gr_t = 2.7\times10^7$ $(\Delta T = 20^0 C)$ and N=$6.35\cdot10^{-2}$ for $\mathrm{Re}_b =$ (a) 100.5 (V_j= 0.07 m/s), (b) 215.3 (V_j= 0.15 m/s), (c) 430.7 (V_j= 0.3m/s), (d) 574.2 (V_j= 0.4m/s), (e) 646 (V_j= 0.5 m/s) , and (f) 717.8 (V_j= 0.5 m/s)

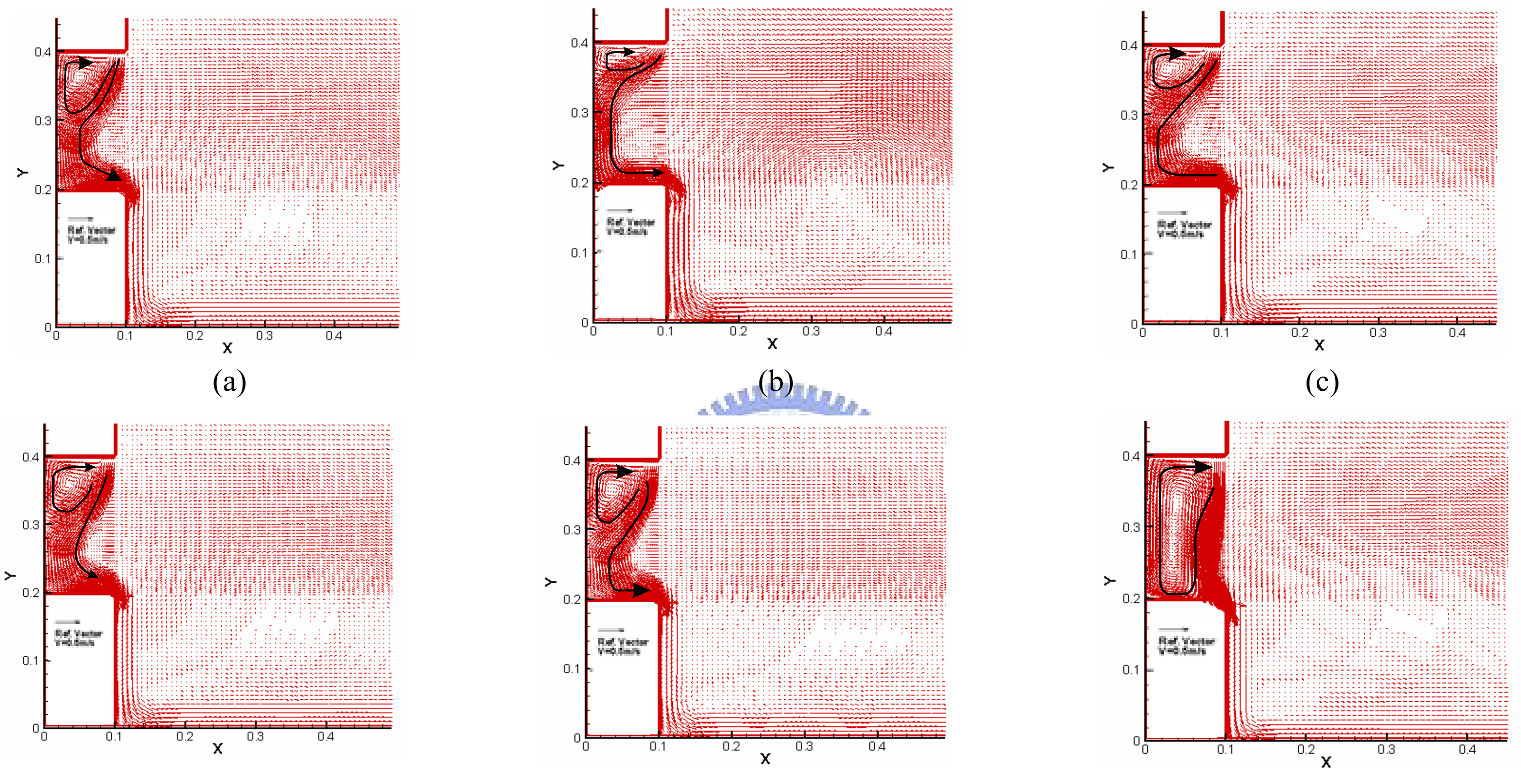

(a) (b) (c)

(d) (e) (f)

Fig. 4.14 Velocity vector maps for steady cavity flow for $b_j = 0.016m$, $Gr_t = 2.7\times10^7$ $(\Delta T = 20^0C)$ and N=$6.35\cdot10^{-2}$ for $\mathrm{Re}_b =$ (a) 100.5 (V_j= 0.0875 m/s), (b) 215.3 (V_j= 0.187 m/s), (c) 430.7 (V_j= 0.375m/s), (d) 574.2 (V_j= 0.5m/s), (e) 646 (V_j= 0.56m/s), and (f) 717.8 (V_j= 0.62 m/s)

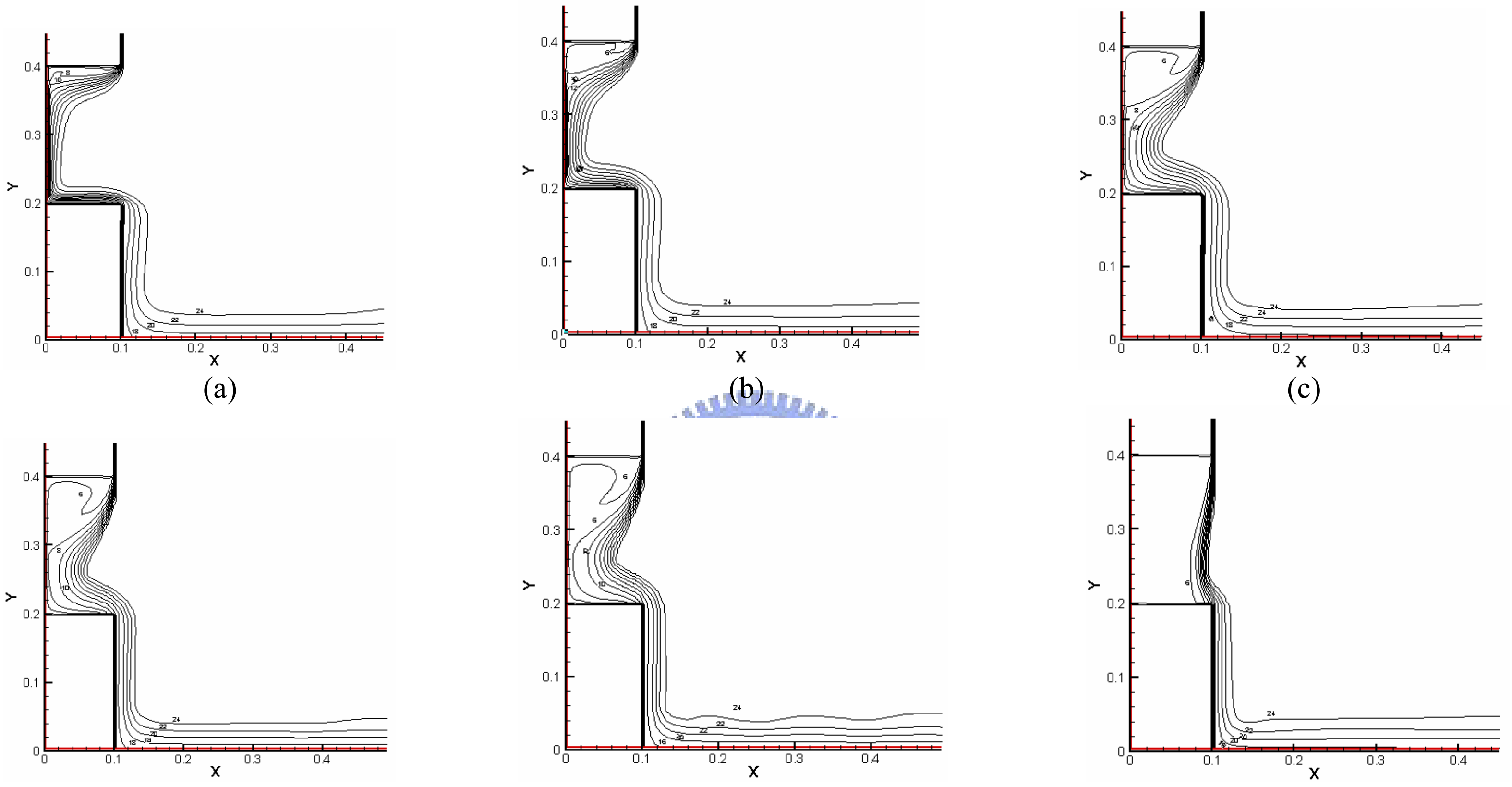

(a) (b) (c)

(d) (e) (f)

Fig. 4.15 Isotherms in the cavity for steady cavity flow for $b_j = 0.016m, Gr_t = 2.7\times10^7$ $(\Delta T = 20^0 C)$ and N= $6.35\cdot10^{-2}$ for $\mathrm{Re}_b =$ (a) 100.5 (V_j = 0.0875 m/s), (b) 215.3 (V_j = 0.187 m/s), (c) 430.7 (V_j = 0.375m/s), (d) 574.2 (V_j = 0.5m/s), (e) 646 (V_j = 0.56m/s), and (f) 717.8 (V_j = 0.62 m/s)

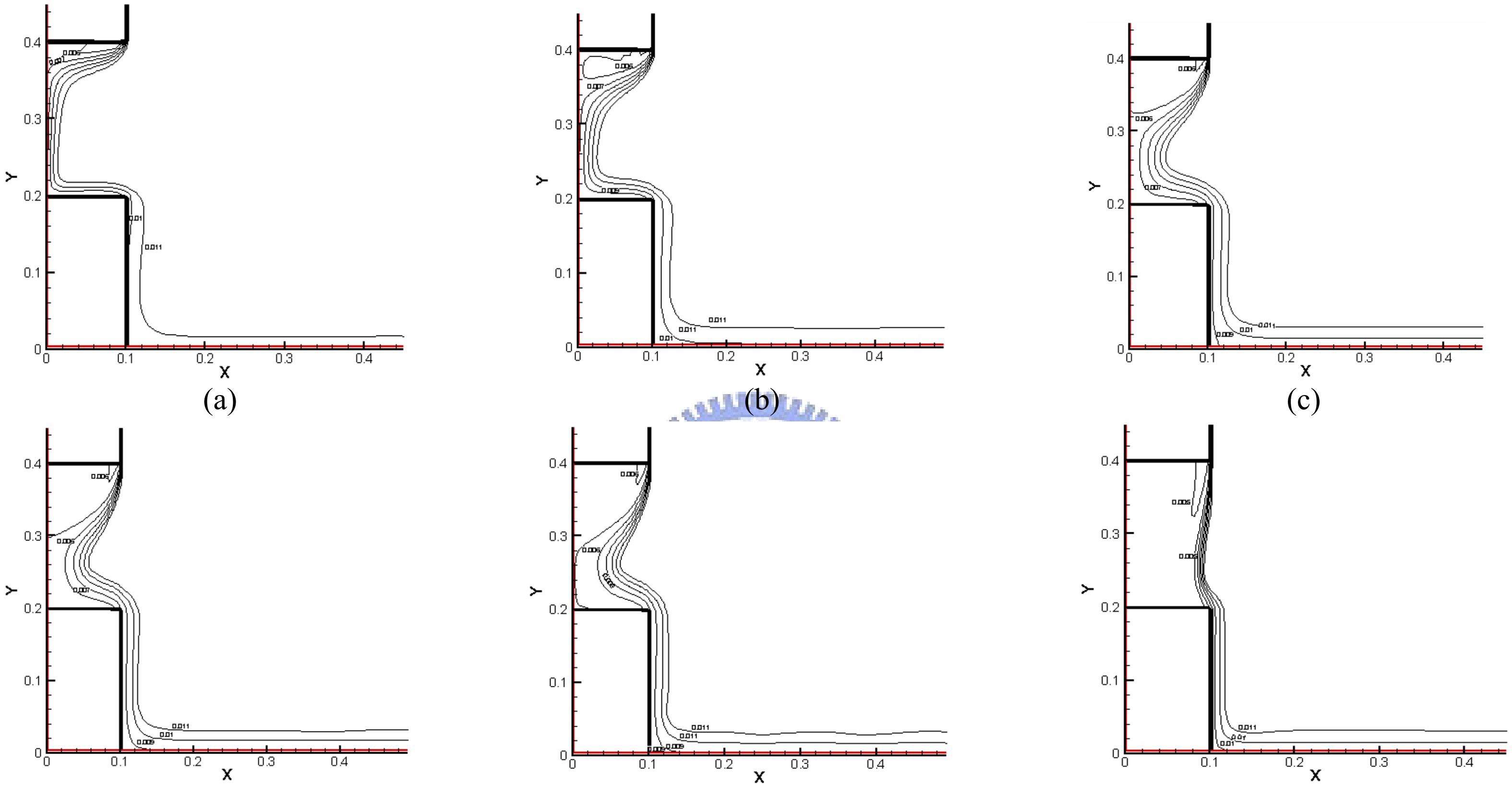

(a) (b) (c)

(d) (e) (f)

Fig. 4.16 Iso-concentration lines for steady cavity flow for $b_j = 0.016m, Gr_t = 2.7 \times 10^7$ $(\Delta T = 20^0 C)$ and N= $6.35 \cdot 10^{-2}$ for $\mathrm{Re}_b =$ (a) 100.5 (V_j = 0.0875 m/s), (b) 215.3 (V_j = 0.187 m/s), (c) 430.7 (V_j = 0.375m/s), (d) 574.2 (V_j = 0.5m/s), (e) 646 (V_j = 0.56m/s), and (f) 717.8 (V_j = 0.62 m/s)

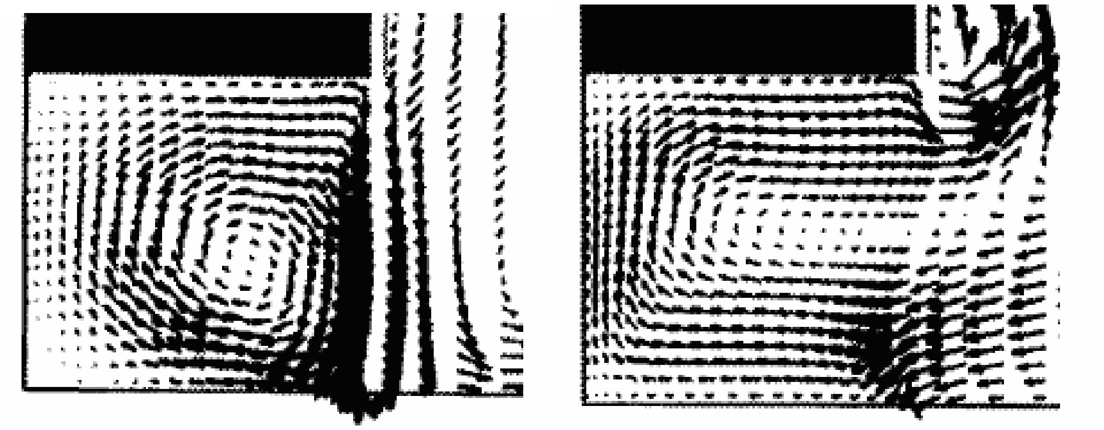

(a) (b)

Fig. 4.17 Steady cartography of speeds in the cavity and in the medium surrounding from Mhiri et al. [22] for $b_j / H = 1/20, Gr_b = 10000$ and N=0 for (a) Ri=0.04 and (b) Ri=1.

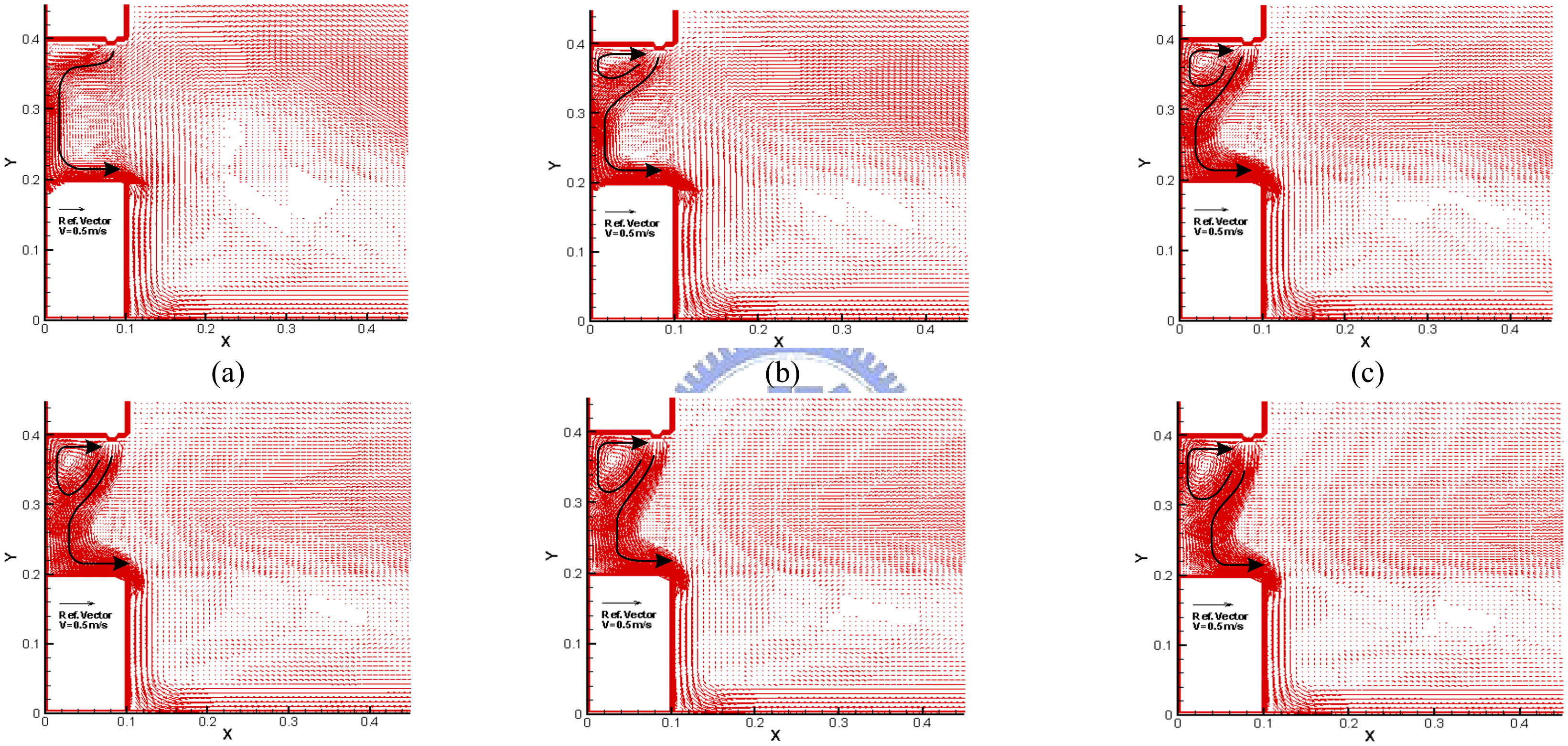

(a) (b) (c)

(d) (e) (f)

Fig. 4.18 Velocity vector maps for $b_j = 0.024m, Gr_t = 2.7\times10^7$ and N=$6.35\cdot10^{-2}$ with a jet inclined angle of 15° for Re_b = (a) 100.5 (V_j = 0.0583 m/s), (b) 215.3 (V_j = 0.125 m/s), (c) 430.7 (V_j = 0.25m/s), (d) 574.2 (V_j = 0.333m/s), (e) 646 (V_j = 0.375m/s), and (f) 717.8(V_j = 0.4162 m/s)

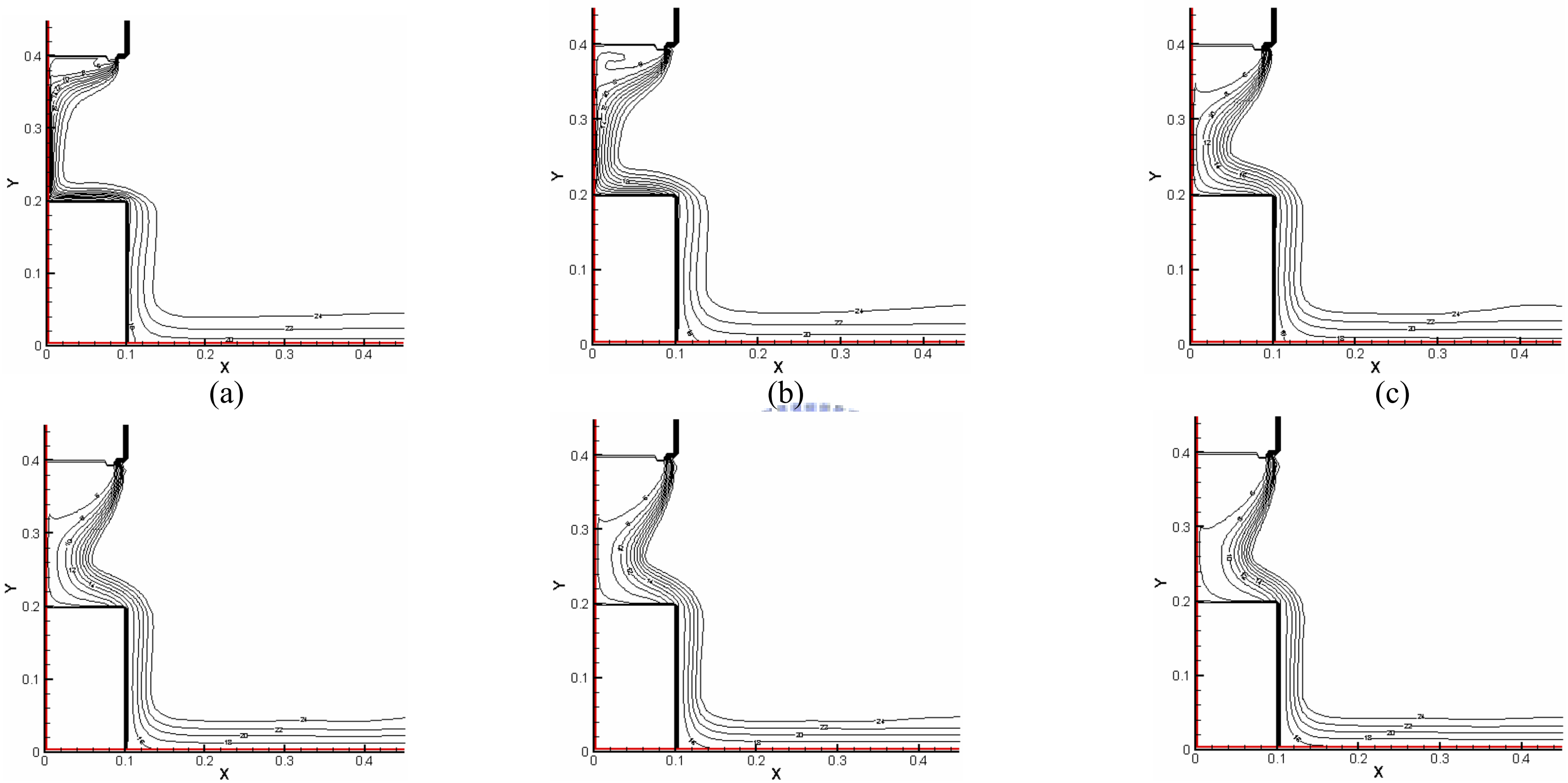

(a) (b) (c)

(d) (e) (f)

Fig. 4.19 Isotherms in the cavity for $b_j = 0.024m, Gr_t = 2.7\times10^7$ and N=$6.35\cdot10^{-2}$ with a jet inclined angle of 15° for $\mathrm{Re}_b =$ (a) 100.5 (V_j= 0.0583 m/s), (b) 215.3 (V_j= 0.125 m/s), (c) 430.7 (V_j= 0.25m/s), (d) 574.2 (V_j= 0.333m/s), (e) 646 (V_j= 0.375m/s), and (f) 717.8 (V_j= 0.4162 m/s)

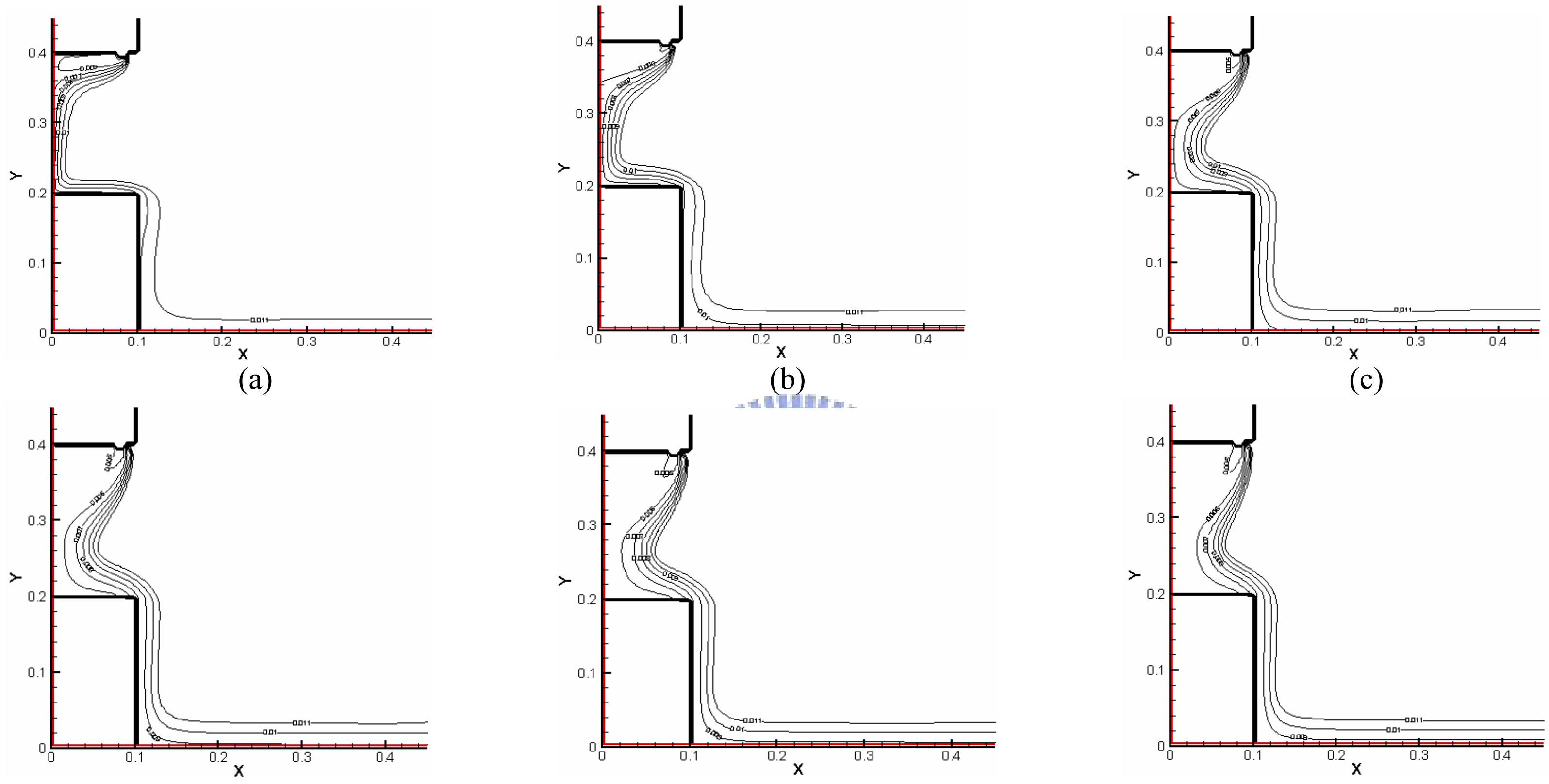

(a) (b) (c)

(d) (e) (f)

Fig. 4.20 Iso-concentration lines for $b_j = 0.024m, Gr_t = 2.7\times10^7$ $(\Delta T = 20^0 C)$ and N=$6.35\cdot10^{-2}$ with a jet inclined angle of 15° for $\mathrm{Re}_b =$ (a) 100.5 (V_j = 0.0583 m/s), (b) 215.3 (V_j = 0.125 m/s), (c) 430.7 (V_j = 0.25m/s), (d) 574.2 (V_j = 0.333m/s), (e) 646 (V_j = 0.375m/s), and (f) 717.8 (V_j = 0.4162m/s)

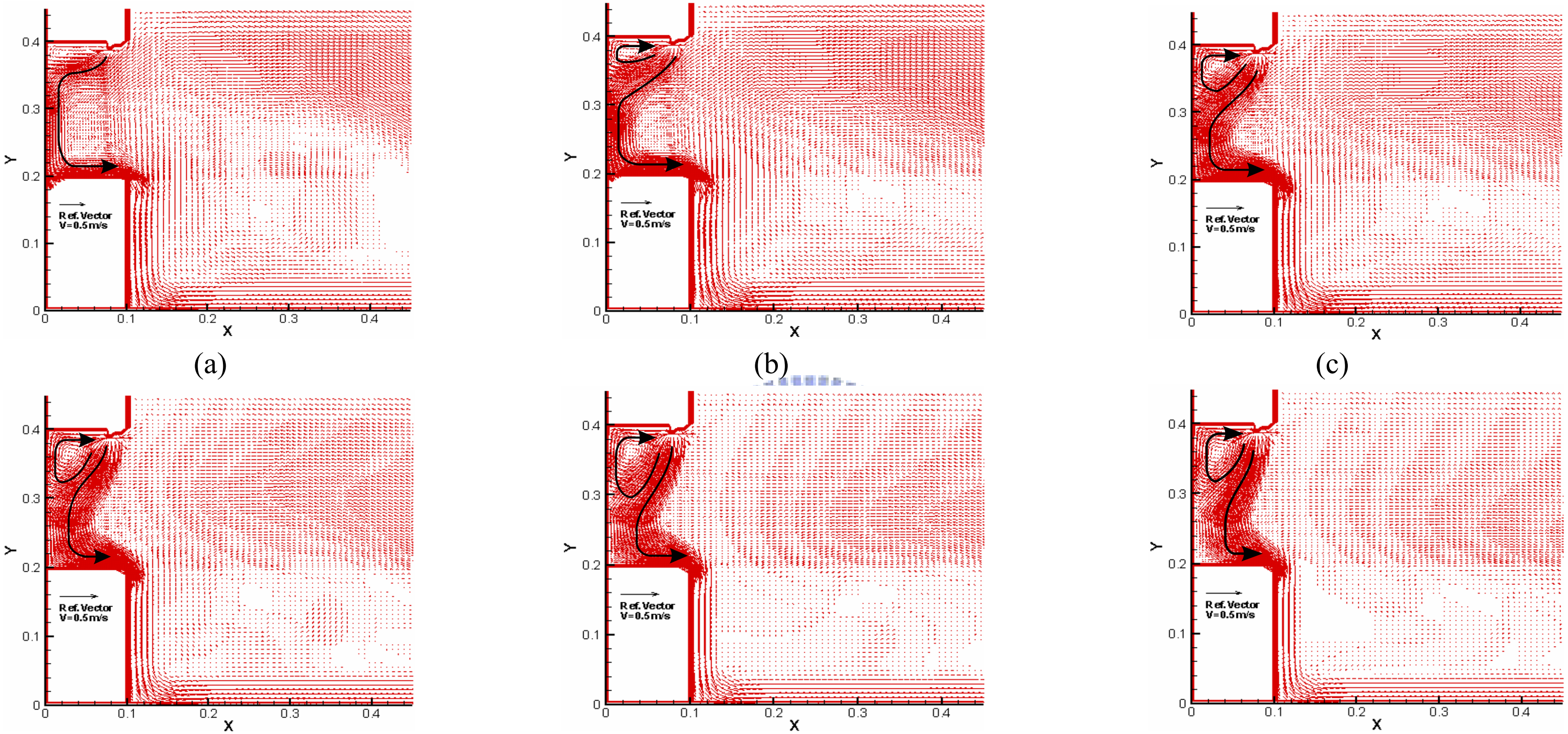

(a) (b) (c)

(d) (e) (f)

Fig. 4.21 Velocity vector maps for $b_j = 0.024m$, $Gr_t = 2.7 \times 10^7$ and N= $6.35 \cdot 10^{-2}$ with a jet inclined angle of 25° for $\mathrm{Re}_b =$ (a) 100.5 (V_j = 0.0583 m/s), (b) 215.3 (V_j = 0.125 m/s), (c) 430.7 (V_j = 0.25m/s), (d) 574.2 (V_j = 0.33m/s), (e) 646 (V_j = 0.375m/s), and (f) 717.8 (V_j = 0.416 m/s)

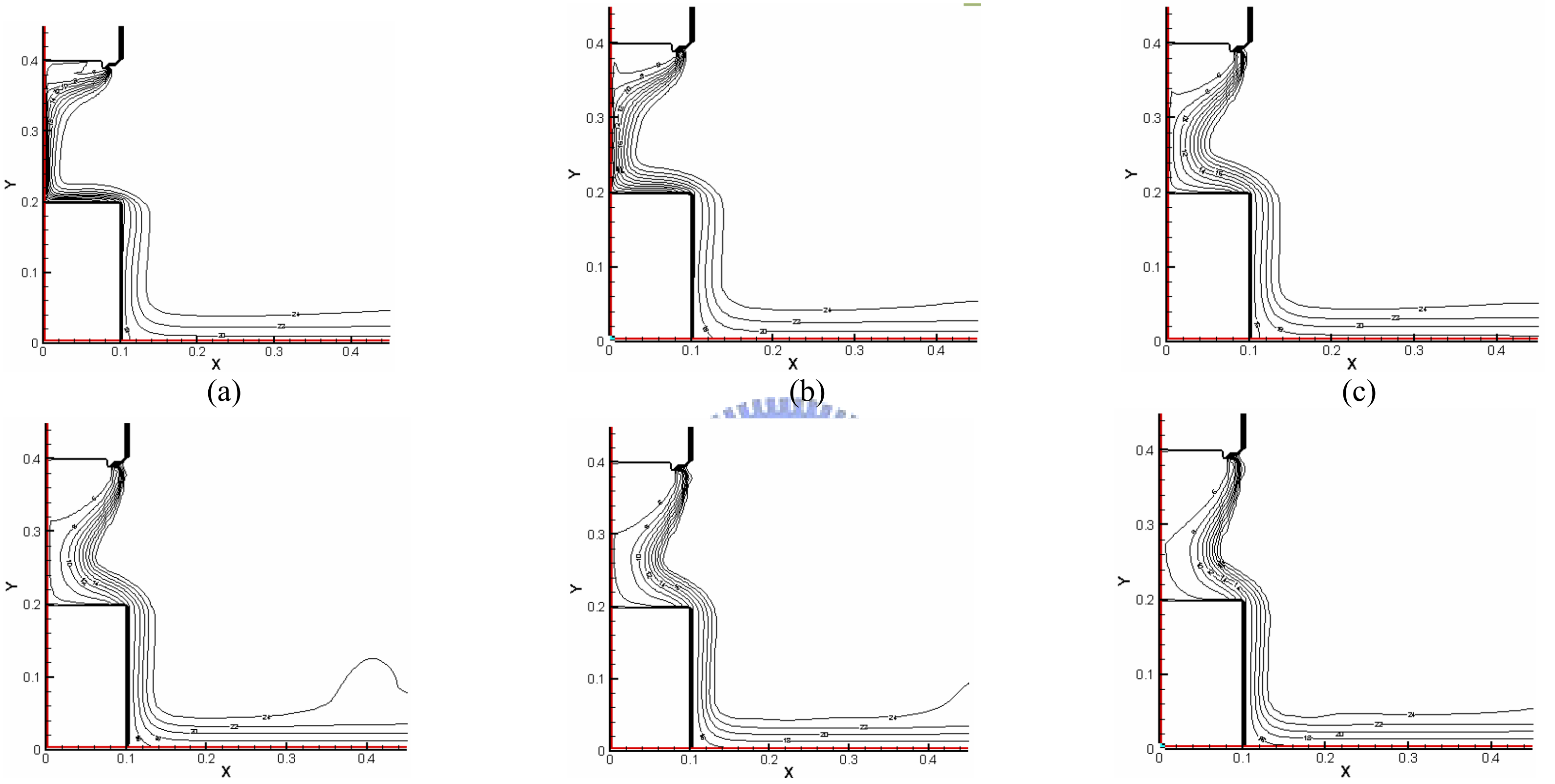

(a) (b) (c)

(d) (e) (f)

Fig. 4.22 Isotherms in the cavity for $b_j = 0.024m, Gr_t = 2.7\times10^7$ and N=$6.35\cdot10^{-2}$ with a jet inclined angle of 25° for Re_b = (a) 100.5 (V_j= 0.0583 m/s), (b) 215.3 (V_j= 0.125 m/s), (c) 430.7 (V_j= 0.25m/s), (d) 574.2 (V_j= 0.33m/s), (e) 646 (V_j= 0.375m/s) , and (f) 717.8(V_j= 0.416 m/s)

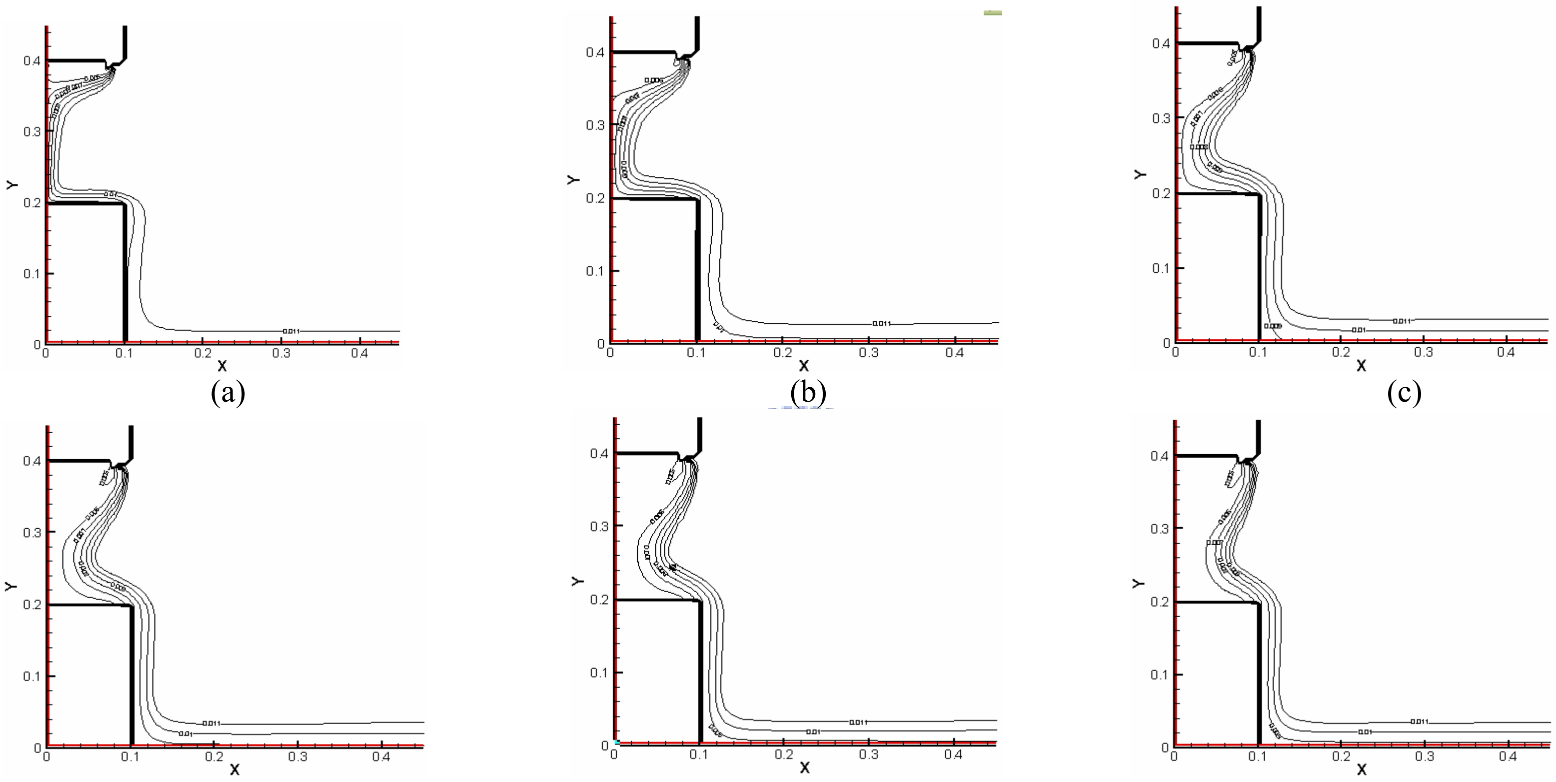

(a) (b) (c)

(d) (e) (f)

Fig. 4.23 Iso-concentration lines for $b_j = 0.024m, Gr_t = 2.7\times10^7$ and N= $6.35\cdot10^{-2}$ with a jet inclined angle of 25° for $\mathrm{Re}_b =$ (a) 100.5 (V_j = 0.0583 m/s), (b) 215.3 (V_j = 0.125 m/s), (c) 430.7 (V_j = 0.25m/s), (d) 574.2 (V_j = 0.33m/s), (e) 646 (V_j = 0.375m/s), and (f) 717.8 (V_j = 0.416 m/s)

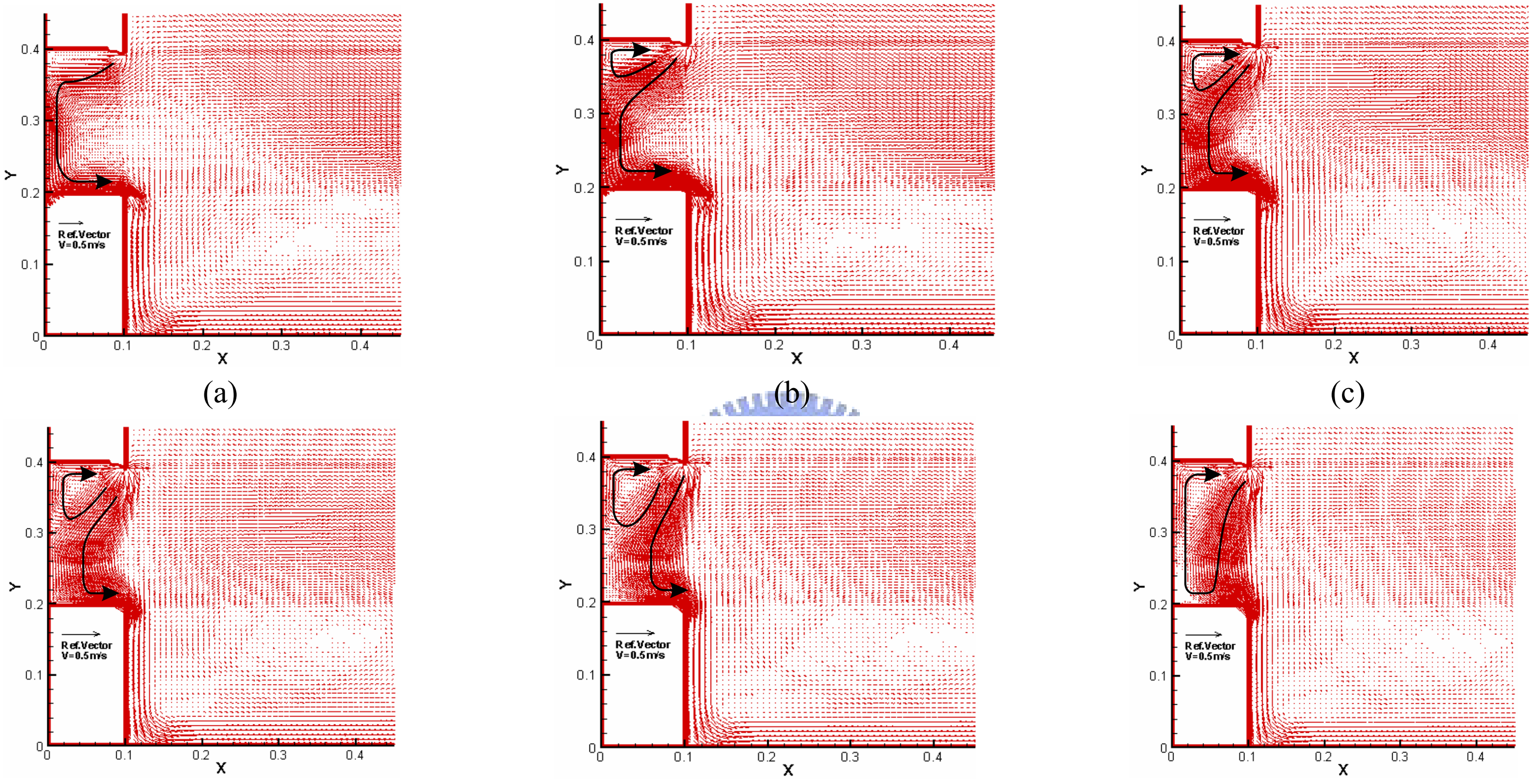

(a) (b) (c)

(d) (e) (f)

Fig. 4.24 Velocity vector maps for $b_j = 0.024m, Gr_t = 2.7\times10^7$ and N= $6.35\cdot10^{-2}$ with a jet inclined angle of -15° for Re_b = (a) 100.5 (V_j = 0.0583 m/s), (b) 215.3 (V_j = 0.125 m/s), (c) 430.7 (V_j = 0.25m/s), (d) 574.2 (V_j = 0.33m/s), (e) 646 (V_j = 0.375m/s), and (f) 717.8 (V_j = 0.416 m/s)

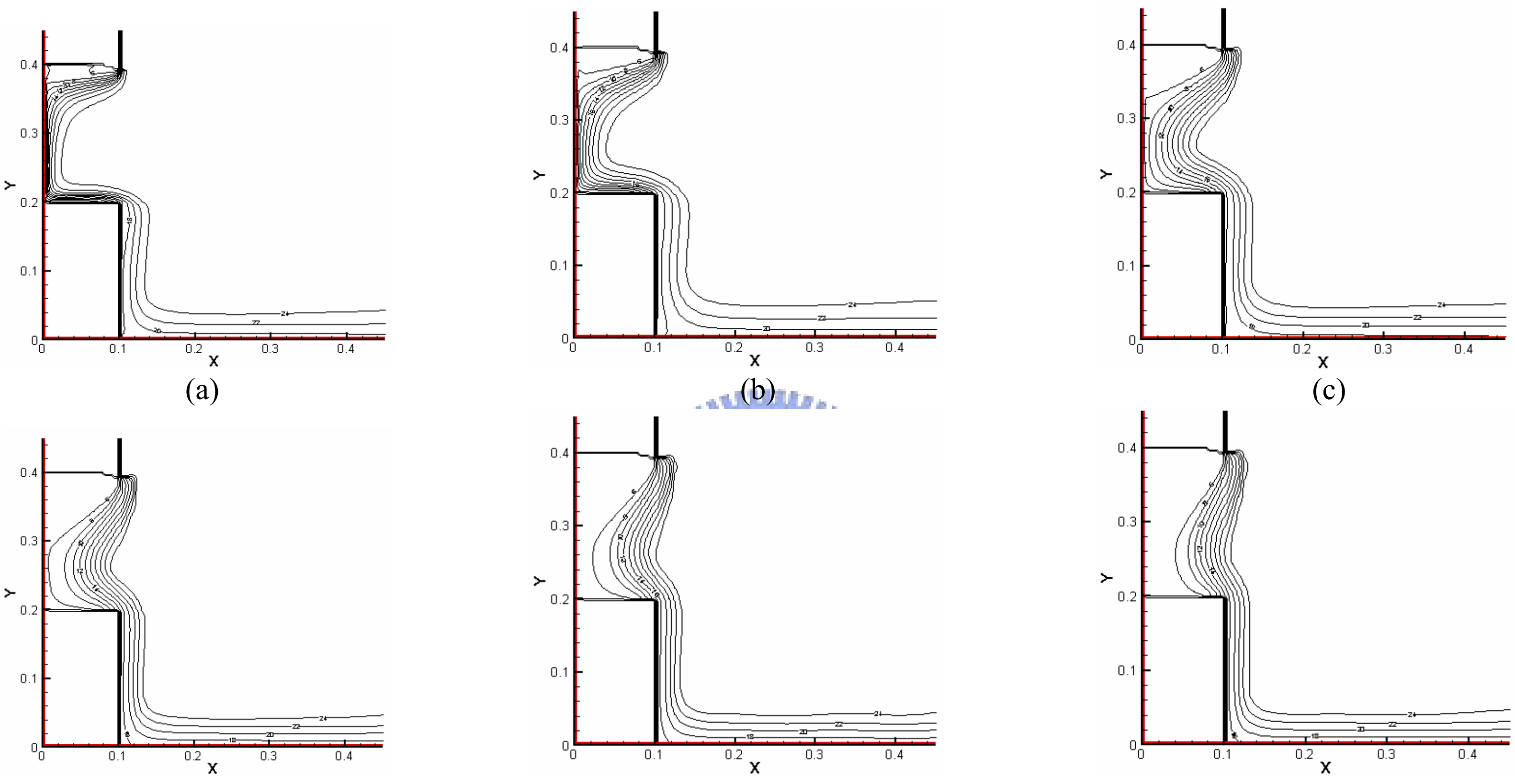

(a) (b) (c)

(d) (e) (f)

Fig. 4.25 Isotherms in the cavity for $b_j = 0.024m, Gr_t = 2.7\times10^7$ and N=$6.35\cdot10^{-2}$ with a jet inclined angle of -15° for $\mathrm{Re}_b =$ (a) 100.5 (V_j= 0.0583 m/s), (b) 215.3 (V_j= 0.125 m/s), (c) 430.7 (V_j= 0.25m/s), (d) 574.2 (V_j= 0.33m/s), (e) 646 (V_j= 0.375m/s), and (f) 717.8 (V_j= 0.416 m/s

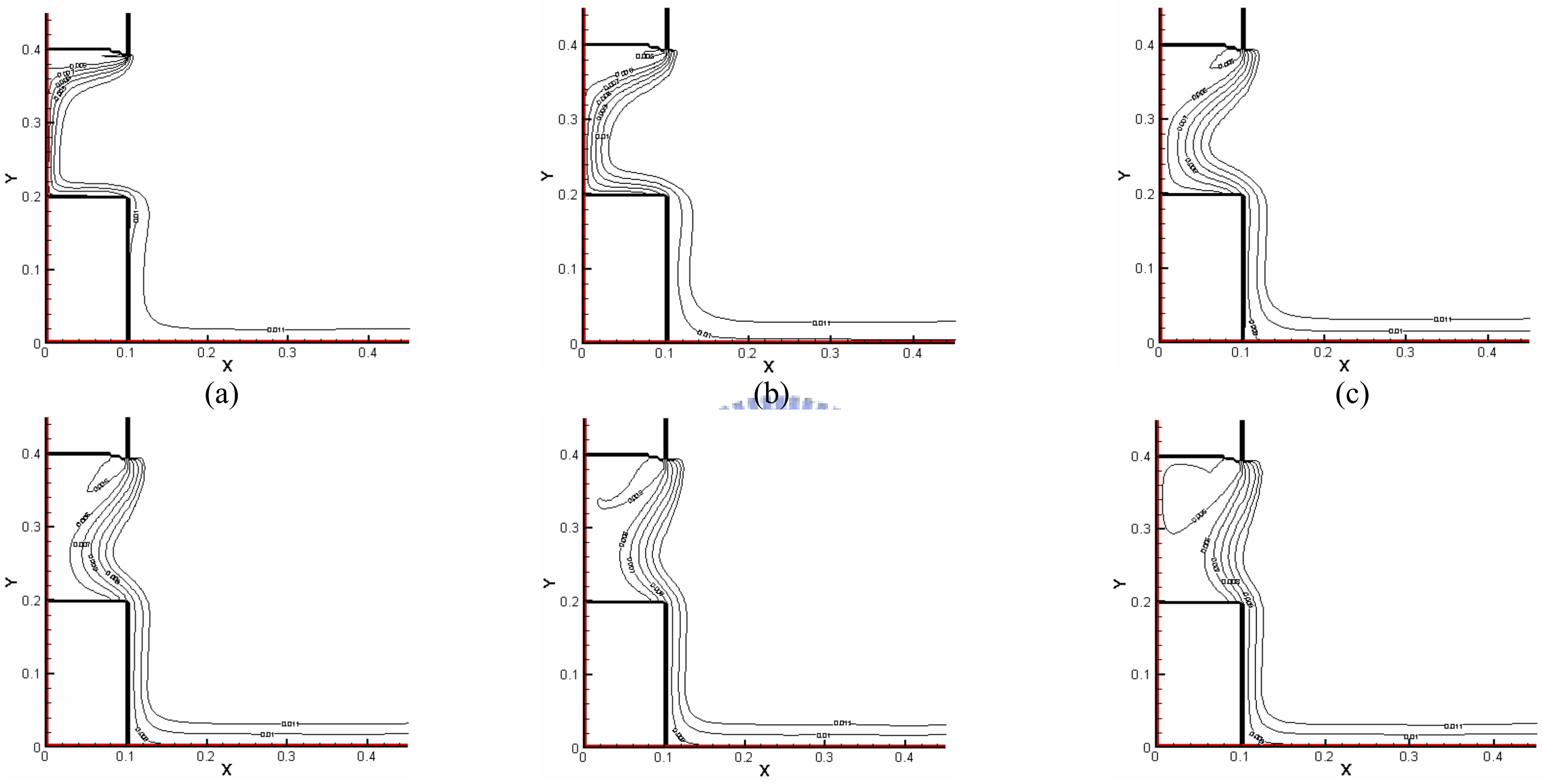

(a) (b) (c)

(d) (e) (f)

Fig. 4.26 Iso-concentration lines for $b_j = 0.024m, Gr_t = 2.7\times10^7$ and N=$6.35\cdot10^{-2}$ with a jet inclined angle of -15° for Re_b = (a) 100.5 (V_j= 0.0583 m/s), (b) 215.3 (V_j= 0.125 m/s), (c) 430.7 (V_j= 0.25m/s), (d) 574.2 (V_j= 0.33m/s), (e) 646 (V_j= 0.375m/s), and (f) 717.8 (V_j= 0.416 m/s

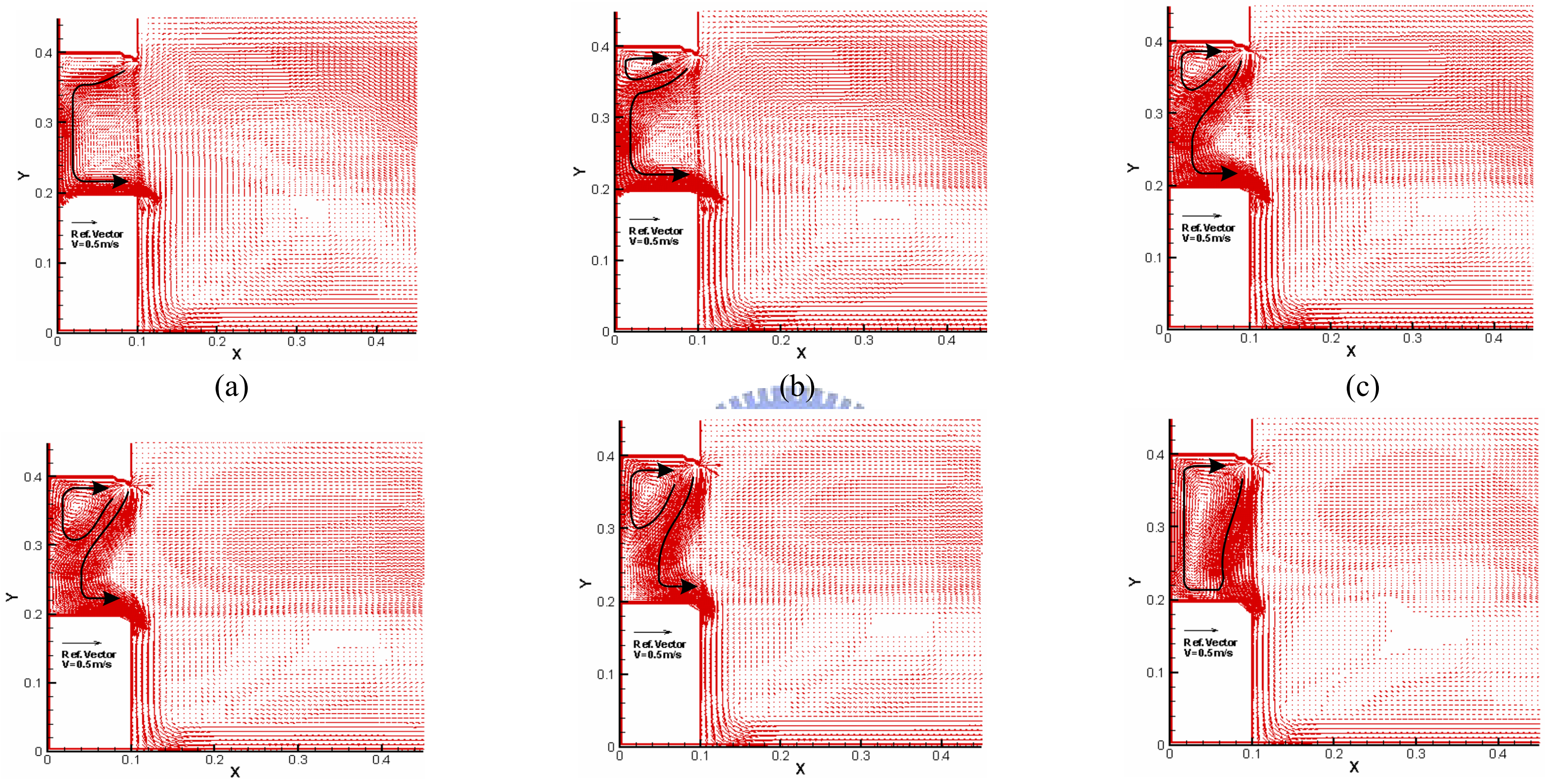

(a) (b) (c)

(d) (e) (f)

Fig. 4.27 Velocity vector maps for $b_j = 0.024m, Gr_t = 2.7\times10^7$ and N=$6.35\cdot10^{-2}$ with a jet inclined angle of -25° for Re_b = (a) 100.5 (V_j= 0.0583 m/s), (b) 215.3 (V_j= 0.125 m/s), (c) 430.7 (V_j= 0.25m/s), (d) 574.2 (V_j= 0.33m/s), (e) 646 (V_j= 0.375m/s), and (f) 717.8 (V_j= 0.416 m/s)

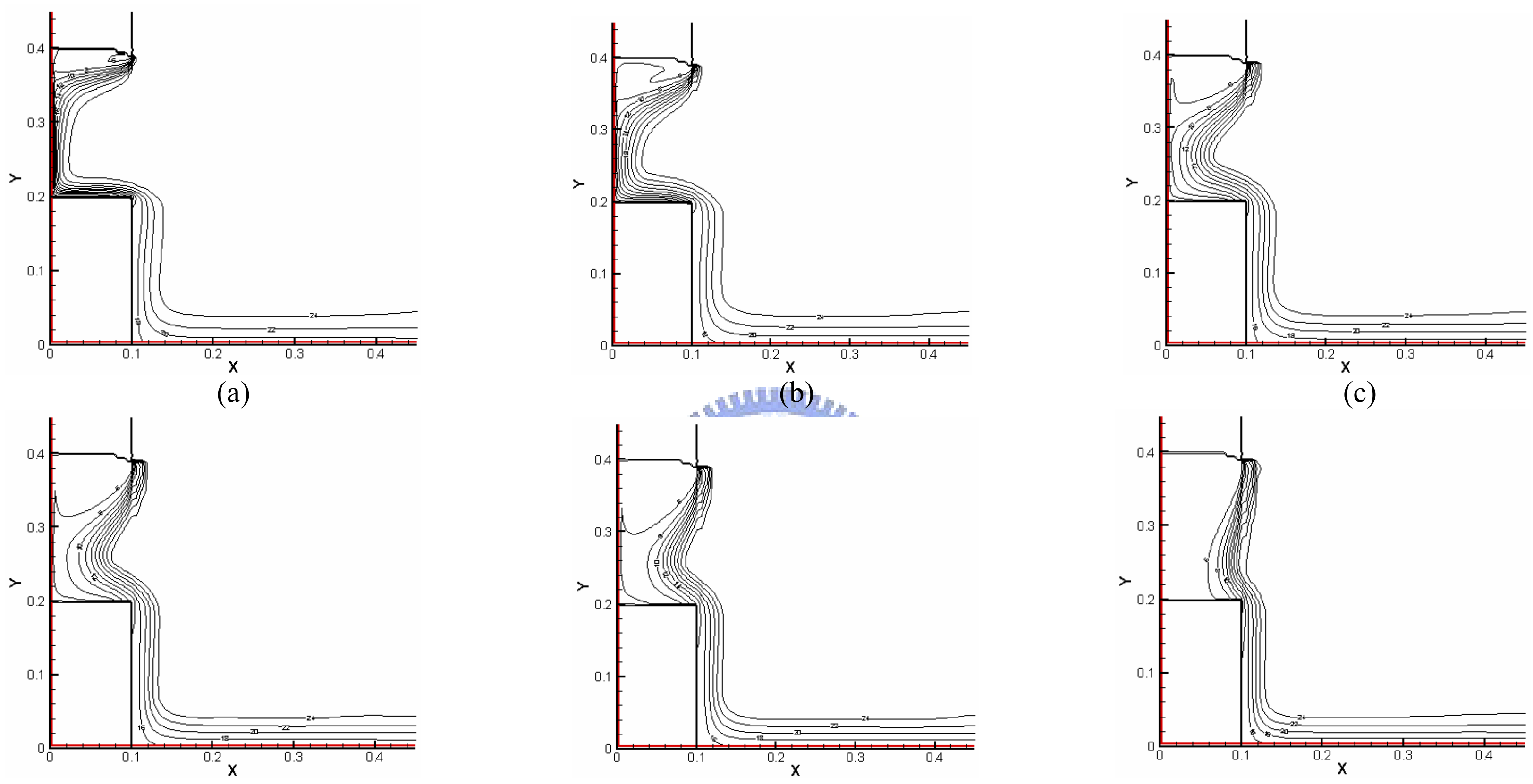

(a) (b) (c)

(d) (e) (f)

Fig. 4.28 Isotherms in the cavity for $b_j = 0.024m, Gr_t = 2.7\times10^7$ and N= $6.35\cdot10^{-2}$ with a jet inclined angle of -25° for $\text{Re}_b =$ (a) 100.5 (V_j = 0.0583 m/s), (b) 215.3 (V_j = 0.125 m/s), (c) 430.7 (V_j = 0.25m/s), (d) 574.2 (V_j = 0.33m/s), (e) 646 (V_j = 0.375m/s), and (f) 717.8 (V_j = 0.416 m/s)

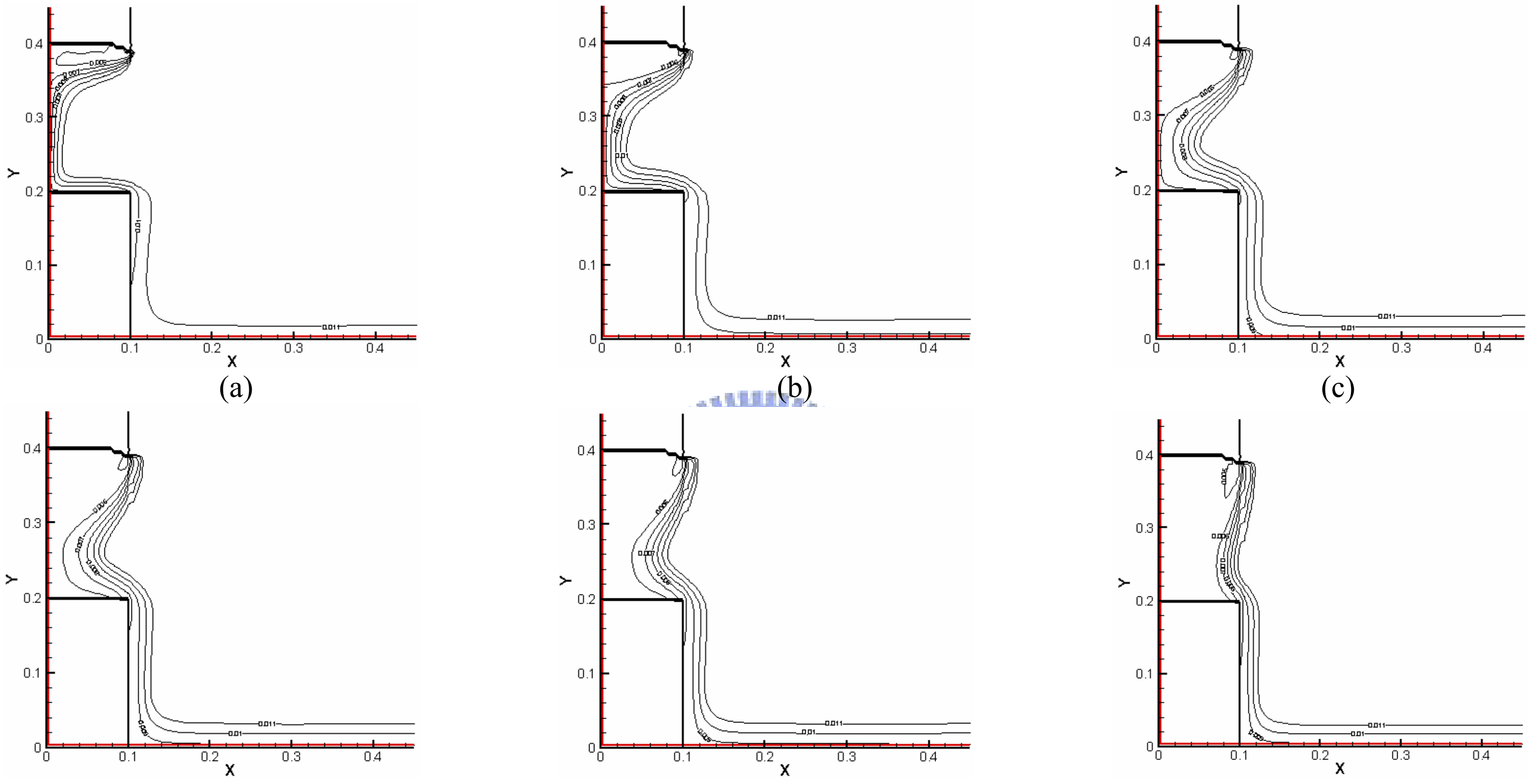

(a) (b) (c)

(d) (e) (f)

Fig. 4.29 Iso-concentration lines for $b_j = 0.024m, Gr_t = 2.7\times10^7$ and N=$6.35\cdot10^{-2}$ with a jet inclined angle of -25° for $\mathrm{Re}_b =$ (a) 100.5 (V_j= 0.0583 m/s), (b) 215.3 (V_j= 0.125 m/s), (c) 430.7 (V_j= 0.25m/s), (d) 574.2 (V_j= 0.33m/s), (e) 646 (V_j= 0.375m/s), and (f) 717.8 (V_j= 0.416 m/s)

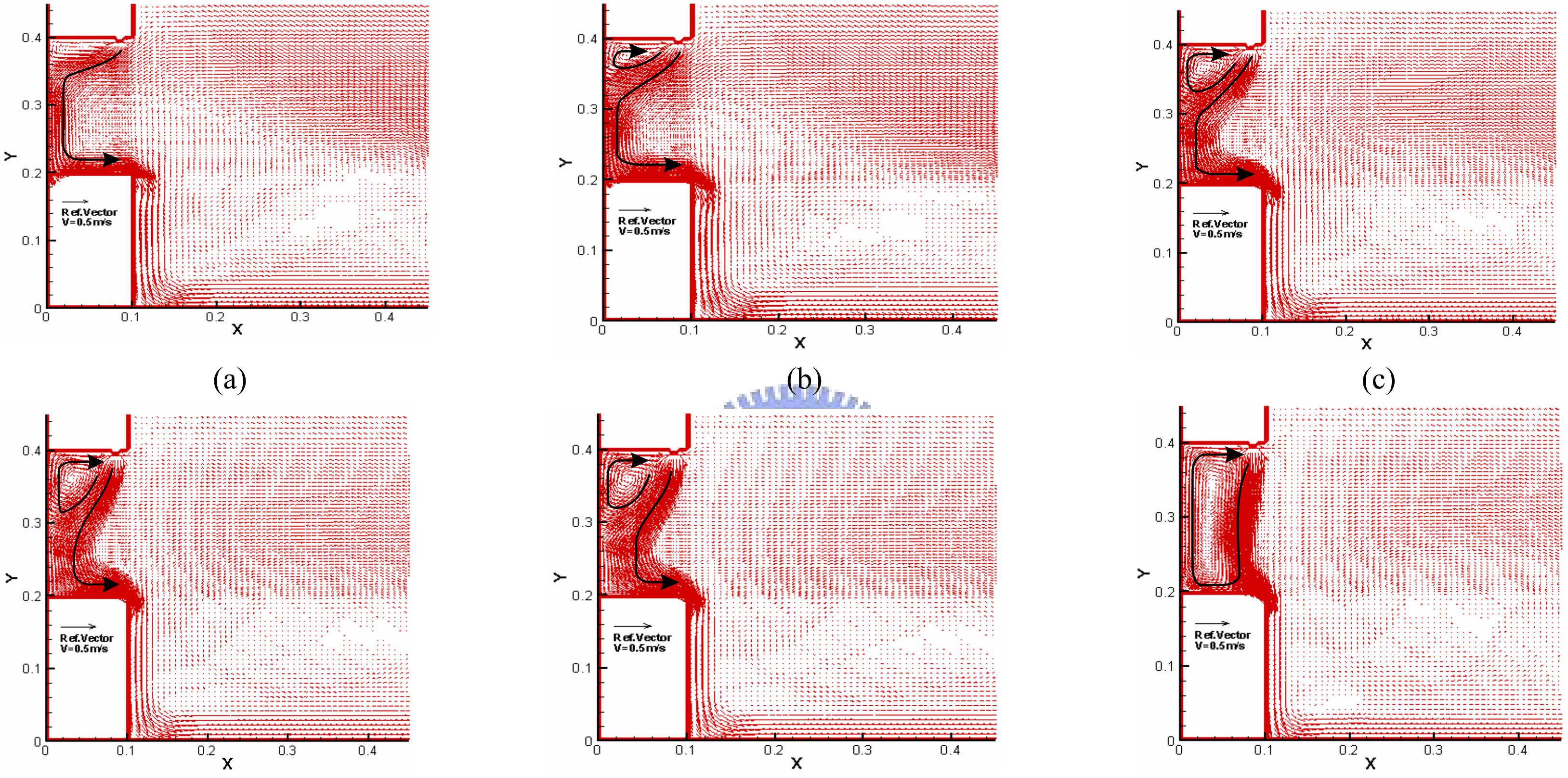

(a) (b) (c)

(d) (e) (f)

Fig. 4.30 Velocity vector maps for $b_j = 0.02m, Gr_t = 2.7\times10^7$ and N$=6.35\cdot10^{-2}$ with a jet inclined angle of 15° for $\mathrm{Re}_b =$ (a) 100.5 ($V_j =$ 0.07 m/s), (b) 215.3 ($V_j =$ 0.15 m/s), (c) 430.7 ($V_j =$ 0.3m/s), (d) 574.2 ($V_j =$ 0.4m/s), (e) 646 ($V_j =$ 0.45m/s), and (f) 717.8 ($V_j =$ 0.5 m/s)

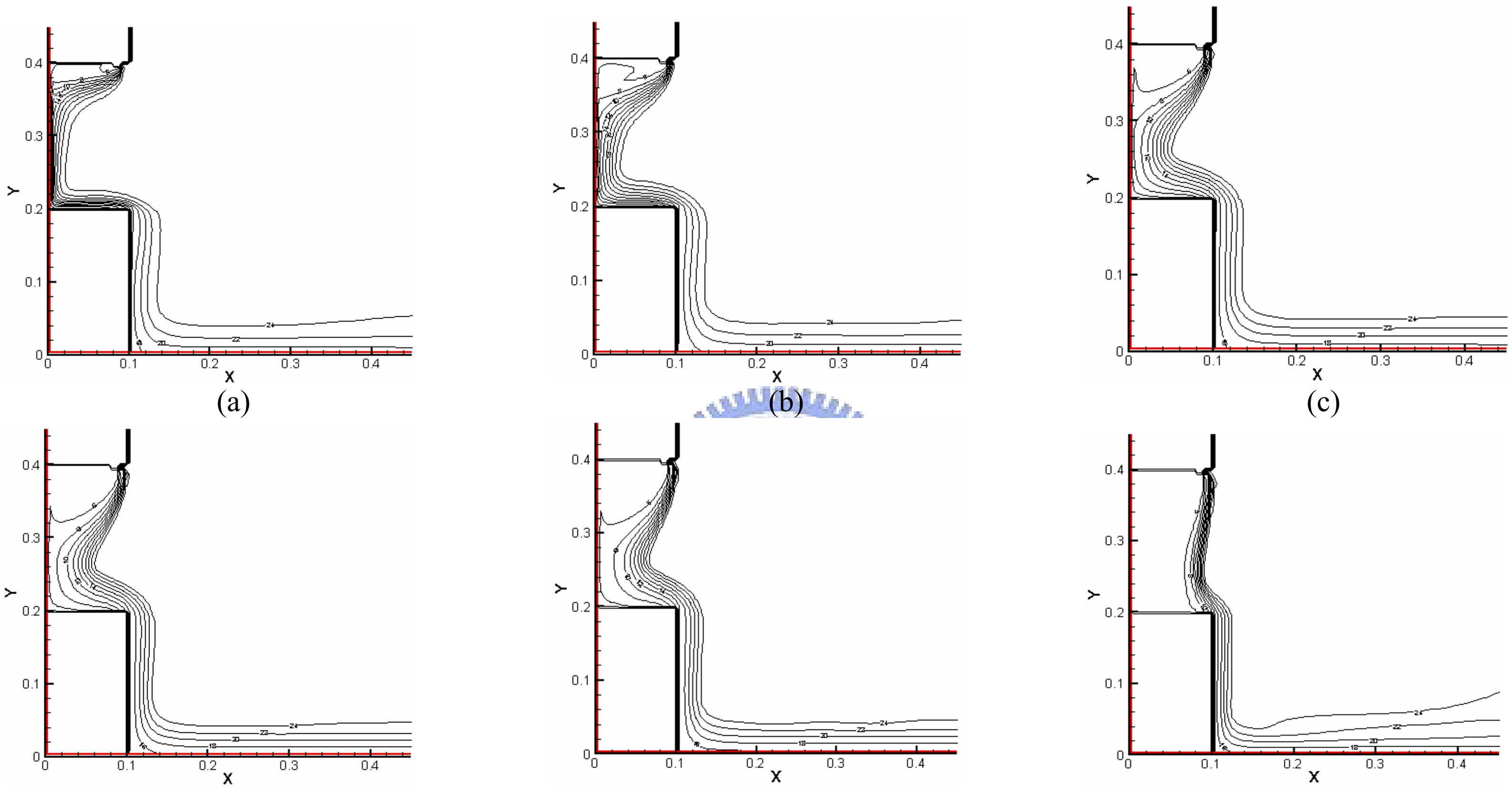

(a) (b) (c)

(d) (e) (f)

Fig. 4.31 Isotherms in the cavity for $b_j = 0.02m, Gr_t = 2.7\times10^7$ and N=$6.35\cdot10^{-2}$ with a jet inclined angle of 15° for Re_b = (a) 100.5 (V_j= 0.07 m/s), (b) 215.3 (V_j= 0.15 m/s), (c) 430.7 (V_j= 0.3m/s), (d) 574.2 (V_j= 0.4m/s), (e) 646 (V_j= 0.45m/s), and (f) 717.8 (V_j= 0.5 m/s)

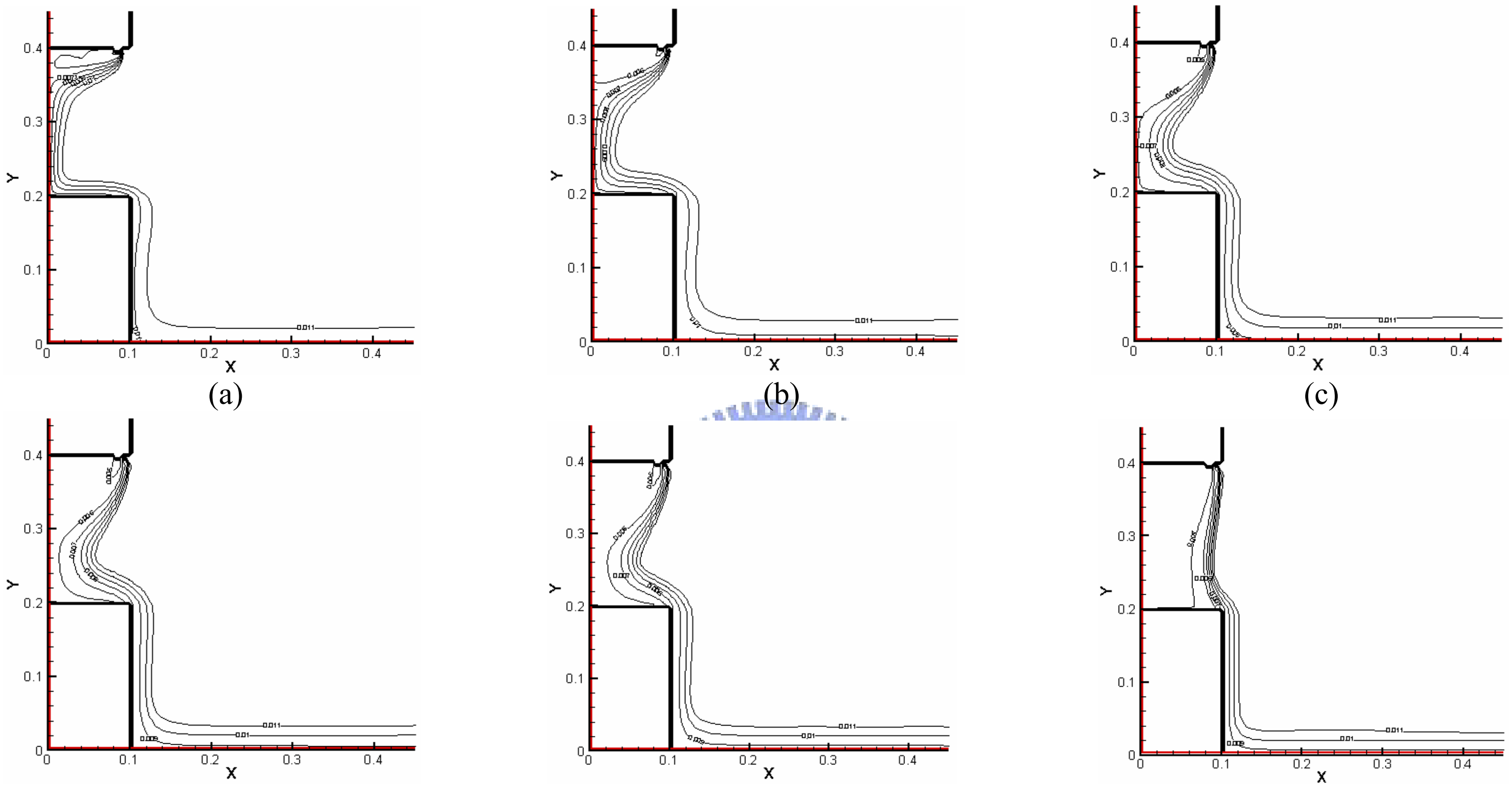

(a) (b) (c)

(d) (e) (f)

Fig. 4.32 Iso-concentration lines for $b_j = 0.02m, Gr_t = 2.7\times10^7$ and N=$6.35\cdot10^{-2}$ with a jet inclined angle of 15° for $\mathrm{Re}_b =$ (a) 100.5 (V_j= 0.07 m/s), (b) 215.3 (V_j= 0.15 m/s), (c) 430.7 (V_j= 0.3m/s), (d) 574.2 (V_j= 0.4m/s), (e) 646 (V_j= 0.45m/s), and (f) 717.8 (V_j= 0.5 m/s)

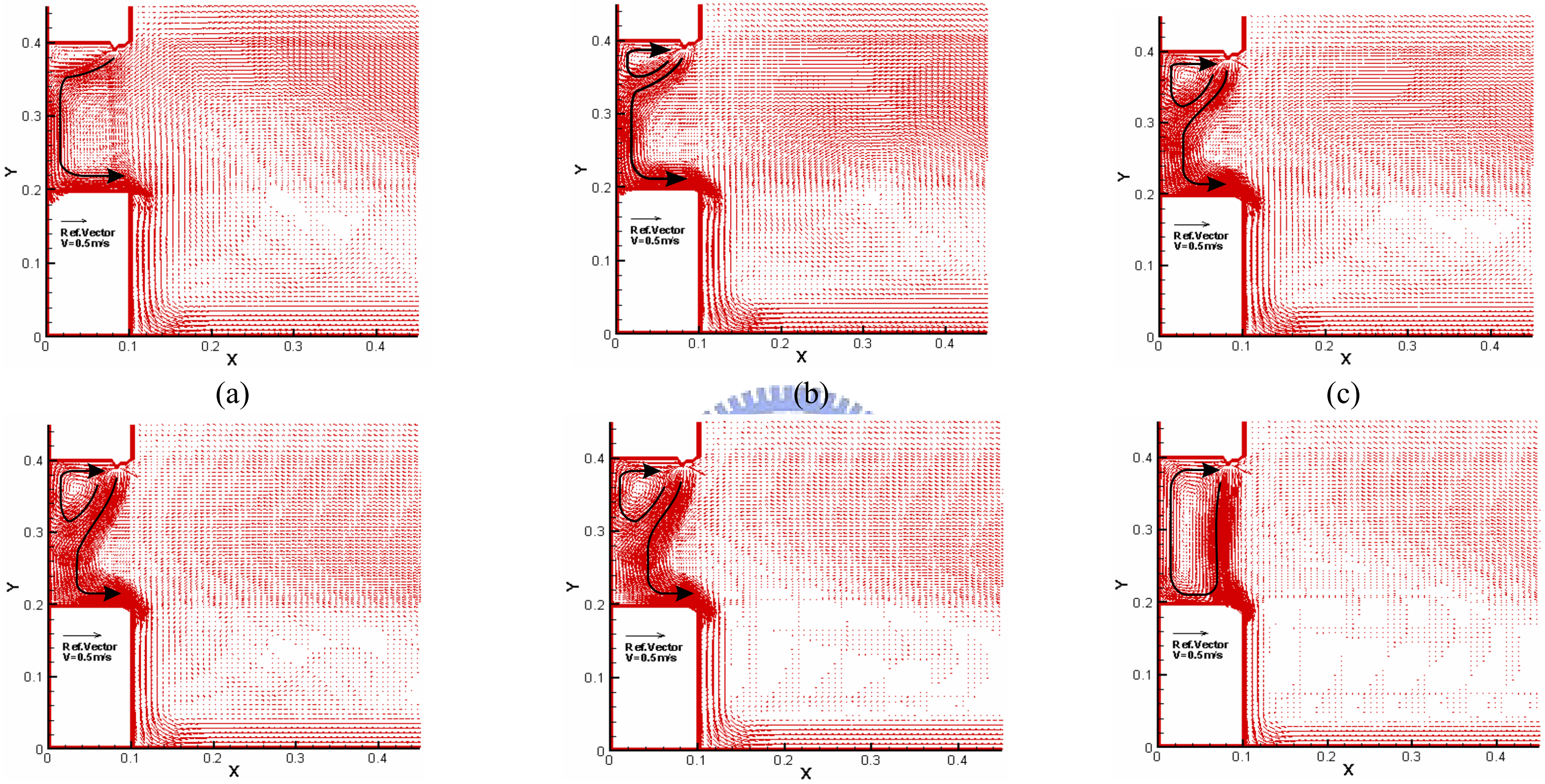

(a) (b) (c)

(d) (e) (f)

Fig. 4.33 Velocity vector maps for $b_j = 0.02m, Gr_t = 2.7 \times 10^7$ and N=$6.35 \cdot 10^{-2}$ with a jet inclined angle of 25° for $\mathrm{Re}_b =$ (a) 100.5 (V_j = 0.07 m/s), (b) 215.3 (V_j = 0.15 m/s), (c) 430.7 (V_j = 0.3m/s), (d) 574.2 (V_j = 0.4m/s), (e) 646 (V_j = 0.45m/s), and (f) 717.8 (V_j = 0.5 m/s)

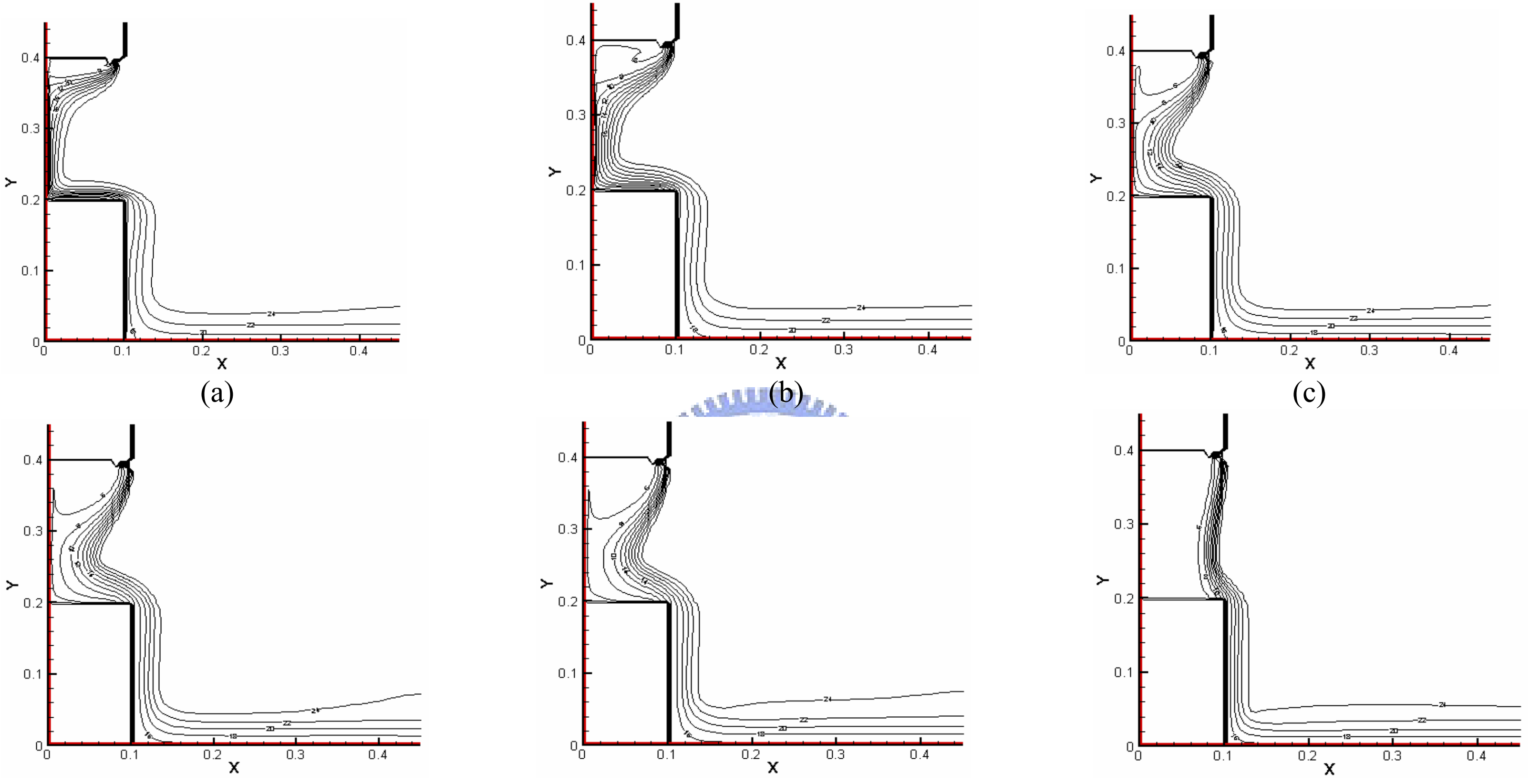

(a) (b) (c)

(d) (e) (f)

Fig. 4.34 Isotherms in the cavity for $b_j = 0.02m, Gr_t = 2.7\times10^7$ and N=$6.35\cdot10^{-2}$ with a jet inclined angle of 25° $\mathrm{Re}_b =$ (a) 100.5 (V_j = 0.07 m/s), (b) 215.3 (V_j = 0.15 m/s), (c) 430.7 (V_j = 0.3m/s), (d) 574.2 (V_j = 0.4m/s), (e) 646 (V_j = 0.45m/s), and (f) 717.8 (V_j = 0.5 m/s)

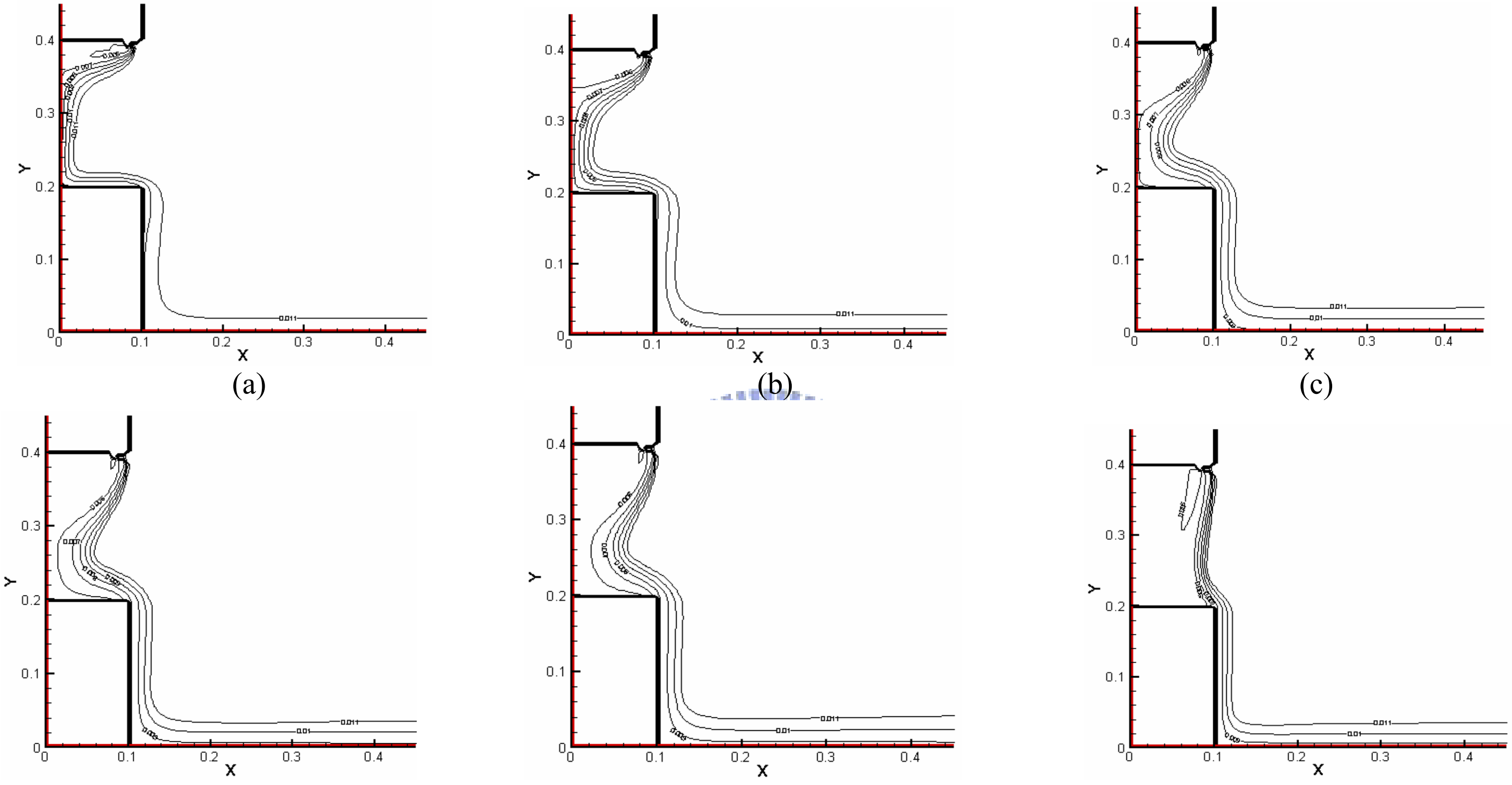

(a) (b) (c)

(d) (e) (f)

Fig. 4.35 Iso-concentration lines for $b_j = 0.02m, Gr_t = 2.7\times10^7$ and N=$6.35\cdot10^{-2}$ with a jet inclined angle of 25° for $\mathrm{Re}_b =$ (a) 100.5 (V_j = 0.07 m/s), (b) 215.3 (V_j = 0.15 m/s), (c) 430.7 (V_j = 0.3m/s), (d) 574.2 (V_j = 0.4m/s), (e) 646 (V_j = 0.45m/s), and (f) 717.8 (V_j = 0.5 m/s)

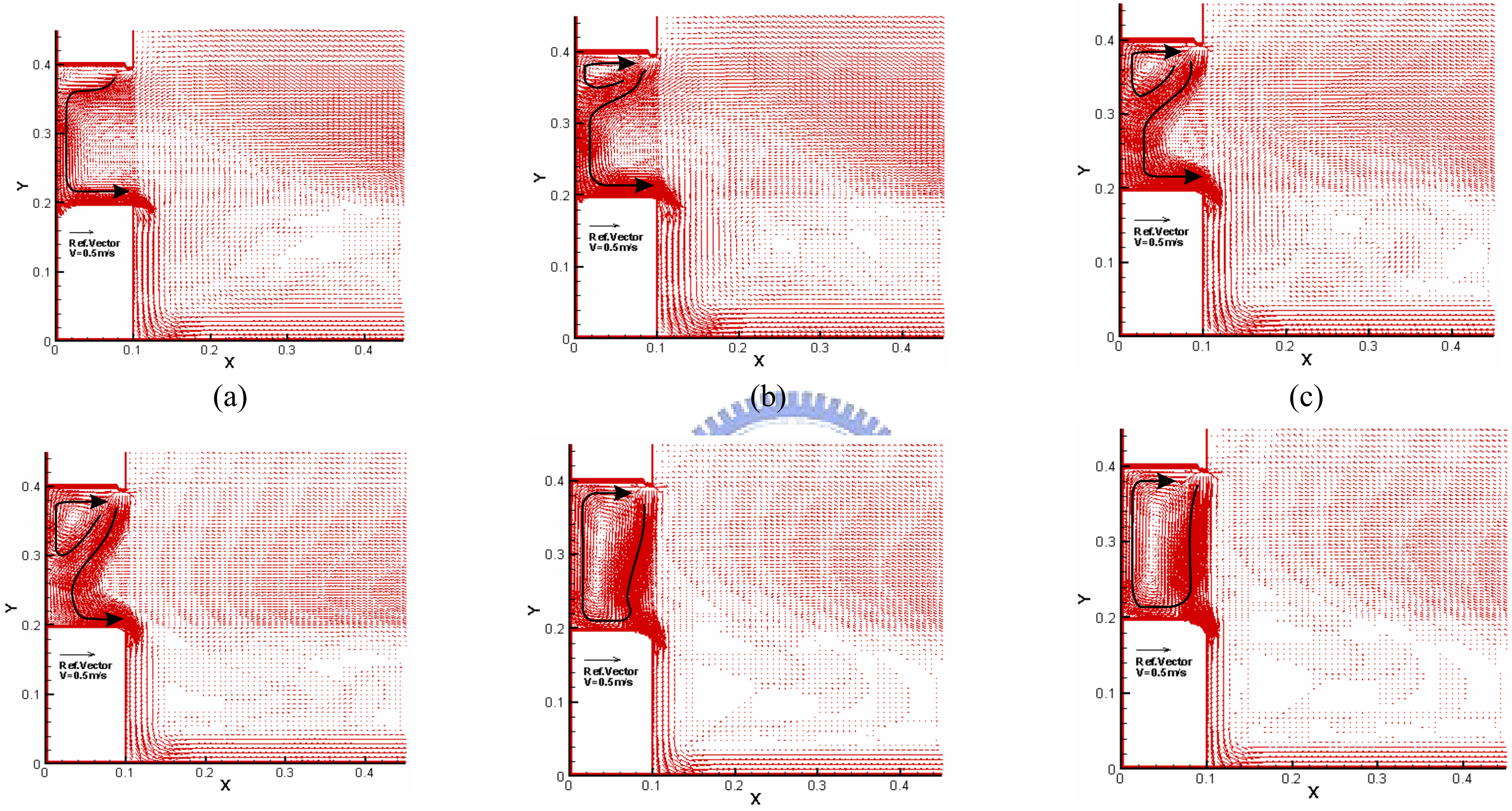

(a) (b) (c)

(d) (e) (f)

Fig. 4.36 Velocity vector maps for $b_j = 0.02m, Gr_t = 2.7\times10^7$ and N=$6.35\cdot10^{-2}$ with a jet inclined angle of -15° for Re_b = (a) 100.5 (V_j= 0.07 m/s), (b) 215.3 (V_j= 0.15 m/s), (c) 430.7 (V_j= 0.3m/s), (d) 574.2 (V_j= 0.4m/s), (e) 646 (V_j= 0.45m/s), and (f) 717.8 (V_j= 0.5 m/s)

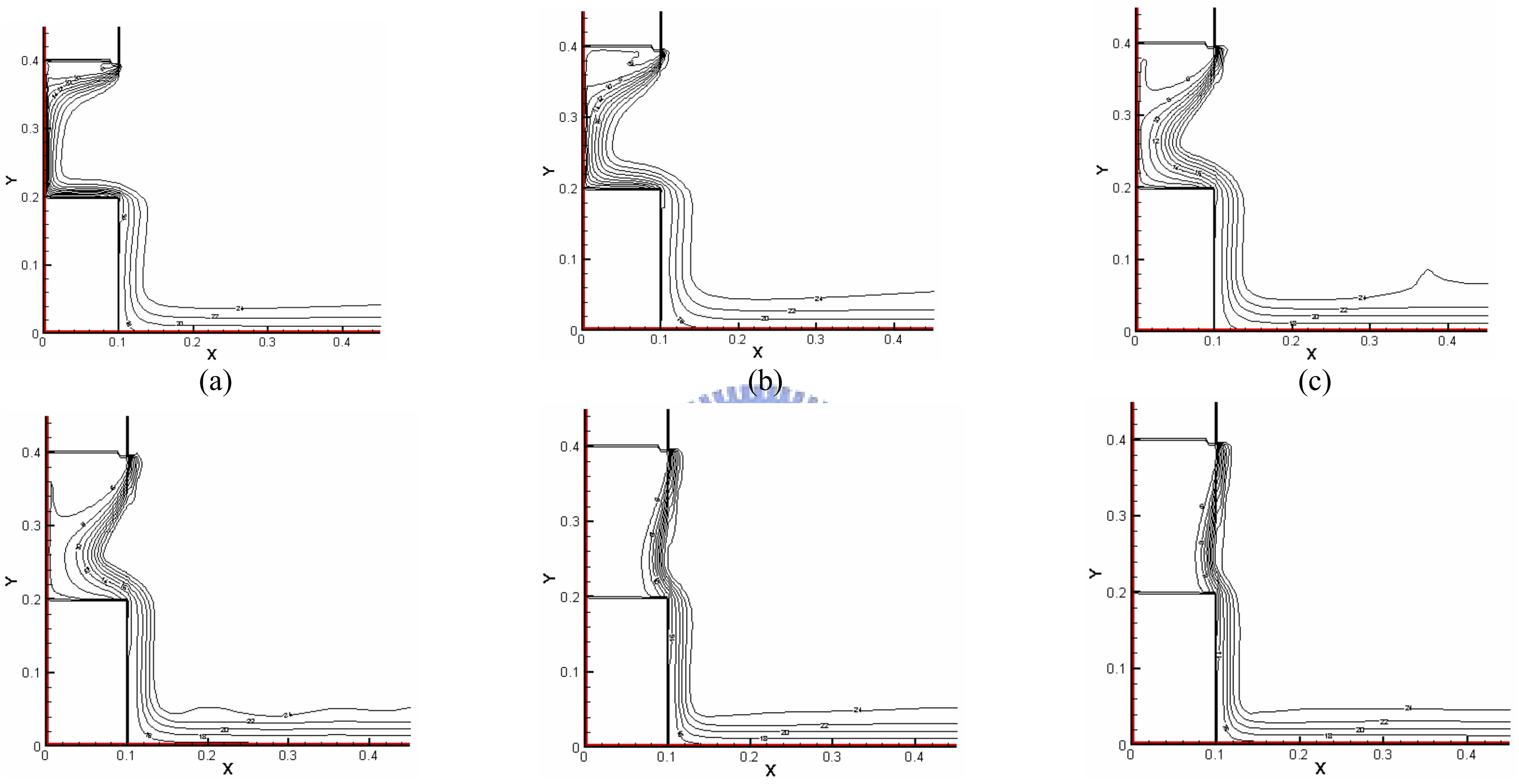

(a) (b) (c)

(d) (e) (f)

Fig. 4.37 Isotherms in the cavity for $b_j = 0.02m, Gr_t = 2.7\times10^7$ and N= $6.35\cdot10^{-2}$ with a jet inclined angle of -15° for $\mathrm{Re}_b =$ (a) 100.5 (V_j= 0.07 m/s), (b) 215.3 (V_j= 0.15 m/s), (c) 430.7 (V_j= 0.3m/s), (d) 574.2 (V_j= 0.4m/s), (e) 646 (V_j= 0.45m/s), and (f) 717.8 (V_j= 0.5 m/s)

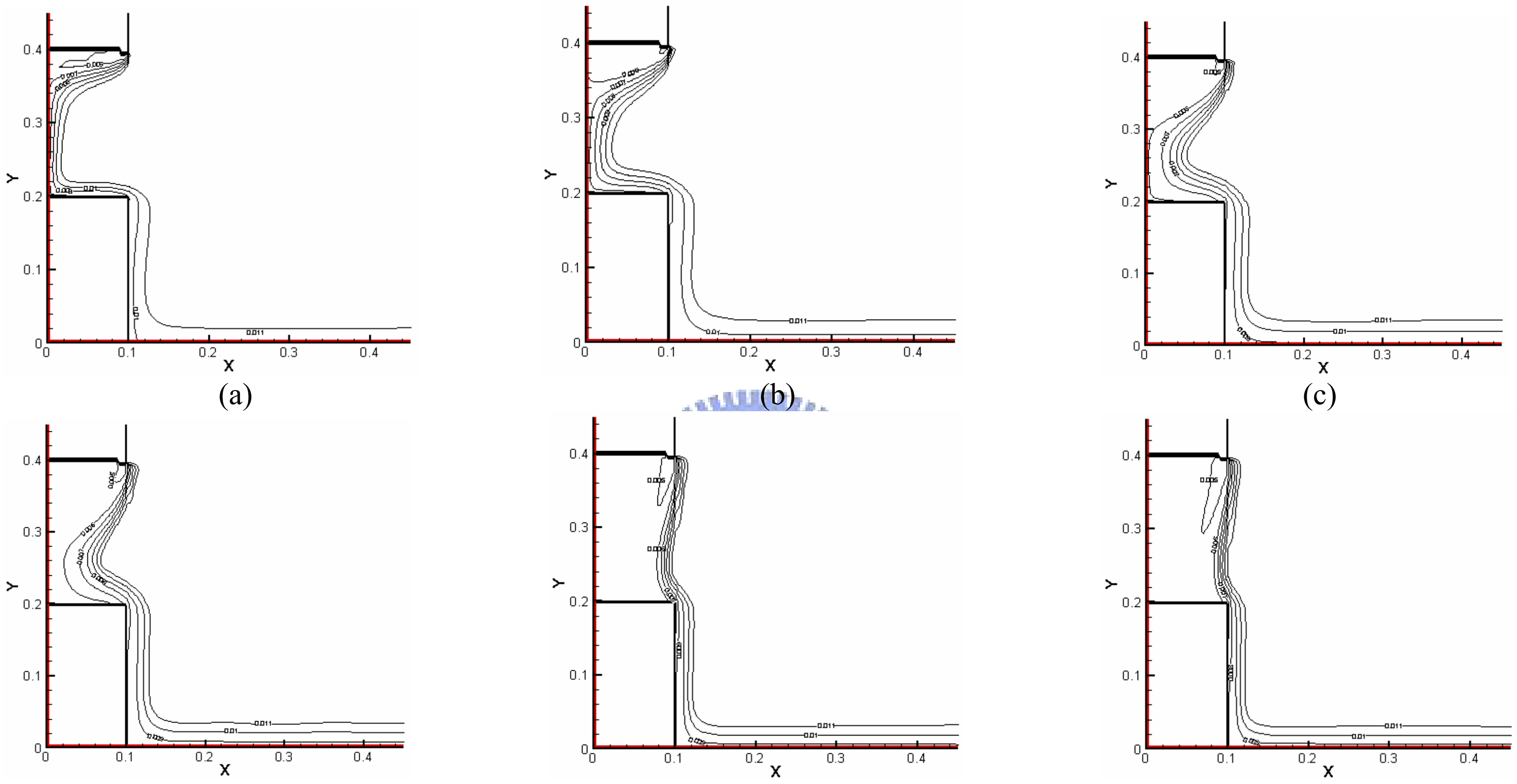

(a) (b) (c)

(d) (e) (f)

Fig. 4.38 Iso-concentration lines for $b_j = 0.02m, Gr_t = 2.7\times10^7$ and N=$6.35\cdot10^{-2}$ with a jet inclined angle of -15° for $\mathrm{Re}_b =$ (a) 100.5 (V_j= 0.07 m/s), (b) 215.3 (V_j= 0.15 m/s), (c) 430.7 (V_j= 0.3m/s), (d) 574.2 (V_j= 0.4m/s), (e) 646 (V_j= 0.45m/s), and (f) 717.8 (V_j= 0.5 m/s)

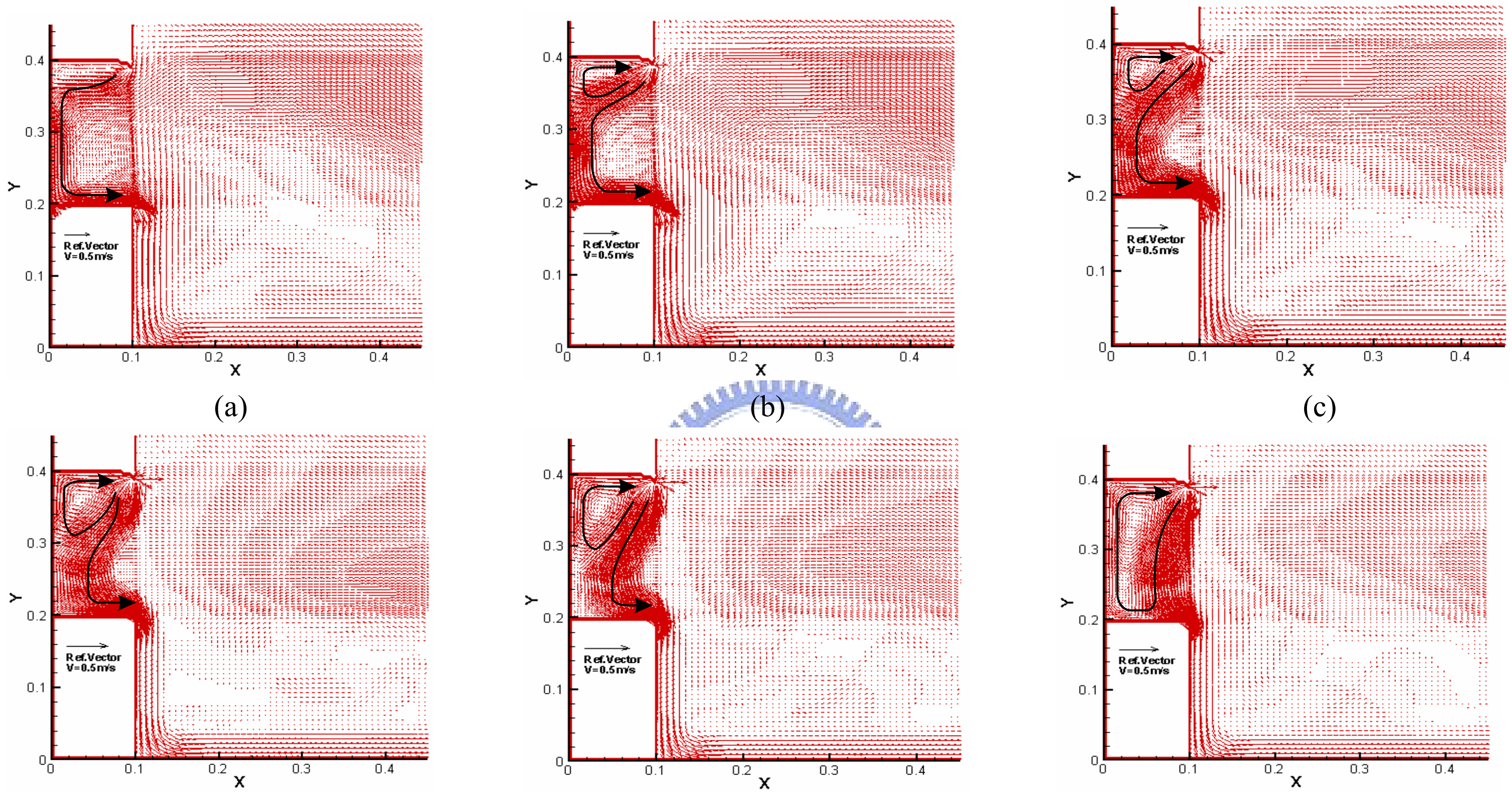

(a) (b) (c)

(d) (e) (f)

Fig. 4.39 Velocity vector maps for $b_j = 0.02m$, $Gr_t = 2.7\times10^7$ and N=$6.35\cdot10^{-2}$ with a jet inclined angle of -25° for Re_b = (a) 100.5 (V_j = 0.07 m/s), (b) 215.3 (V_j = 0.15 m/s), (c) 430.7 (V_j = 0.3m/s), (d) 574.2 (V_j = 0.4m/s), (e) 646 (V_j = 0.45m/s), and (f) 717.8 (V_j = 0.5 m/s)

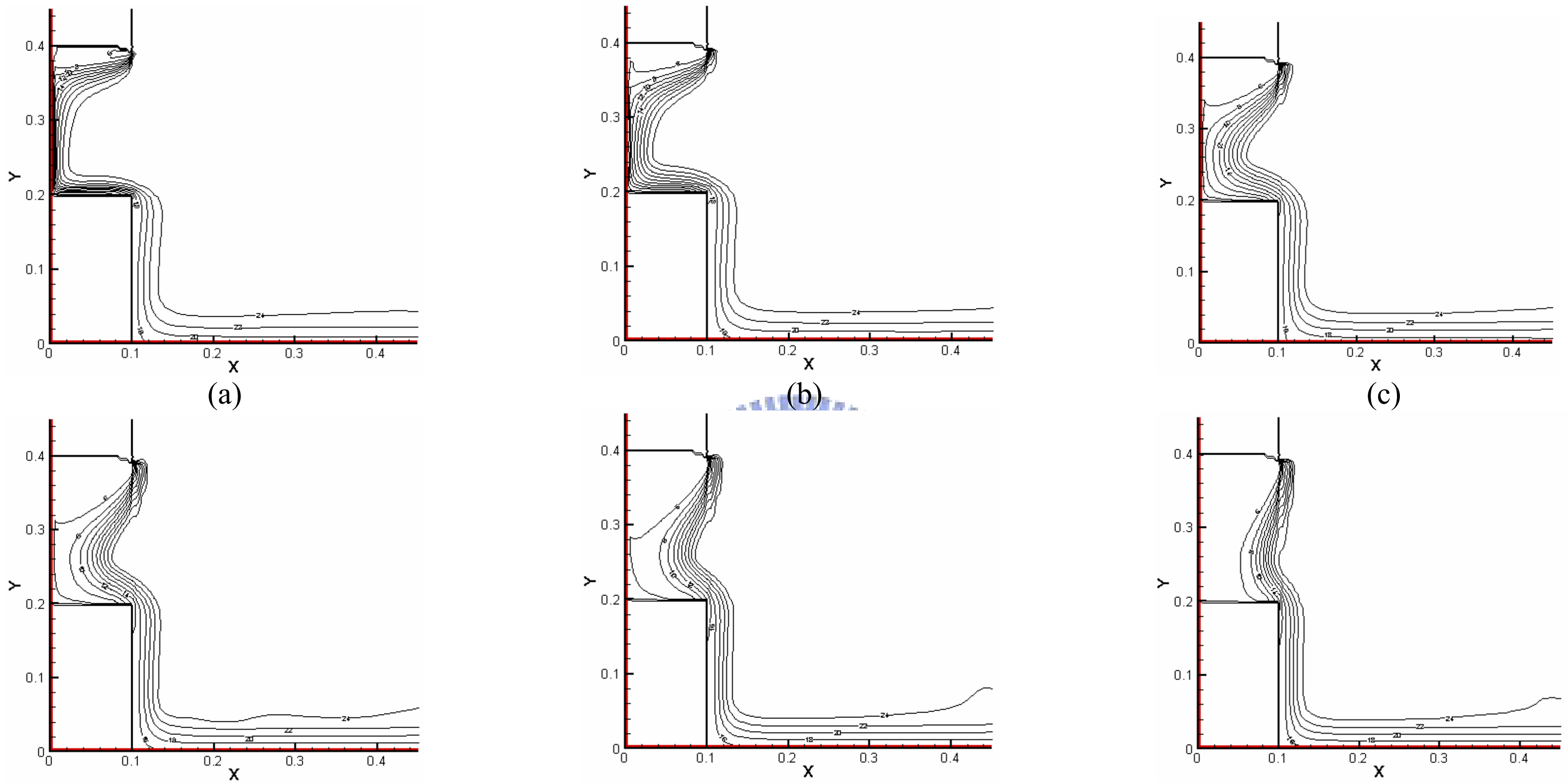

Fig. 4.40 Isotherms in the cavity for $b_j = 0.02m, Gr_t = 2.7\times10^7$ and N= $6.35\cdot10^{-2}$ with a jet inclined angle of -25° for $\mathrm{Re}_b =$ (a) 100.5 (V_j = 0.07 m/s), (b) 215.3 (V_j = 0.15 m/s), (c) 430.7 (V_j = 0.3m/s), (d) 574.2 (V_j = 0.4m/s), (e) 646 (V_j = 0.45m/s), and (f) 717.8 (V_j = 0.5 m/s)

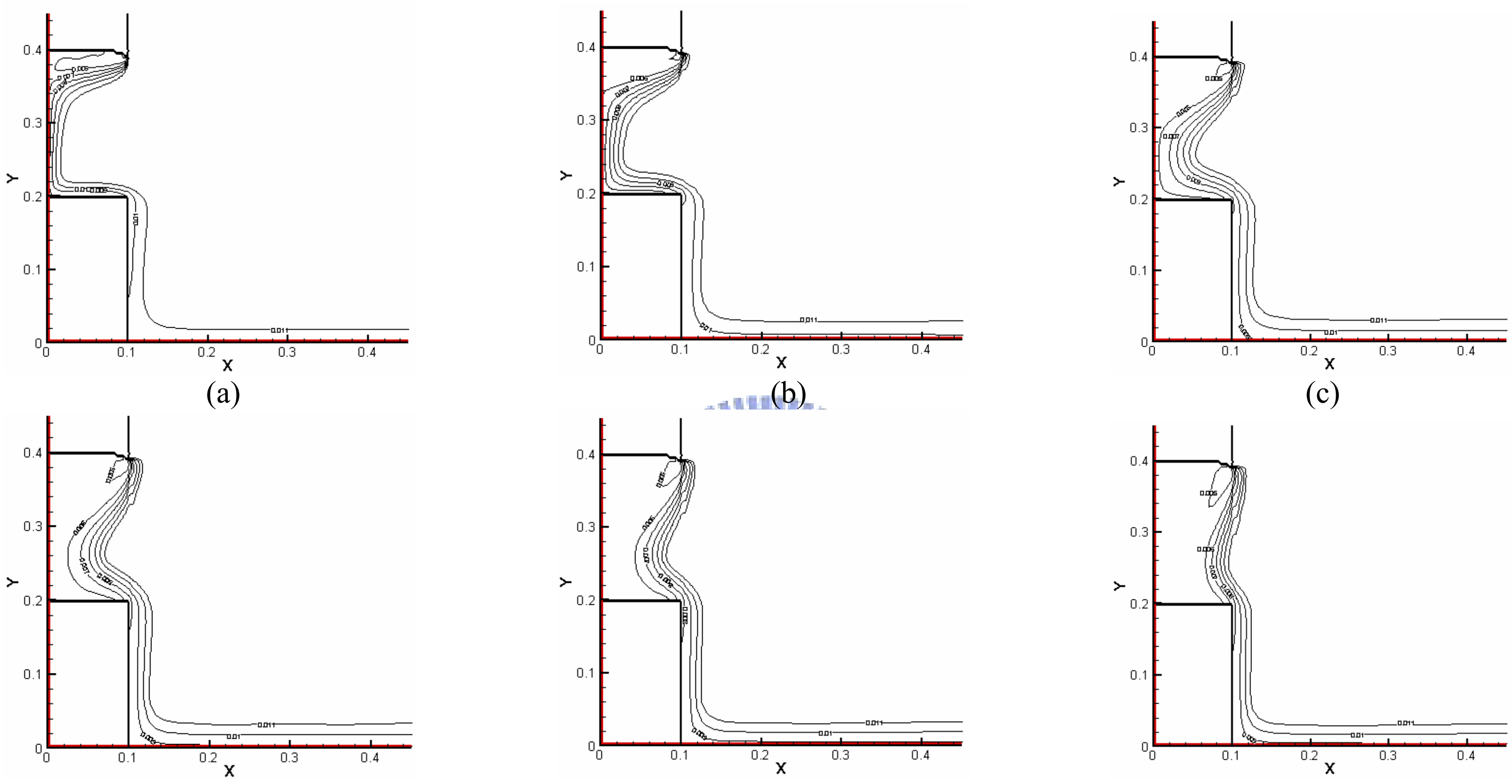

(a) (b) (c)

(d) (e) (f)

Fig. 4.41 Iso-concentration lines for $b_j = 0.02m, Gr_t = 2.7\times10^7$ and N= $6.35\cdot10^{-2}$ with a jet inclined angle of-25° for $\mathrm{Re}_b =$ (a) 100.5 (V_j = 0.07 m/s), (b) 215.3 (V_j = 0.15 m/s), (c) 430.7 (V_j = 0.3m/s), (d) 574.2 (V_j = 0.4m/s), (e) 646 (V_j = 0.45m/s), and (f) 717.8 (V_j = 0.5 m/s)

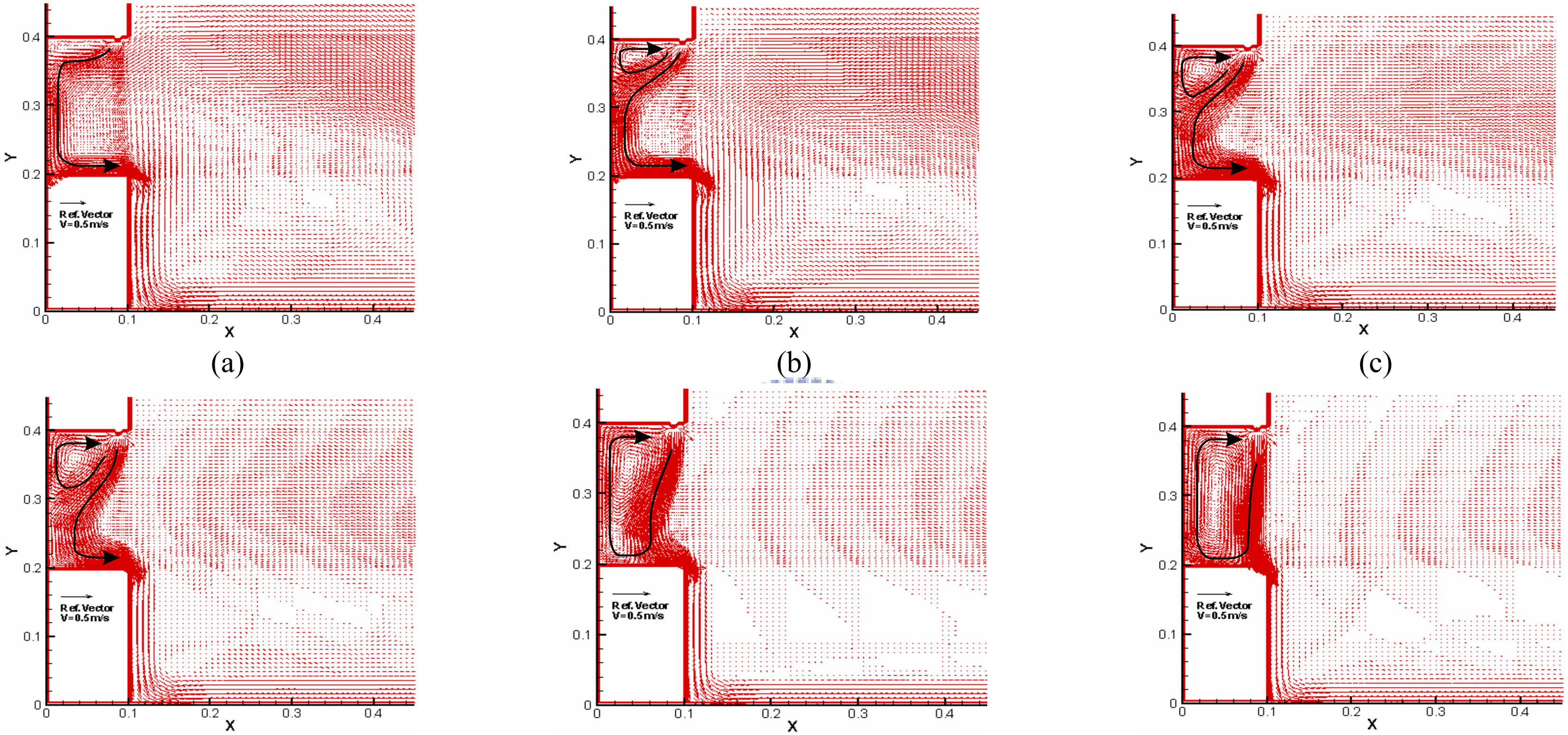

(a) (b) (c)

(d) (e) (f)

Fig. 4.42 Velocity vector maps for $b_j = 0.016m, Gr_t = 2.7\times10^7$ and $N = 6.35\cdot10^{-2}$ with a jet inclined angle of 15° for $\mathrm{Re}_b =$ (a) 100.5 (V_j = 0.0875 m/s), (b) 215.3 (V_j = 0.187 m/s), (c) 430.7 (V_j = 0.375m/s), (d) 574.2 (V_j = 0.5m/s), (e) 646 (V_j = 0.56m/s), and (f) 717.8 (V_j = 0.62 m/s)

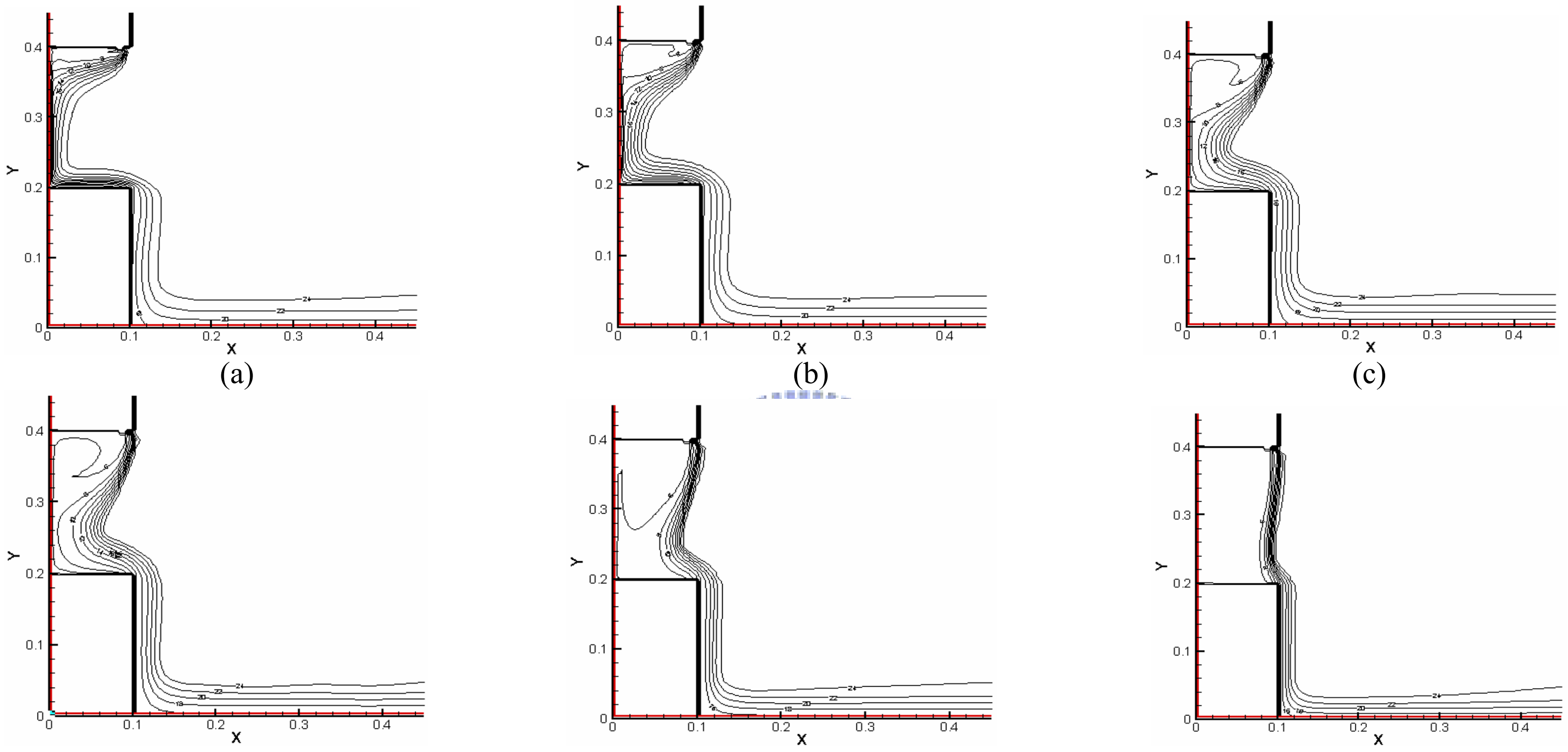

(a) (b) (c)

(d) (e) (f)

Fig. 4.43 Isotherms in the cavity for $b_j = 0.016m$, $Gr_t = 2.7\times10^7$ and N= $6.35\cdot10^{-2}$ with a jet inclined angle of 15° for $\mathrm{Re}_b =$ (a) 100.5 (V_j= 0.0875 m/s), (b) 215.3 (V_j= 0.187 m/s), (c) 430.7 (V_j= 0.375m/s), (d) 574.2 (V_j= 0.5m/s), (e) 646 (V_j= 0.56m/s), and (f) 717.8 (V_j= 0.62 m/s)

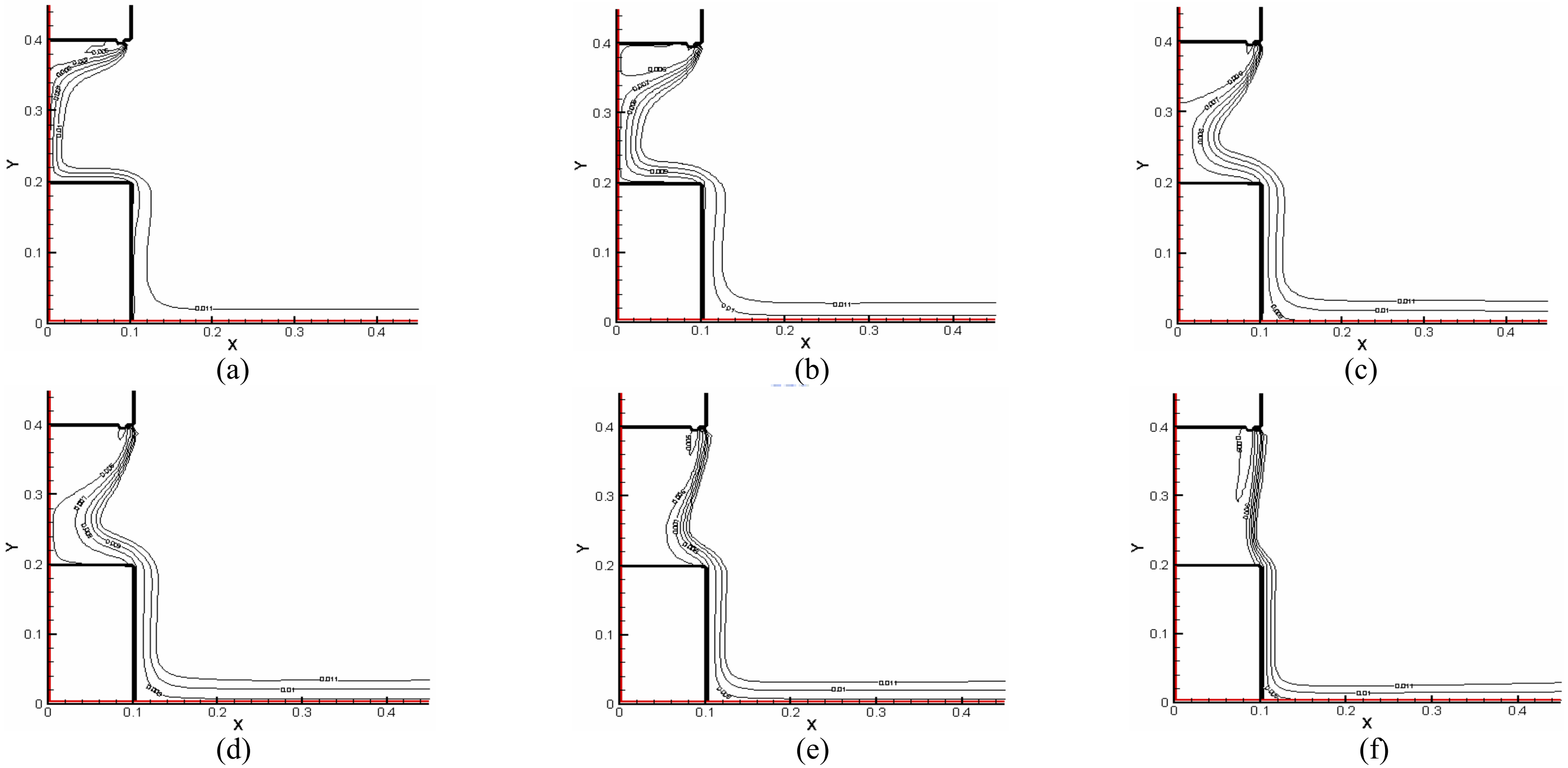

Fig. 4.44 Iso-concentration lines for $b_j = 0.016m, Gr_t = 2.7\times10^7$ and N=$6.35\cdot10^{-2}$ with a jet inclined angle of 15° for $\mathrm{Re}_b =$ (a) 100.5 (V_j= 0.0875 m/s), (b) 215.3 (V_j= 0.187 m/s), (c) 430.7 (V_j= 0.375m/s), (d) 574.2 (V_j= 0.5m/s), (e) 646 (V_j= 0.56m/s), and (f) 717.8 (V_j= 0.62 m/s)

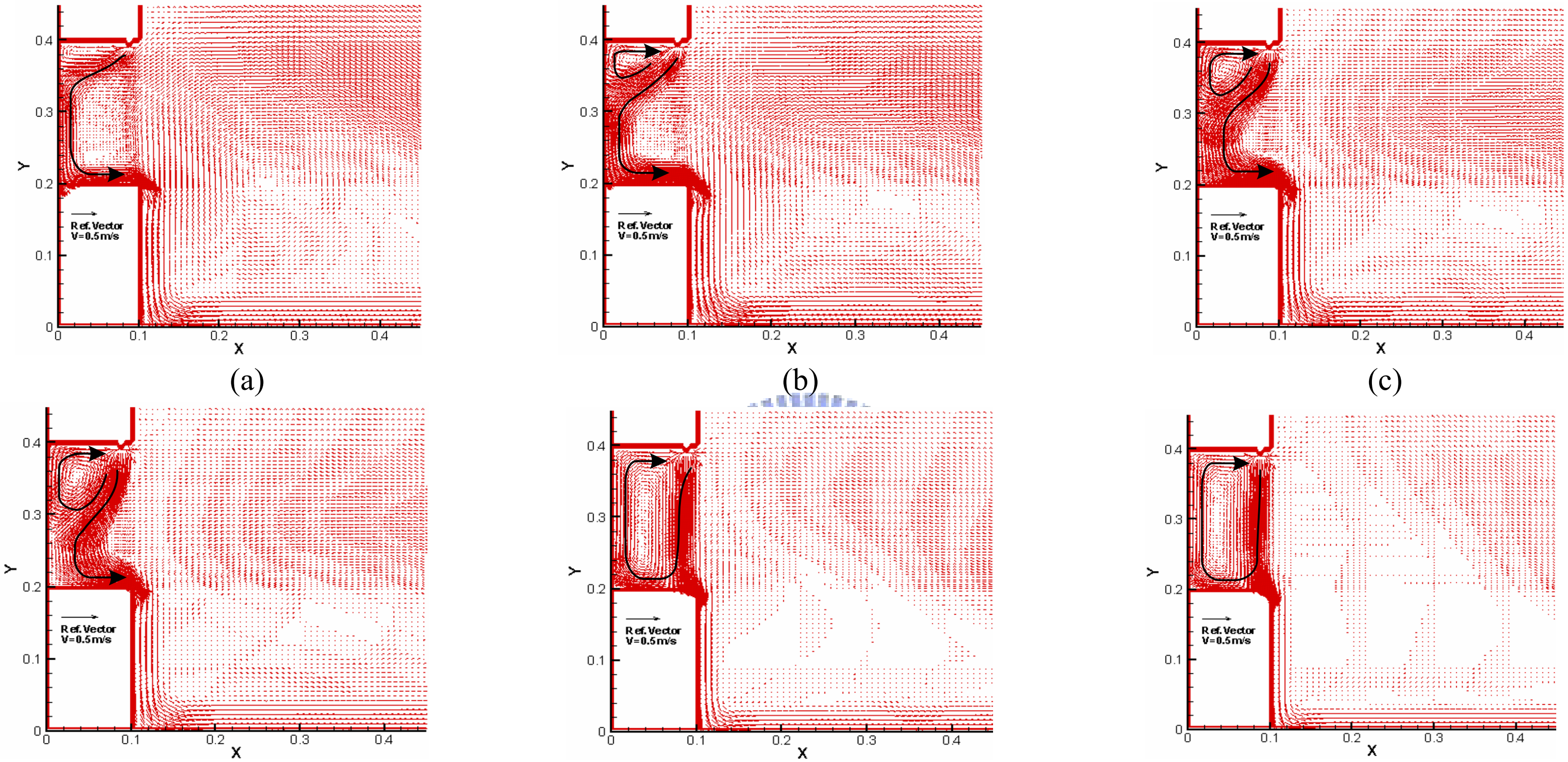

(a) (b) (c)

(d) (e) (f)

Fig. 4.45 Velocity vector maps for $b_j = 0.016m, Gr_t = 2.7\times10^7$ and N=$6.35\cdot10^{-2}$ with a jet inclined angle of 25° for $\mathrm{Re}_b =$ (a) 100.5 (V_j = 0.0875 m/s), (b) 215.3 (V_j = 0.187 m/s), (c) 430.7 (V_j = 0.375m/s), (d) 574.2 (V_j = 0.5m/s), (e) 646 (V_j = 0.56m/s), and (f) 717.8 (V_j = 0.62 m/s)

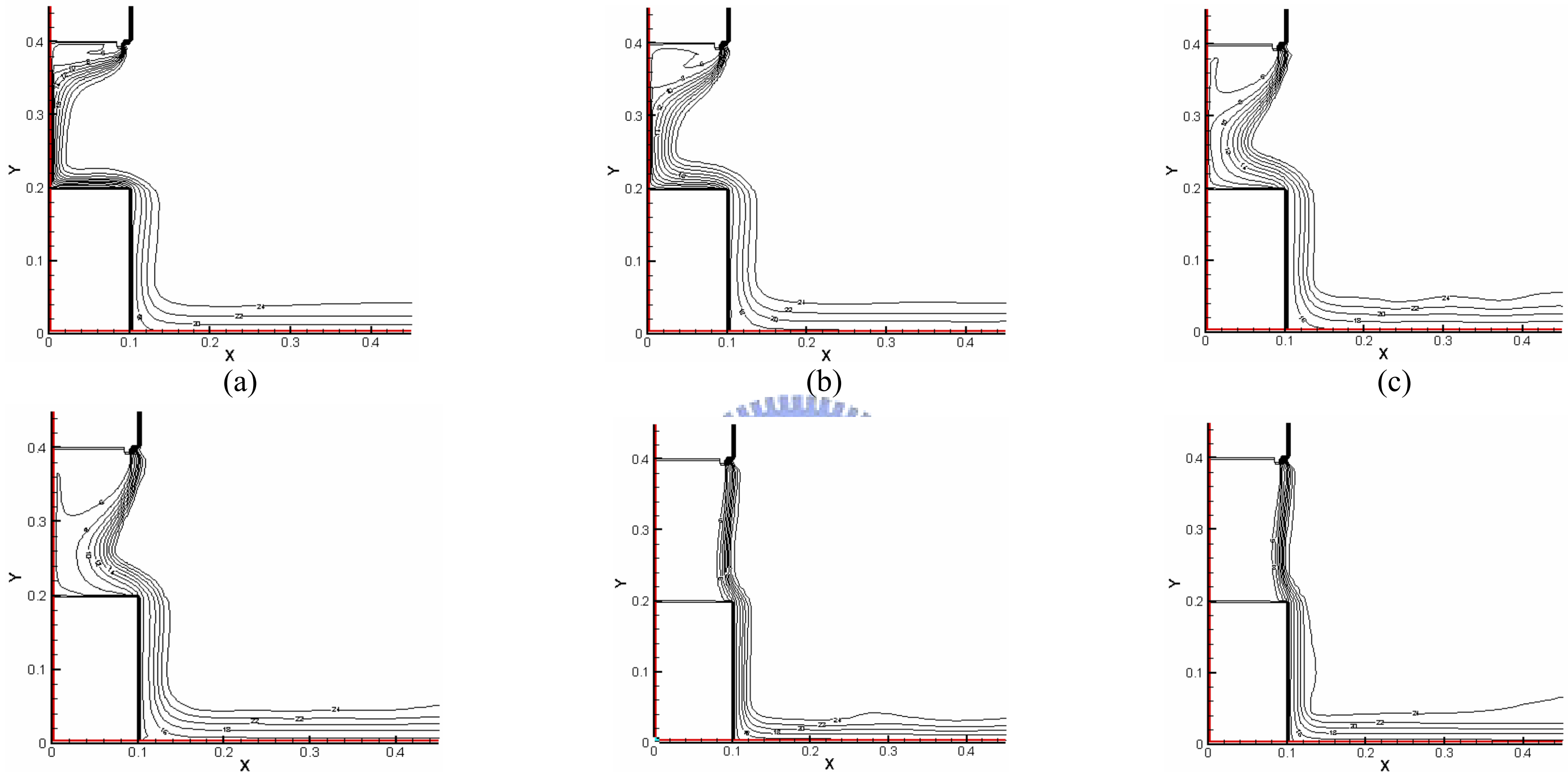

(a) (b) (c)

(d) (e) (f)

Fig. 4.46 Isotherms in the cavity for $b_j = 0.016m, Gr_t = 2.7\times10^7$ and N= $6.35\cdot10^{-2}$ with a jet inclined angle of 25° for $\mathrm{Re}_b =$ (a) 100.5 (V_j= 0.0875 m/s), (b) 215.3 (V_j= 0.187 m/s), (c) 430.7 (V_j= 0.375m/s), (d) 574.2 (V_j= 0.5m/s), (e) 646 (V_j= 0.56m/s), and (f) 717.8 (V_j= 0.62 m/s)

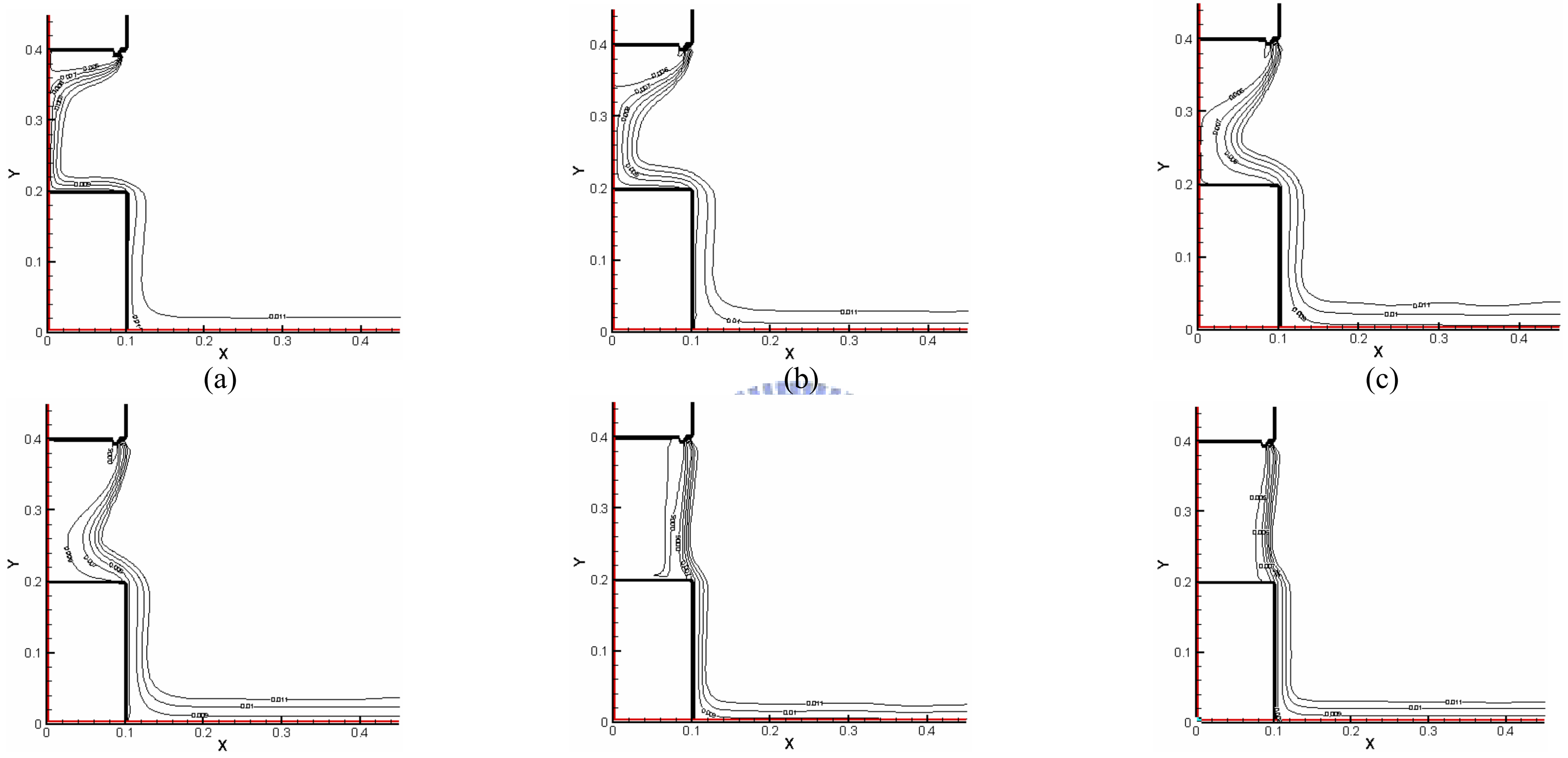

(a) (b) (c)

(d) (e) (f)

Fig. 4.47 Iso-concentration lines for $b_j = 0.016m, Gr_t = 2.7\times10^7$ and N=$6.35\cdot10^{-2}$ with a jet inclined angle of 25° for $\mathrm{Re}_b =$ (a) 100.5 (V_j= 0.0875 m/s), (b) 215.3 (V_j= 0.187 m/s), (c) 430.7 (V_j= 0.375m/s), (d) 574.2 (V_j= 0.5m/s), (e) 646 (V_j= 0.56m/s), and (f) 717.8 (V_j= 0.62 m/s)

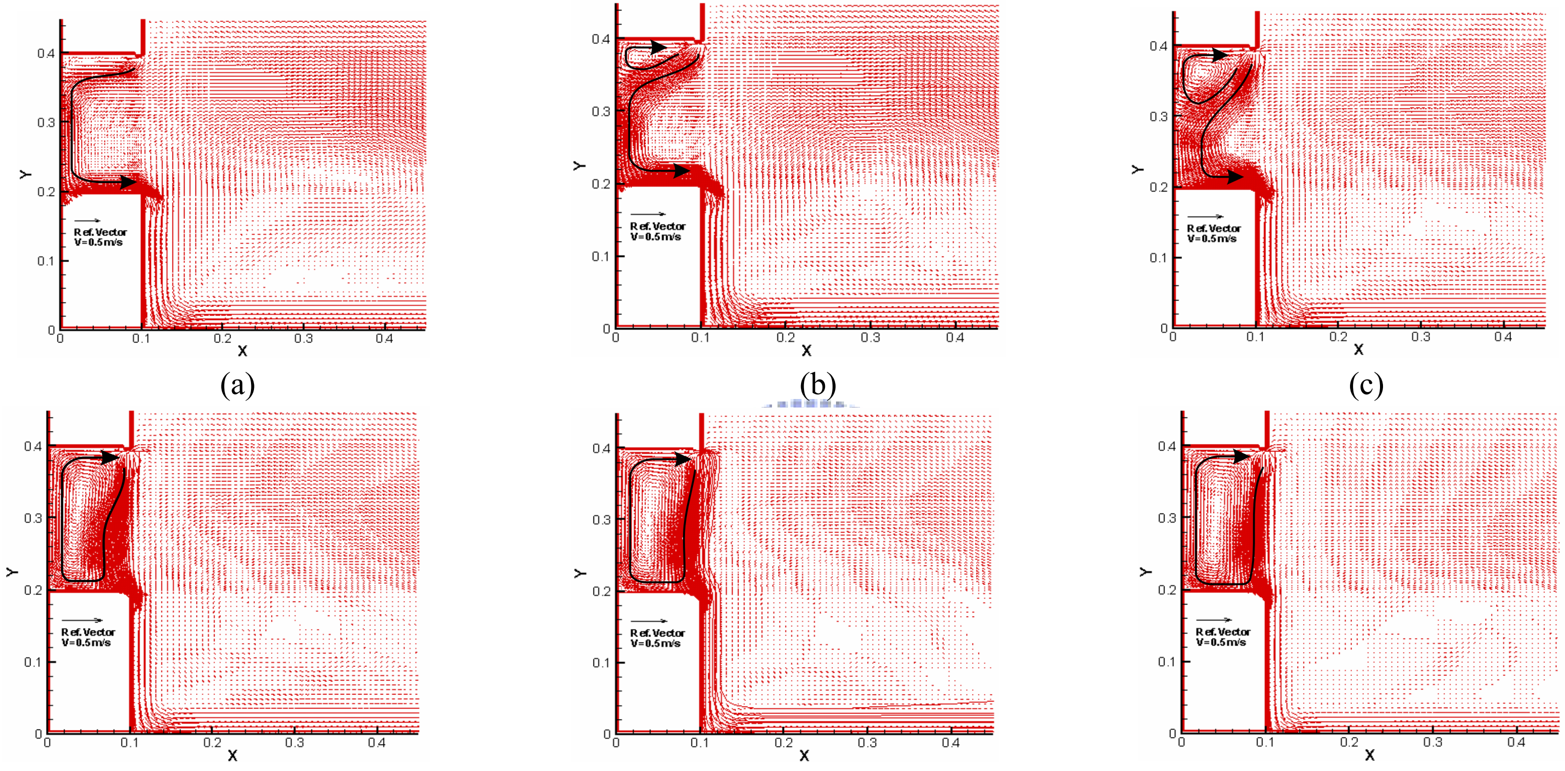

(a) (b) (c)

(d) (e) (f)

Fig. 4.48 Velocity vector maps for $b_j = 0.016m, Gr_t = 2.7\times10^{7}$ and N=$6.35\cdot10^{-2}$ with a jet inclined angle of -15° for $\mathrm{Re}_b =$ (a) 100.5 (V_j = 0.0875 m/s), (b) 215.3 (V_j = 0.187 m/s), (c) 430.7 (V_j = 0.375m/s), (d) 574.2 (V_j = 0.5m/s), (e) 646 (V_j = 0.56m/s), and (f) 717.8 (V_j = 0.62 m/s)

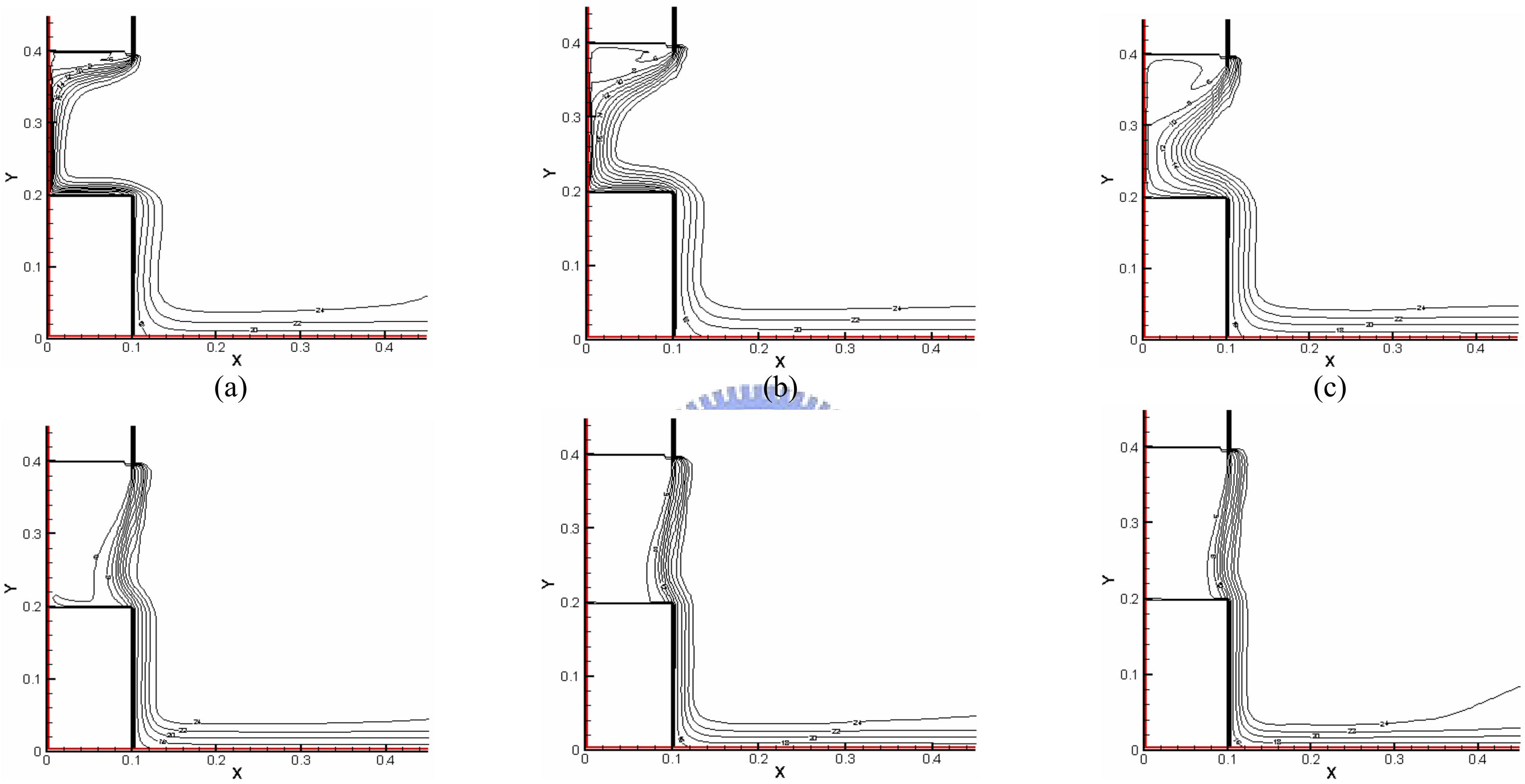

(a) (b) (c)

(d) (e) (f)

Fig. 4.49 Isotherms in the cavity for $b_j = 0.016m, Gr_t = 2.7\times10^7$ and N$=6.35\cdot10^{-2}$ with a jet inclined angle of -15° for $\mathrm{Re}_b =$ (a) 100.5 (V_j = 0.0875 m/s), (b) 215.3 (V_j = 0.187 m/s), (c) 430.7 (V_j = 0.375m/s), (d) 574.2 (V_j = 0.5m/s), (e) 646 (V_j = 0.56m/s), and (f) 717.8 (V_j = 0.62 m/s)

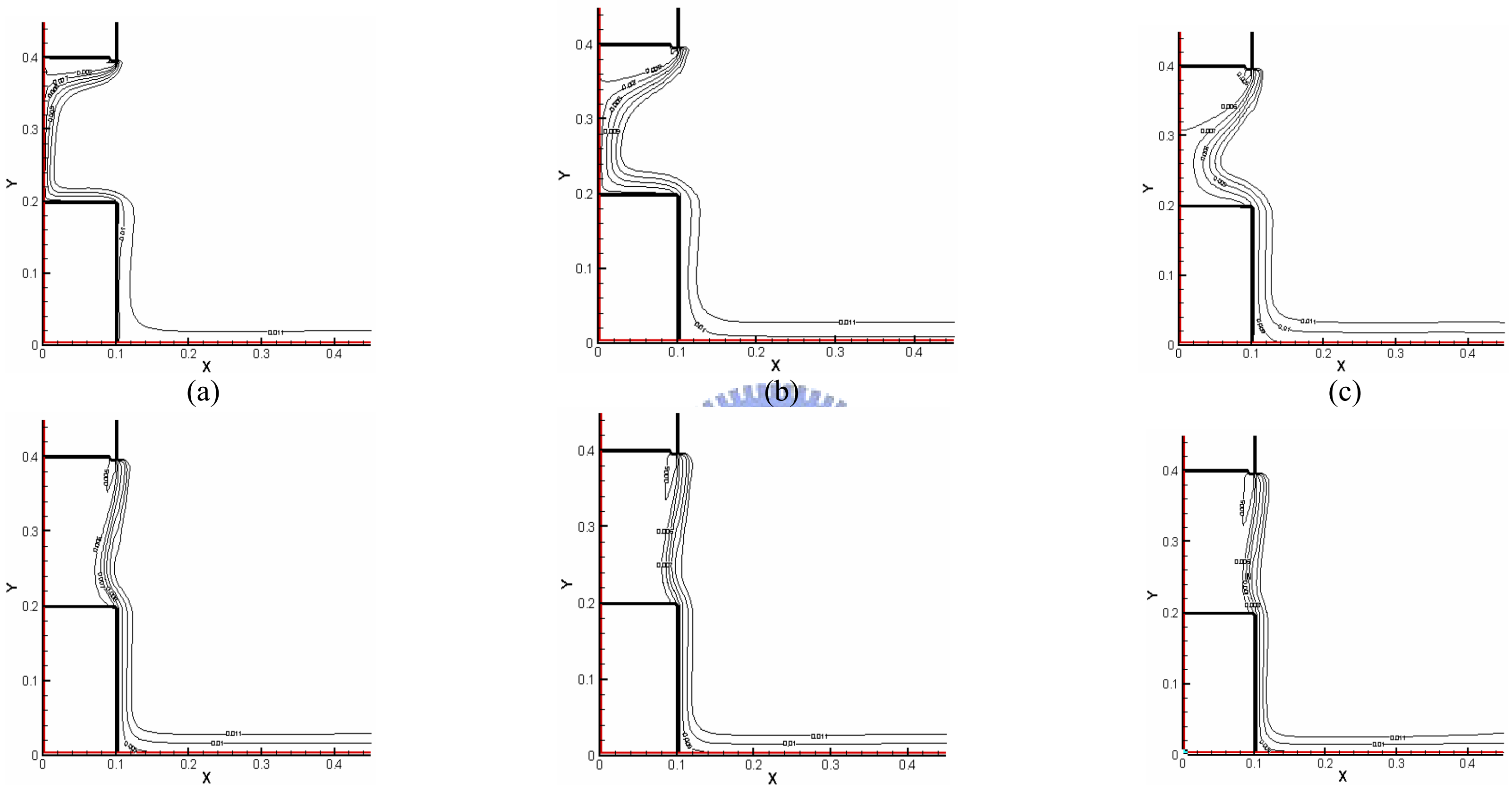

(a) (b) (c)

(d) (e) (f)

Fig. 4.50 Iso-concentration lines for $b_j = 0.016m, Gr_t = 2.7\times10^7$ and N=$6.35\cdot10^{-2}$ with a jet inclined angle of -15° for Re_b = (a) 100.5 (V_j= 0.0875 m/s), (b) 215.3 (V_j= 0.187 m/s), (c) 430.7 (V_j= 0.375m/s), (d) 574.2 (V_j= 0.5m/s), (e) 646 (V_j= 0.56m/s), and (f) 717.8 (V_j= 0.62 m/s)

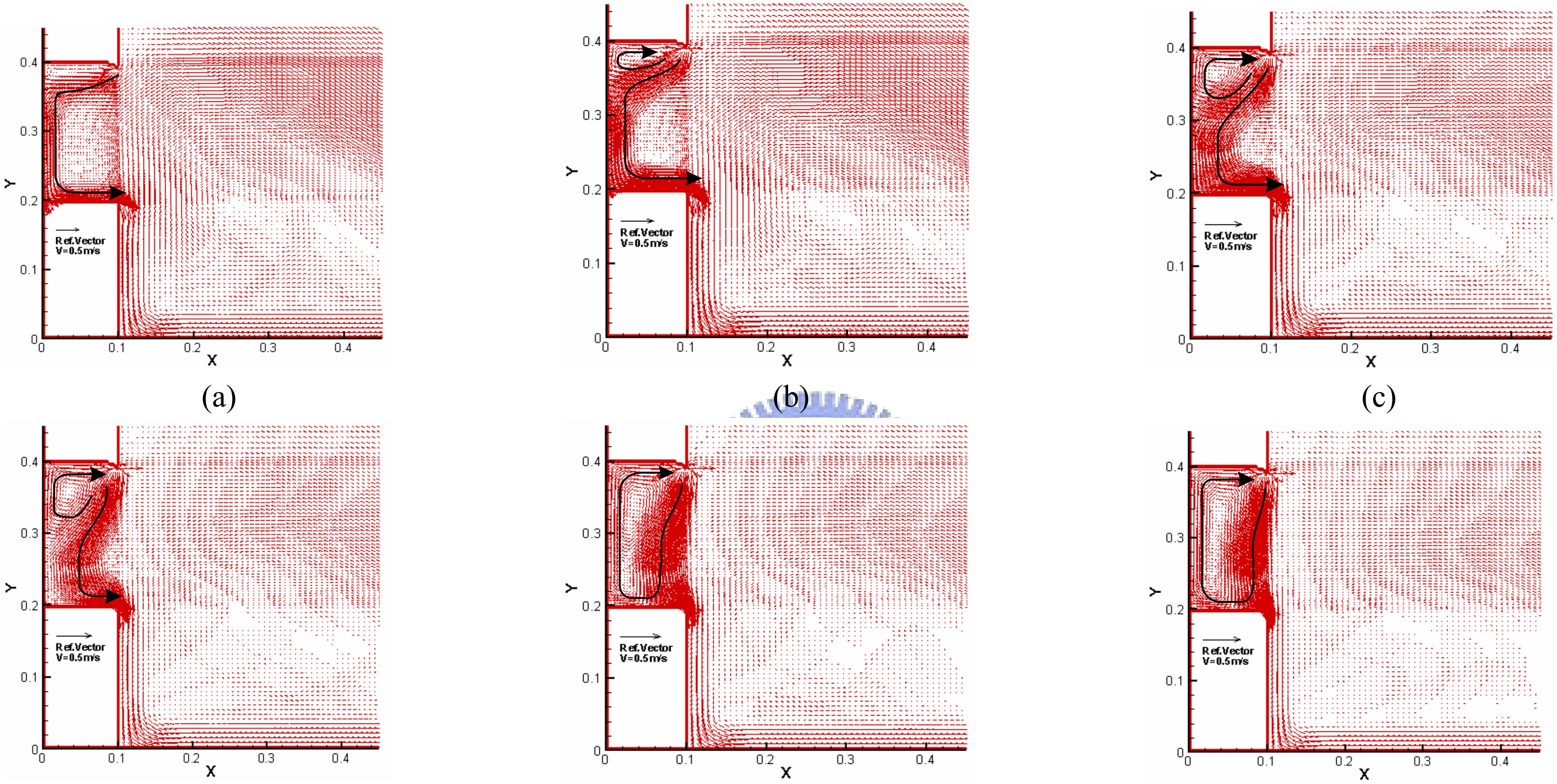

(a) (b) (c)

(d) (e) (f)

Fig. 4.51 Velocity vector maps for $b_j = 0.016m, Gr_t = 2.7\times10^7$ and N=$6.35\cdot10^{-2}$ with a jet inclined angle of -25° for $\mathrm{Re}_b =$ (a) 100.5 (V_j = 0.0875 m/s), (b) 215.3 (V_j = 0.187 m/s), (c) 430.7 (V_j = 0.375m/s), (d) 574.2 (V_j = 0.5m/s), (e) 646 (V_j = 0.56m/s), and (f) 717.8 (V_j = 0.62 m/s)

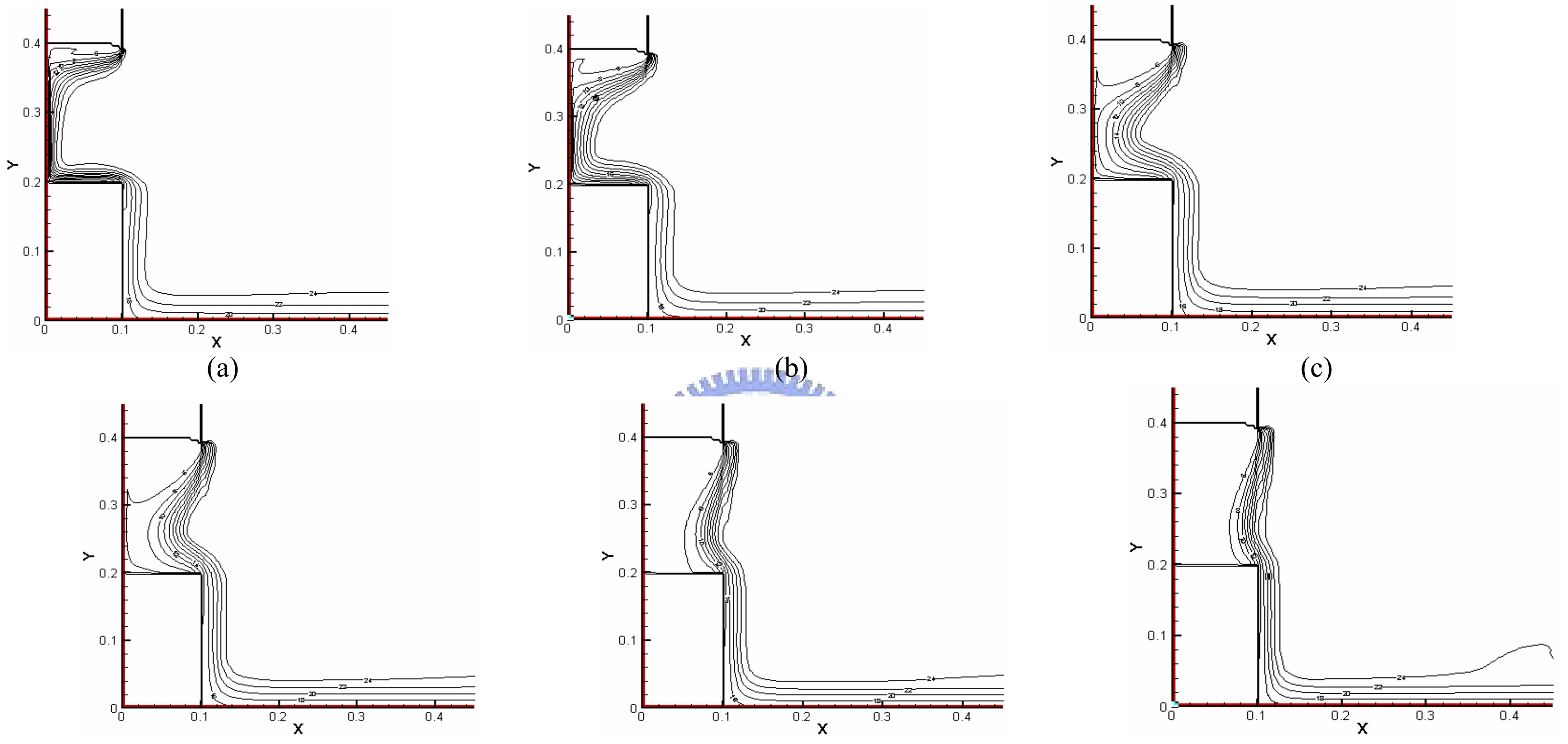

(a) (b) (c)

(d) (e) (f)

Fig. 4.52 Isotherms in the cavity for $b_j = 0.016m, Gr_t = 2.7\times10^7$ and N=$6.35\cdot10^{-2}$ with a jet inclined angle of -25° for Re_b = (a) 100.5 (V_j= 0.0875 m/s), (b) 215.3 (V_j= 0.187 m/s), (c) 430.7 (V_j= 0.375m/s), (d) 574.2 (V_j= 0.5m/s), (e) 646 (V_j= 0.56m/s), and (f) 717.8 (V_j= 0.62 m/s)

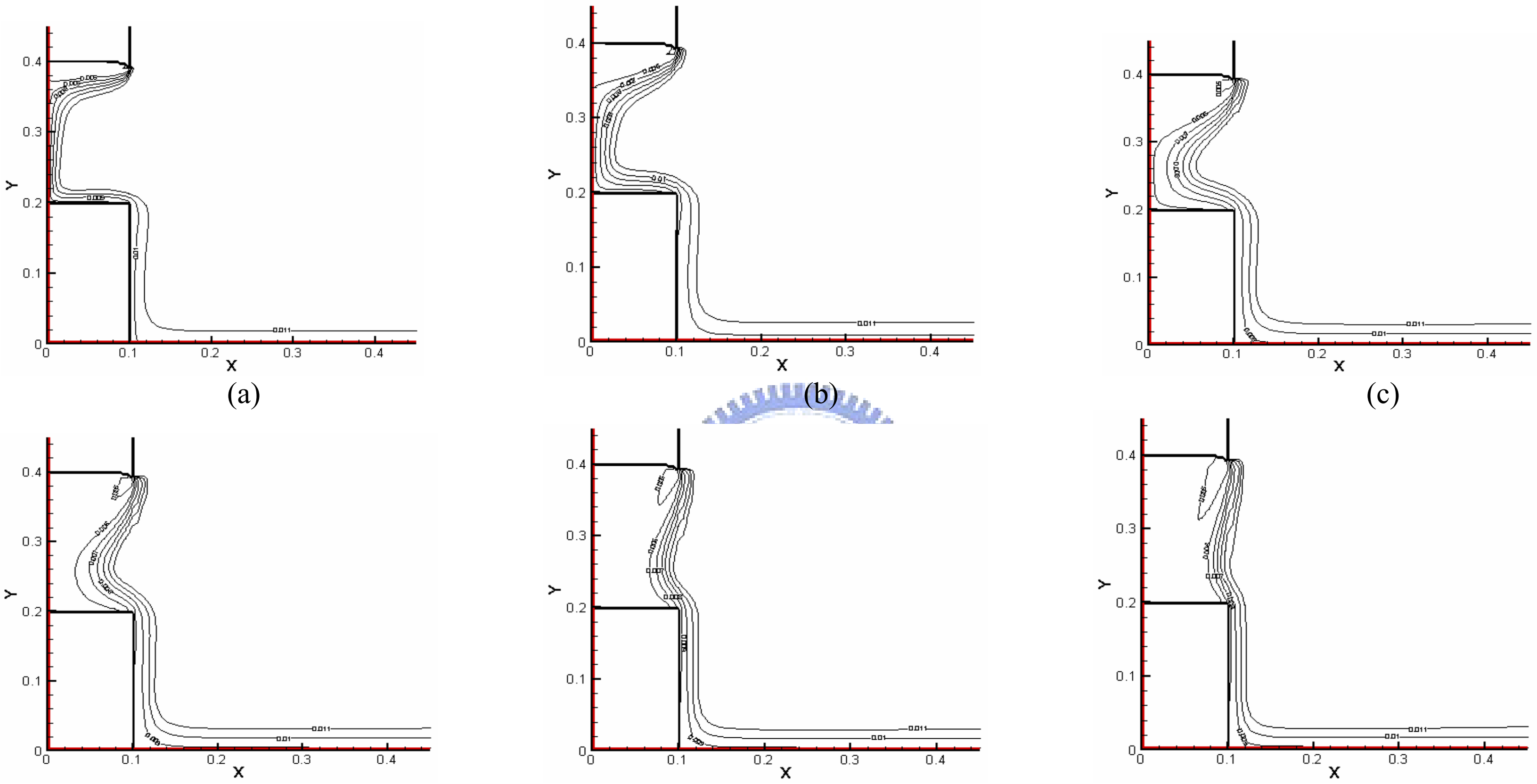

(a) (b) (c)

(d) (e) (f)

Fig. 4.53 Iso-concentration lines for $b_j = 0.016m, Gr_t = 2.7\times10^7$ and N$=6.35\cdot10^{-2}$ with a jet inclined angle of -25° for $\mathrm{Re}_b =$ (a) 100.5 (V_j= 0.0875 m/s), (b) 215.3 (V_j= 0.187 m/s), (c) 430.7 (V_j= 0.375m/s), (d) 574.2 (V_j= 0.5m/s), (e) 646 (V_j= 0.56m/s), and (f) 717.8 (V_j= 0.62 m/s).

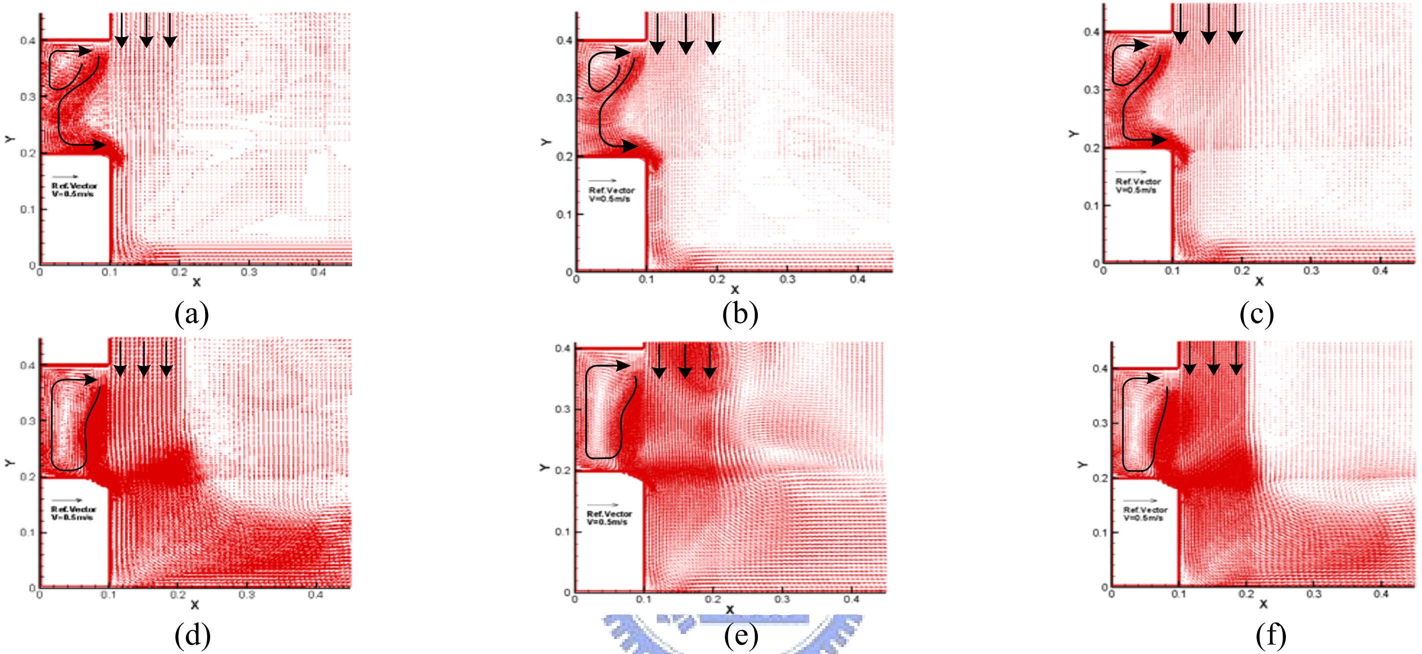

(a) (b) (c)

(d) (e) (f)

Fig. 4.54 Velocity vector maps for steady cavity flow for $\mathrm{Re}_b = 574.2$, $V_j = 0.4\,\mathrm{m/s}$, $b_j = 0.02m$, $Gr_t = 2.7 \times 10^7$ $(\Delta T = 20^0 C)$ and $N = 6.35 \cdot 10^{-2}$ covered by a second air jet with, $T_{2j} = 25^{\circ}\mathrm{C}$ and $b_{2j} = 0.01m$ for the total number of cells = (a) 13,208 ($V_{2j} = 0.1$ m/s), (b) 15,428 ($V_{2j} = 0.1$ m/s), (c) 17,168 ($V_{2j} = 0.1$m/s, domain size= 1 × 0.6 m^2), (d) 13,208 ($V_{2j} = 0.4$m/s), (e)15,428 ($V_{2j} = 0.4$m/s),(f) 17,168 ($V_{2j} = 0.4$ m/s, domain size = 1 × 0.6 m^2)

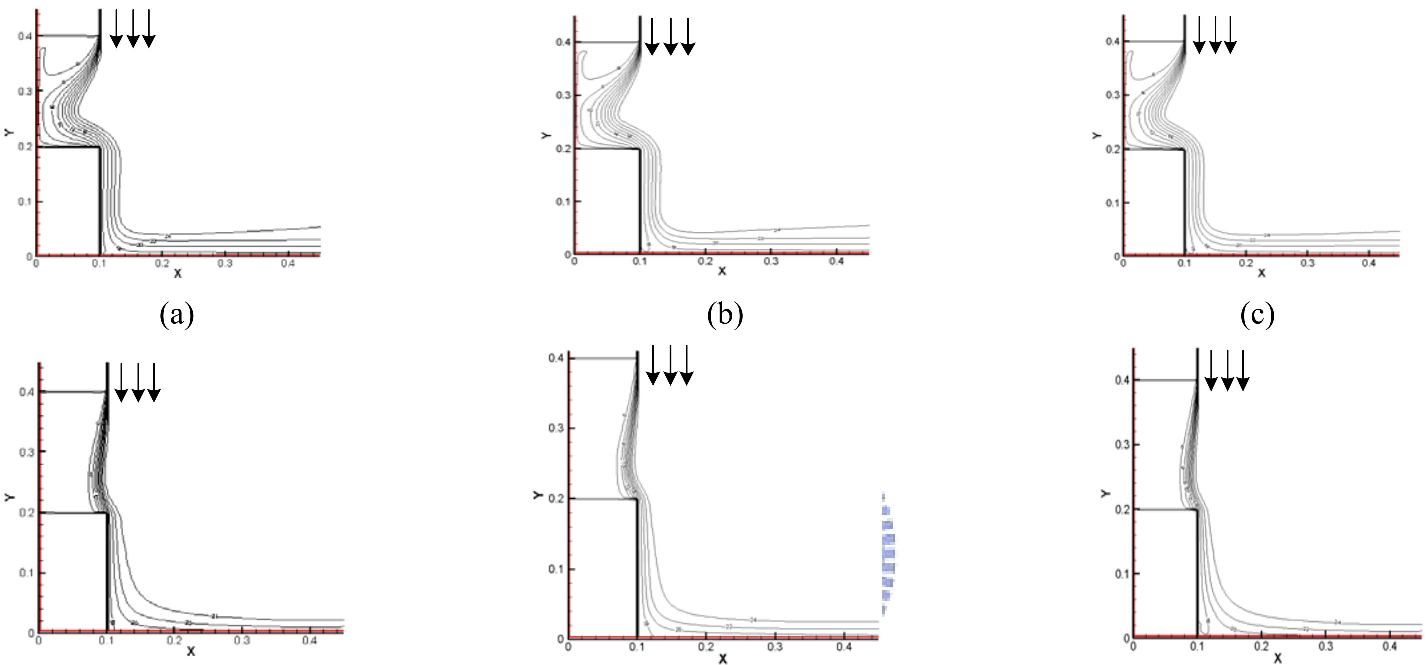

(a) (b) (c)

(d) (e) (f)

Fig. 4.55 Isotherms in the cavity for steady cavity flow for $\mathrm{Re}_b = 574.2$, $V_j = 0.4$m/s, $b_j = 0.02m$, $Gr_t = 2.7\times10^7$ $(\Delta T = 20^0 C)$ and $N = 6.35\cdot10^{-2}$ covered by a second air jet with $T_{2j} = 25^\circ\mathrm{C}$ and $b_{2j} = 0.01m$ for the total number of cells = (a) 13,208 ($V_{2j} = 0.1$ m/s), (b) 15,428 ($V_{2j} = 0.1$ m/s), (c) 17,168 ($V_{2j} = 0.1$m/s, domain size= 1 × 0.6 m^2), (d) 13,208 ($V_{2j} = 0.4$m/s), (e)15,428 ($V_{2j} = 0.4$m/s),(f) 17,168 ($V_{2j} = 0.4$ m/s, domain size = 1 × 0.6 m^2)

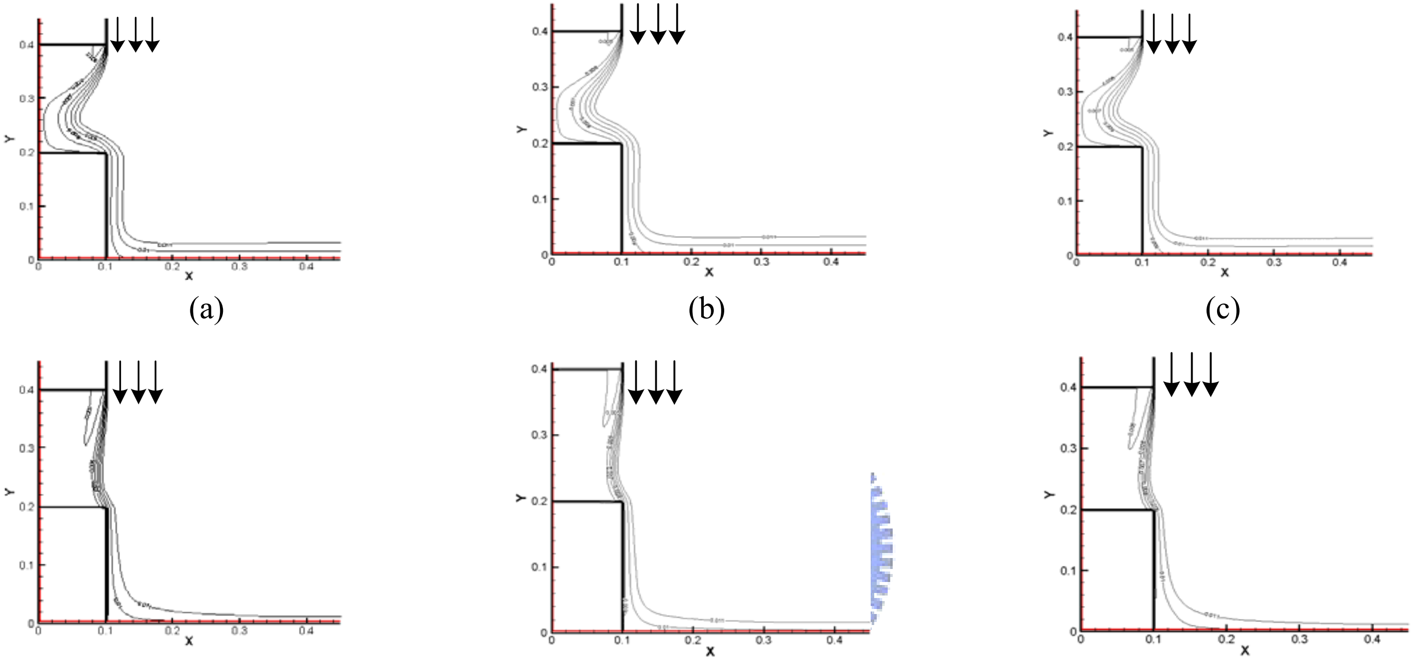

(a) (b) (c)

(d) (e) (f)

Fig. 4.56 Iso-concentration lines for steady cavity flow for $\mathrm{Re}_b = 574.2$, $V_j = 0.4$m/s, $b_j = 0.02m$, $Gr_t = 2.7\times10^7$ $(\Delta T = 20^0C)$, $N = 6.35\cdot10^{-2}$, and covered by a second air jet with $T_{2j} = 25^\circ\mathrm{C}$ and $b_{2j} = 0.01m$ for the total number of cells = (a) 13,208 ($V_{2j} = 0.1$ m/s), (b) 15,428 ($V_{2j} = 0.1$ m/s), (c) 17,168 ($V_{2j} = 0.1$m/s, domain size= 1 × 0.6 m^2), (d) 13,208 ($V_{2j} = 0.4$m/s), (e)15,428 ($V_{2j} = 0.4$m/s),(f) 17,168 ($V_{2j} = 0.4$ m/s, domain size = 1 × 0.6 m^2)

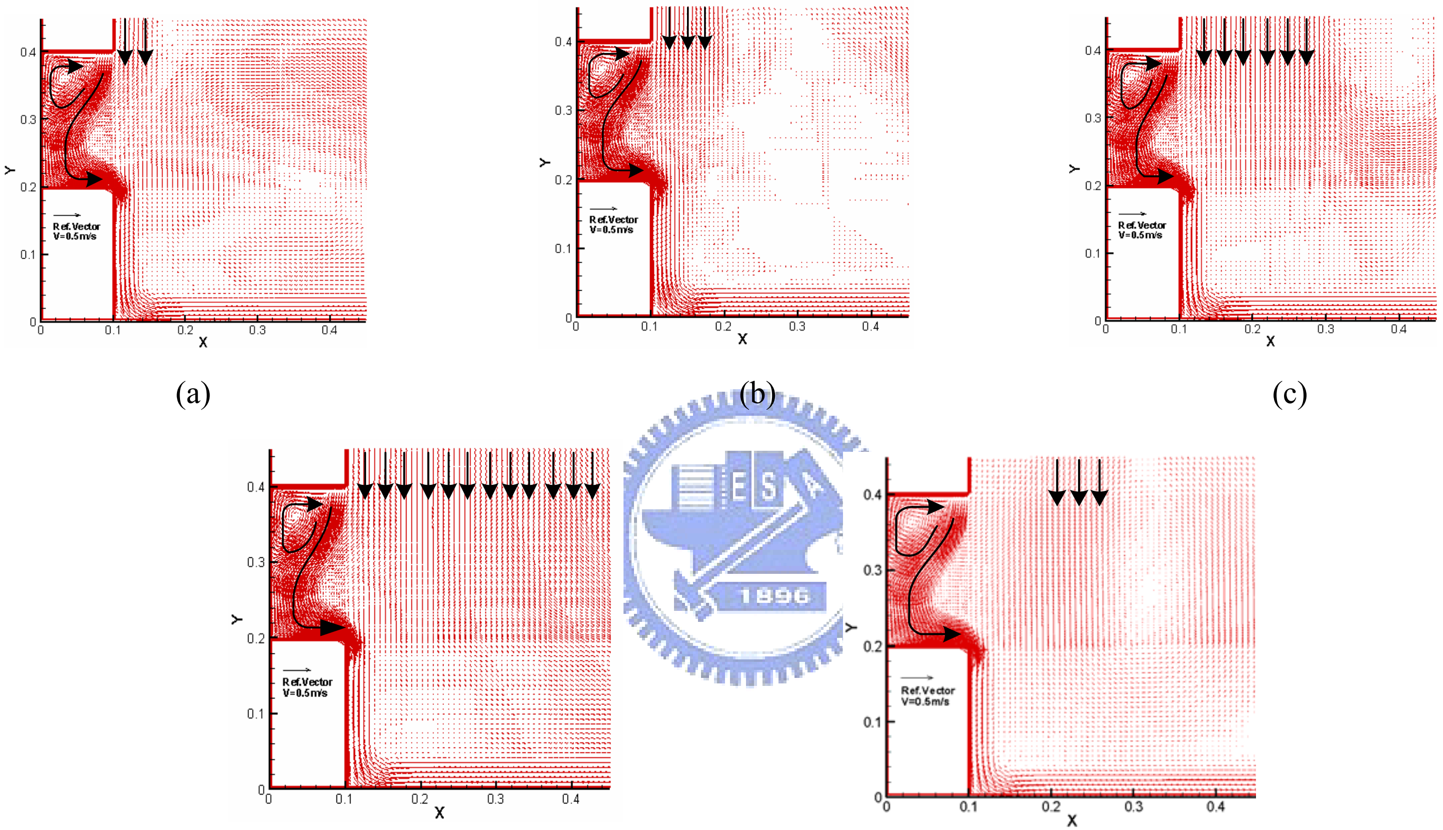

(a) (b) (c)

(d) (e)

Fig. 4.57 Velocity vector maps for steady cavity flow for $Re_b = 574.2$, $V_j = 0.4$m/s, $b_j = 0.02m$, $Gr_t = 2.7\times10^7$ $(\Delta T = 20^0C)$ and $N=6.35\cdot10^{-2}$ covered by a second air jet with $V_{2j} = 0.1$ m/s, $T_{2j} = 25^\circ C$ for $b_{2j} =$ (a) $0.05m$, (b) $0.1m$, (c) $0.2m$, (d) $0.7m$, (e) $0.1m$ at $L=0.2m$

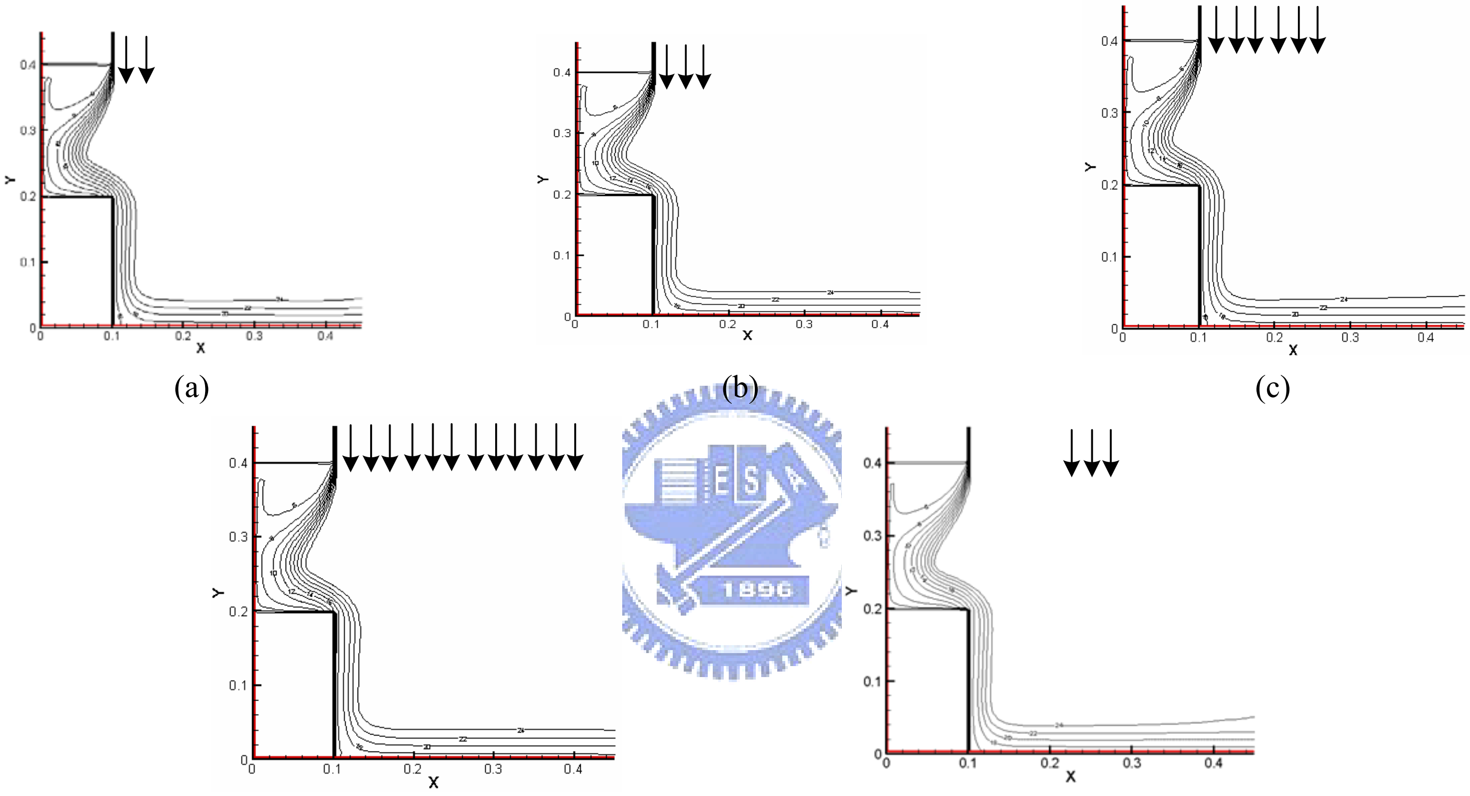

(a) (b) (c)

(d) (e)

Fig. 4.58 Isotherms in the cavity for steady cavity flow for $\mathrm{Re}_b = 574.2$, $V_j = 0.4$m/s, $b_j = 0.02m$, $Gr_t = 2.7\times10^7$ $(\Delta T = 20^0 C)$ and $N = 6.35\cdot10^{-2}$ covered by a second air jet with $V_{2j} = 0.1$ m/s, $T_{2j} = 25$℃ for $b_{2j} =$ (a) $0.05m$, (b) $0.1m$, (c) $0.2m$, (d) $0.7m$, (e) $0.1m$ at L= $0.2m$

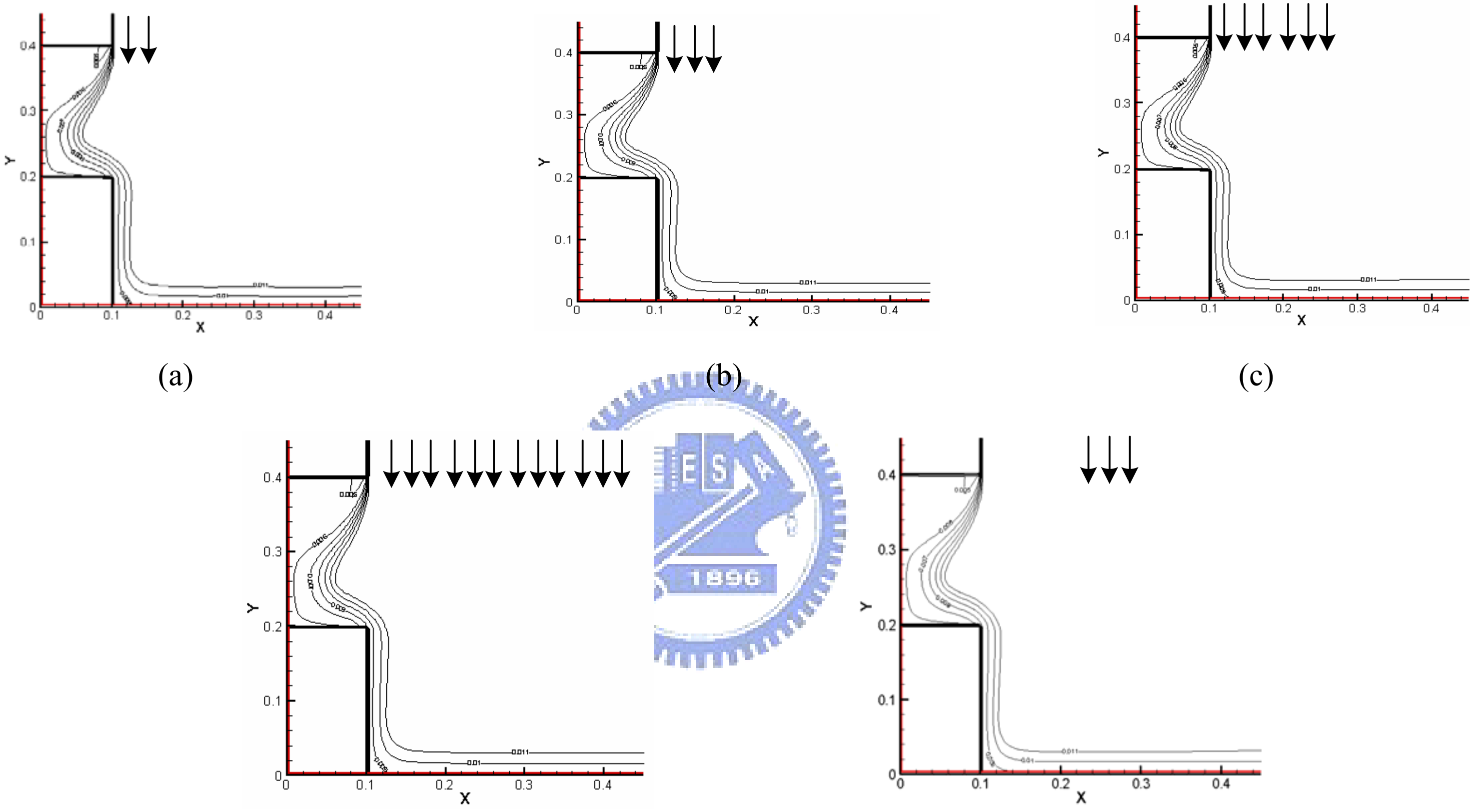

(a) (b) (c)

(d) (e)

Fig. 4.59 Iso-concentration lines for steady cavity flow for Re$_b$ = 574.2, V$_j$ = 0.4m/s, $b_j = 0.02m$, $Gr_t = 2.7\times10^7$ $(\Delta T = 20^0 C)$, $N = 6.35\cdot10^{-2}$, and covered by a second air jet with V_{2j} = 0.1 m/s, T_{2j} = 25℃ for b_{2j} = (a) $0.05m$, (b) $0.1m$, (c) $0.2m$, (d) $0.7m$, (e) $0.1m$ at L=$0.2m$

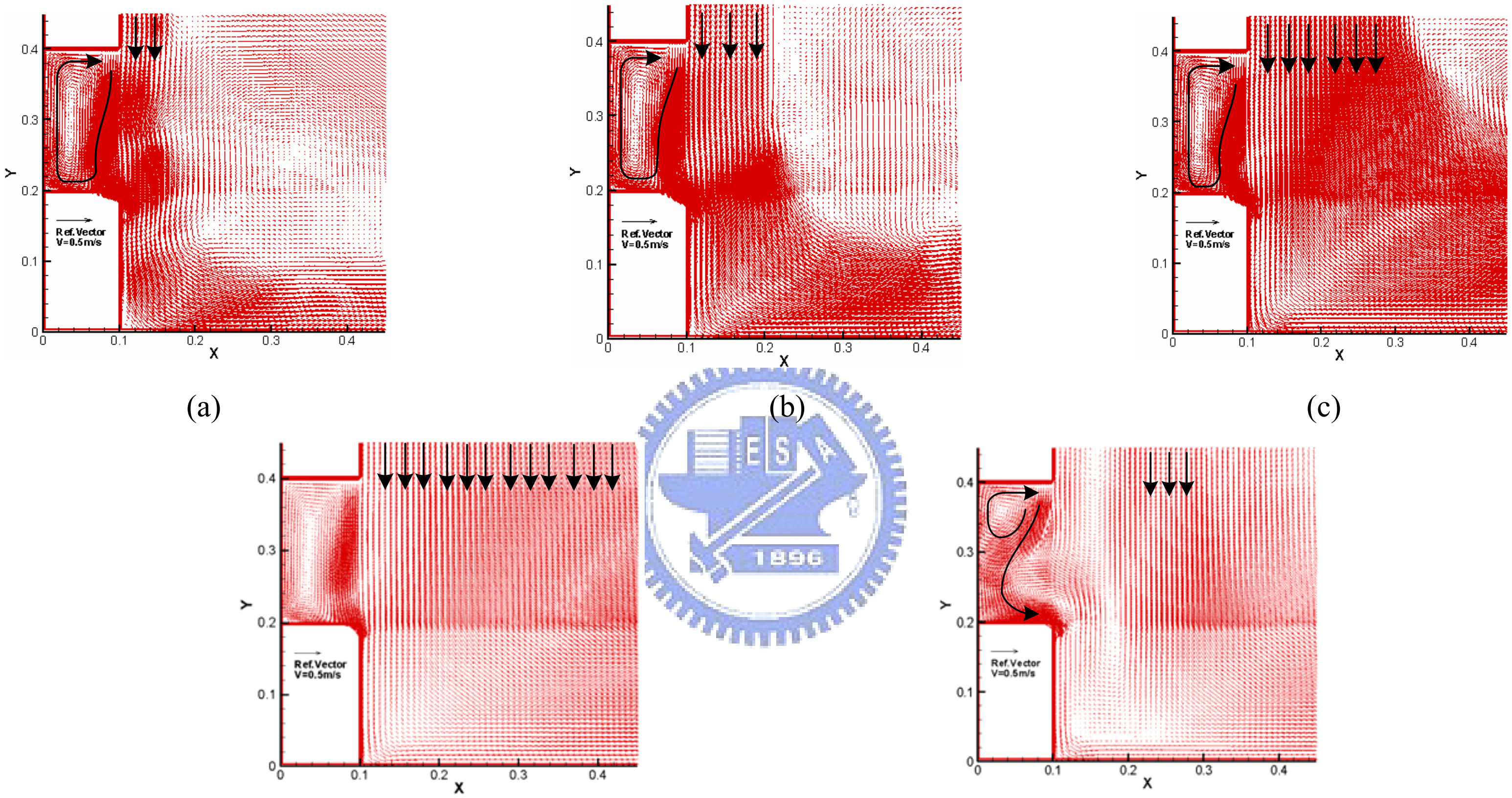

(a)

(b)

(c)

(d)

(e)

Fig. 4.60 Velocity vector maps for steady cavity flow for $Re_b = 574.2$, $V_j = 0.4m/s$, $b_j = 0.02m$, $Gr_t = 2.7\times10^7$ $(\Delta T = 20^0 C)$ and $N = 6.35\cdot10^{-2}$

covered by a second air jet with $V_{2j} = 0.4m/s$, $T_{2j} = 25^\circ C$ for $b_{2j} =$ (a) $0.05m$, (b) $0.1m$, (c) $0.2m$, (d) $0.7m$, (e) $0.1m$ at $L = 0.2m$

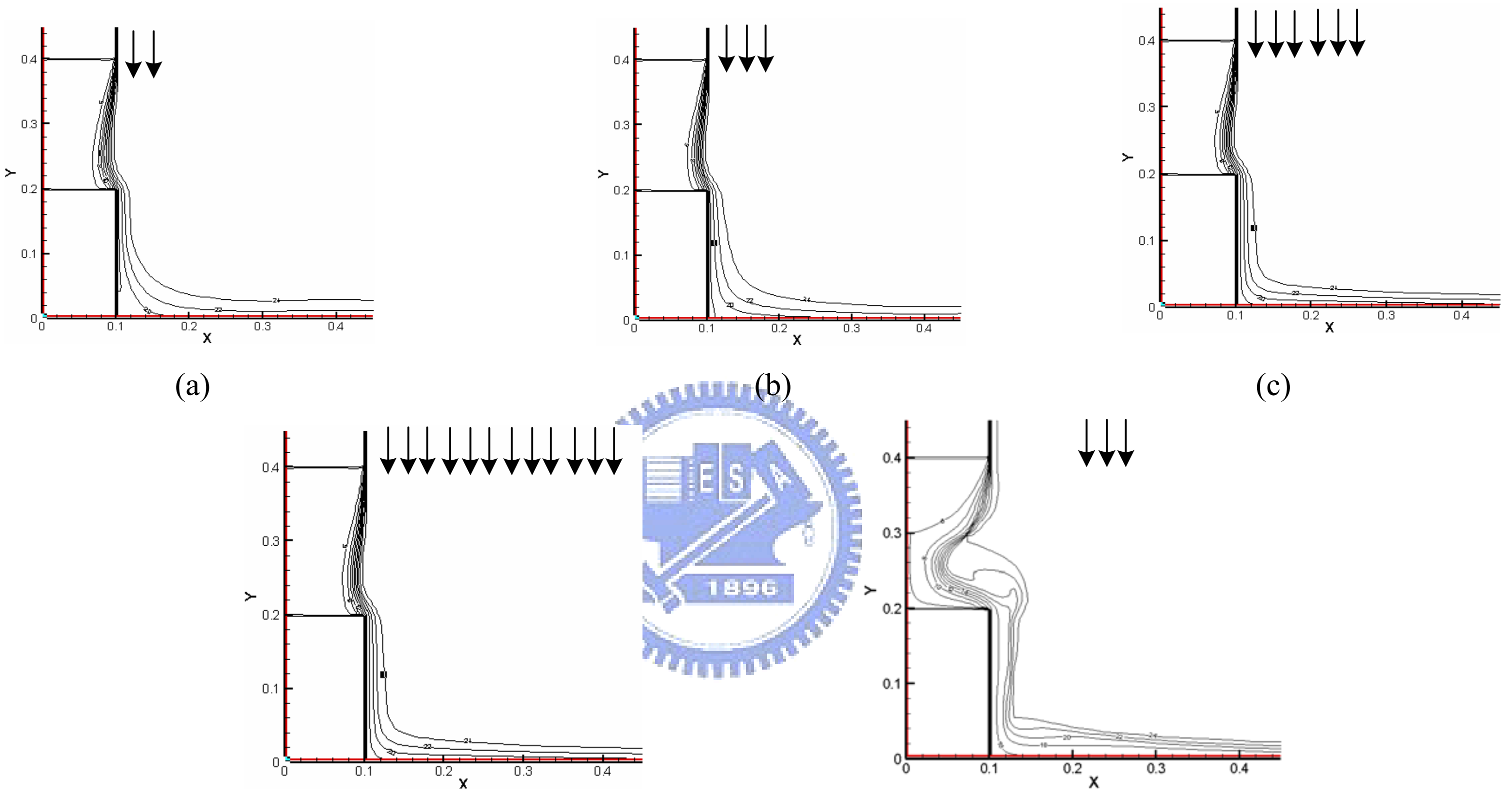

(a) (b) (c)

(d) (e)

Fig. 4.61 Isotherms in the cavity for steady cavity flow for $\mathrm{Re_b} = 574.2$, $\mathrm{V_j} = 0.4\mathrm{m/s}$, $b_j = 0.02m$, $Gr_t = 2.7\times10^7$ $(\Delta T = 20^0 C)$ and $\mathrm{N}=6.35\cdot10^{-2}$ covered by a second air jet with $V_{2j} = 0.4$ m/s, $T_{2j} = 25^\circ\mathrm{C}$ for $b_{2j} =$ (a) $0.05m$, (b) $0.1m$, (c) $0.2m$, (d) $0.7m$, (e) $0.1m$ at $\mathrm{L}=0.2m$

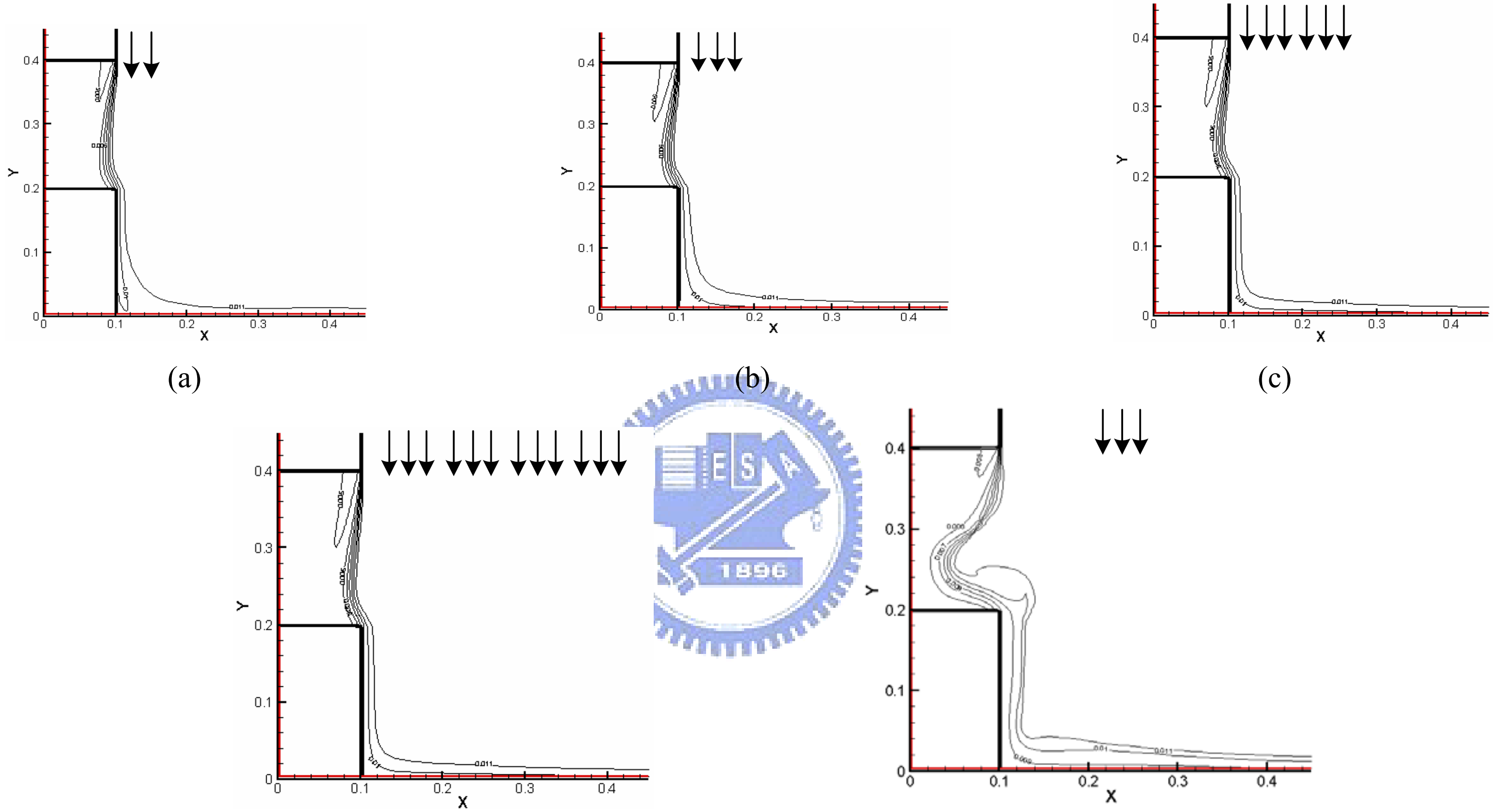

(a) (b) (c)

(d) (e)

Fig. 4.62 Iso-concentration lines for steady cavity flow for $\mathrm{Re_b} = 574.2$, $\mathrm{V_j} = 0.4\,\mathrm{m/s}$, $b_j = 0.02m$, $Gr_t = 2.7\times10^7$ $(\Delta T = 20^0C)$, $\mathrm{N} = 6.35\cdot10^{-2}$, and covered by a second air jet with $V_{2j} = 0.4$ m/s, $T_{2j} = 25^\circ\mathrm{C}$ for $b_{2j} =$ (a) $0.05m$, (b) $0.1m$, (c) $0.2m$, (d) $0.7m$, (e) $0.1m$ at $\mathrm{L}=0.2m$

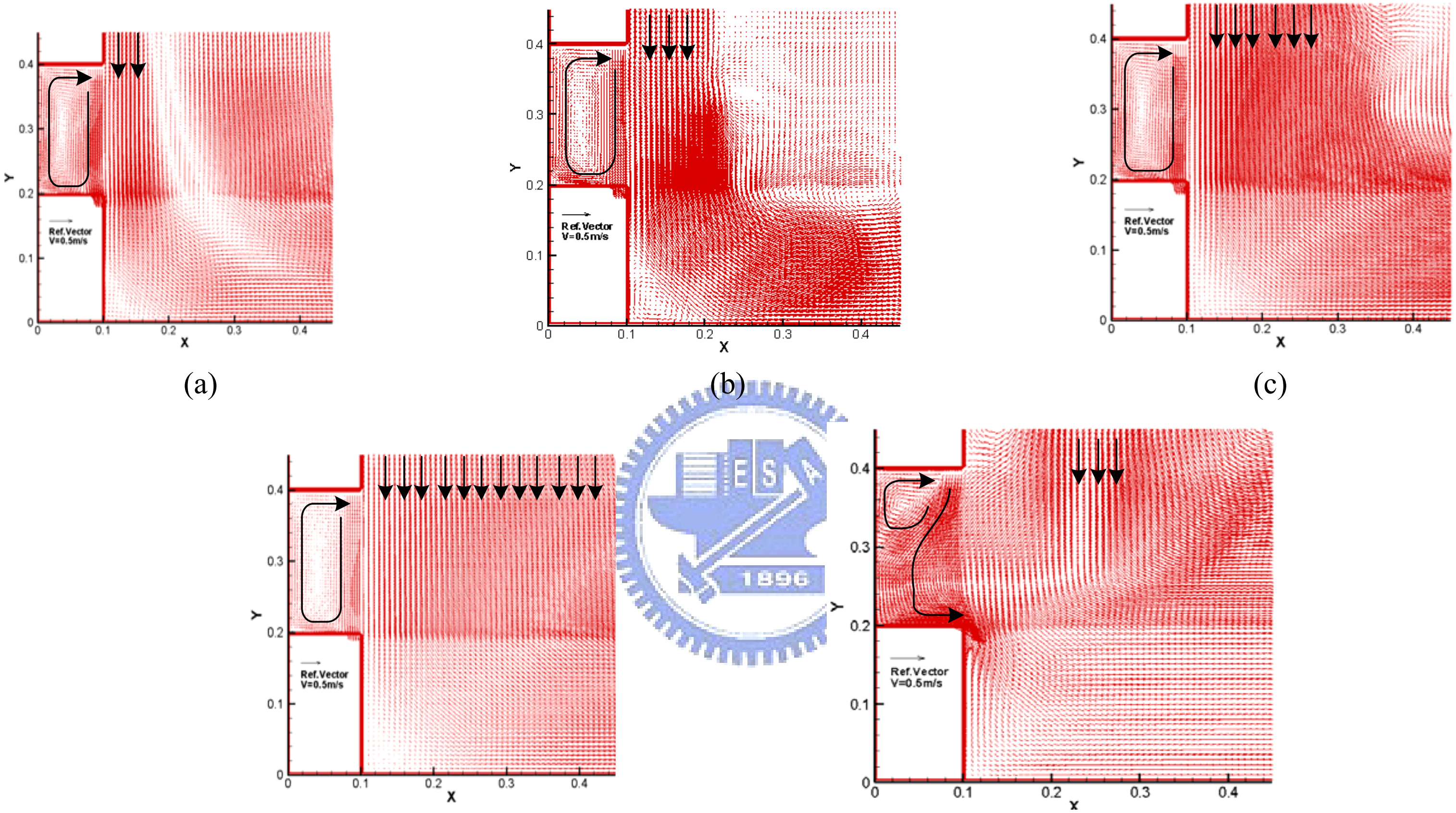

(a) (b) (c)

(d) (e)

Fig. 4.63 Velocity vector maps for steady cavity flow for $\mathrm{Re}_b = 574.2$, $V_j = 0.4\mathrm{m/s}$, $b_j = 0.02m$, $Gr_t = 2.7\times10^7$ $(\Delta T = 20^0 C)$ and $N = 6.35\cdot10^{-2}$

covered by a second air jet with $V_{2j} = 0.7$ m/s, $T_{2j} = 25^\circ\mathrm{C}$ for $b_{2j} =$ (a) $0.05m$, (b) $0.1m$, (c) $0.2m$, (d) $0.7m$, (e) $0.1m$ at $L = 0.2m$

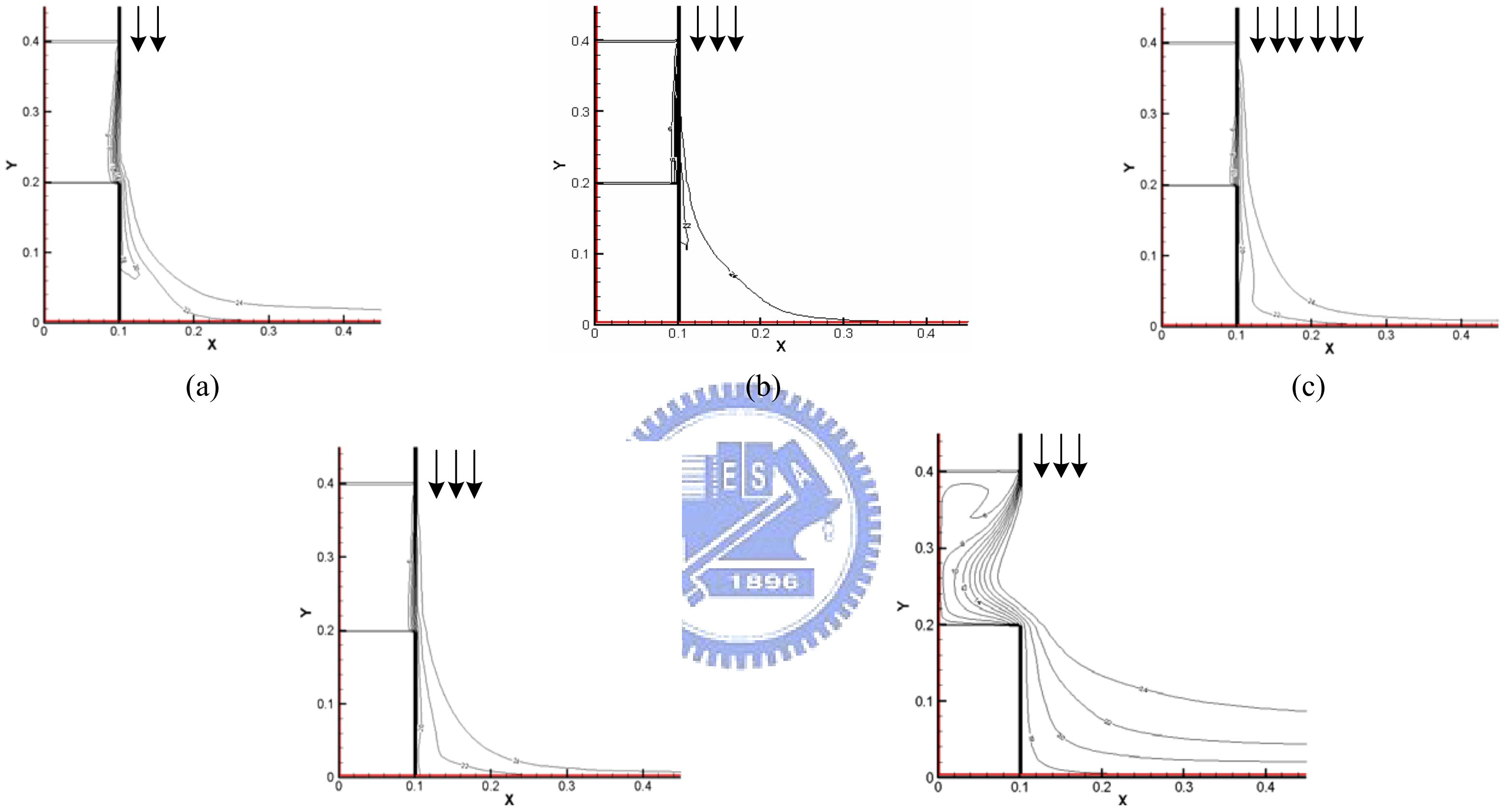

(a) (b) (c)

(d) (e)

Fig. 4.64 Isotherms in the cavity for steady cavity flow for $\mathrm{Re_b} = 574.2$, $\mathrm{V_j} = 0.4\mathrm{m/s}$, $b_j = 0.02m$, $Gr_t = 2.7\times10^7$ $(\Delta T = 20^0 C)$ and $\mathrm{N} = 6.35\cdot10^{-2}$ covered by a second air jet with $V_{2j} = 0.7$ m/s, $T_{2j} = 25^{\circ}\mathrm{C}$ for $b_{2j} =$ (a) $0.05m$, (b) $0.1m$, (c) $0.2m$, (d) $0.7m$, (e) $0.1m$ at $\mathrm{L} = 0.2m$

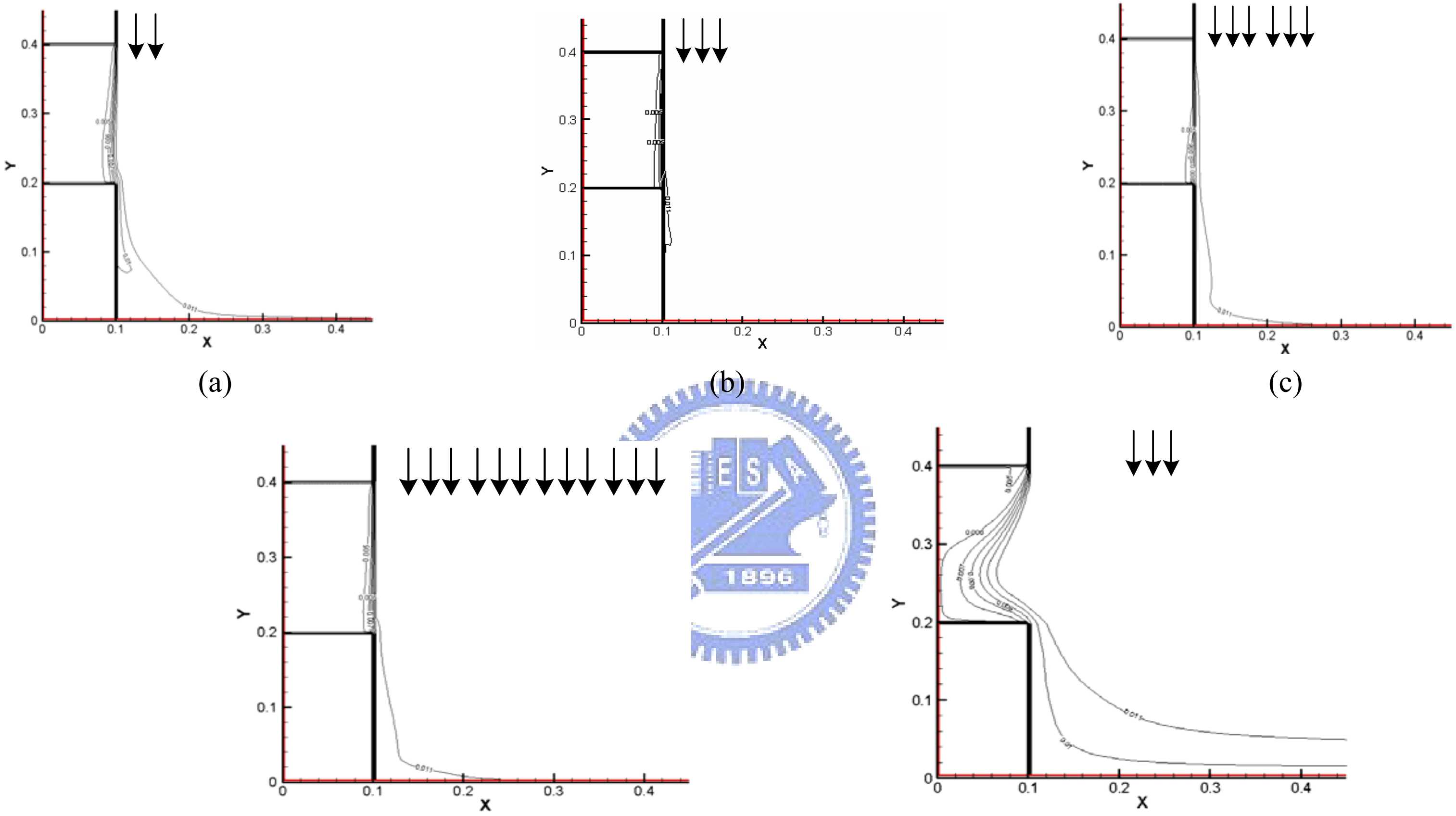

(a) (b) (c)

(d) (e)

Fig. 4.65 Iso-concentration lines for steady cavity flow for $\mathrm{Re_b} = 574.2$, $\mathrm{V_j} = 0.4\mathrm{m/s}$, $b_j = 0.02m$, $Gr_t = 2.7\times10^7$ $(\Delta T = 20^0 C)$, $\mathrm{N} = 6.35\cdot10^{-2}$, and covered by a second air jet with $V_{2j} = 0.7$ m/s, $T_{2j} = 25$℃ for $b_{2j} =$ (a) $0.05m$, (b) $0.1m$, (c) $0.2m$, (d) $0.7m$, (e) $0.1m$ at $\mathrm{L}=0.2m$